

THESIS

EVALUATION OF THE KIPP AND ZONEN LARGE APERTURE SCINTILLOMETER FOR
ESTIMATION OF SENSIBLE HEAT FLUX OVER IRRIGATED AND NON-IRRIGATED
FIELDS IN SOUTHEASTERN COLORADO

Submitted by

Evan H. Rambikur

Department of Civil and Environmental Engineering

In partial fulfillment of the requirements

For the degree of Master of Science

Colorado State University

Fort Collins, Colorado

Fall 2012

Master's Committee:

Advisor: José L. Chávez

Allan A. Andales

Timothy K. Gates

Jay M. Ham

Copyright by Evan Herbert Rambikur 2012

All Rights Reserved

ABSTRACT

EVALUATION OF THE KIPP AND ZONEN LARGE APERTURE SCINTILLOMETER FOR ESTIMATION OF SENSIBLE HEAT FLUX OVER IRRIGATED AND NON-IRRIGATED FIELDS IN SOUTHEASTERN COLORADO

The aim of this work was to assess the performance of the Kipp and Zonen Large Aperture Scintillometer (LAS; Delft, Netherlands) to predict surface sensible heat flux (H). The LAS was introduced approximately 30 years ago and has been marketed as an indirect tool for the estimation of vegetation evapotranspiration (ET). Several tests have shown the LAS to be a fairly robust tool for prediction of H , both over homogeneous and heterogeneous surfaces. However, the Kipp and Zonen LAS has been criticized for overestimation of H and for significant inter-sensor deviation in H . Field experiments were performed in 2011 using three Kipp and Zonen LAS units over two different surfaces to assess the accuracy and inter-sensor variability. Accuracy was evaluated based on reference measurements from eddy covariance (EC) instrumentation, which provides direct measurement of sensible and latent heat fluxes. Notably the EC method has been criticized for systematic underestimation of the sensible and/or latent heat flux, but is nonetheless a common tool used to validate LAS data. The first experimental test site was predominantly dry and uniform grassland located near Timpas, CO. At this site, all three LAS units were deployed together for some time in order to assess inter-sensor variability and an EC system was installed for some duration of the LAS deployment. The EC system was subsequently moved to the second site, which was the Colorado State University (CSU) Arkansas Valley Research Center (AVRC) near Rocky Ford, CO. At the AVRC, one LAS unit was set up over irrigated alfalfa. Results from the inter-LAS comparison suggested that there may be some inherent variability between 6-11% in LAS-predicted H (H_{LAS}) and that the

physical alignment of the LAS is critical for maintaining good performance. Testing different methods for estimation of the friction velocity (u_*) variable revealed bias between the logarithmic wind profile (LWP) result and the EC measurement. Linear regression slopes between 0.94 and 1.35 were found for H_{LAS} with respect to EC-derived H (H_{EC}) for the Timpas site – dependent on the LAS unit, the LAS alignment, and the u_* method. The overall conclusion was that H_{LAS} was reasonably accurate, partially due to the potential of H_{EC} being underestimated on the basis of lack of energy balance closure. For the CSU AVRC (irrigated) site, H_{LAS} was generally observed to be greater than H_{EC} by 20-30%. However, heat flux source area differences between the LAS and EC units may have contributed to some of the observed biases. Further, the overall conclusion of reasonable accuracy of H_{LAS} was made, again partially due to potential for H underestimation by the EC system. It is recommended, nonetheless, for future applications to calibrate the Kipp and Zonen LAS to a reliable reference on the basis of observed inter-sensor variability. Further, the benefit of the LAS is judged to be higher for a scenario of limited or no irrigation than for one of full irrigation, since the contribution of H to the overall energy balance would be relatively small for a full irrigation scenario.

ACKNOWLEDGEMENTS

This work represents the culmination of two years of research devoted to understanding the Large Aperture Scintillometer method of heat flux estimation. Likely more people than mentioned here were in some way involved in this research. I very much appreciate the opportunity to participate in the research provided to me by Dr. José L. Chávez, my advisor. Further, he has been patient with me through each part of this learning experience. I appreciate also the time commitment and input of the other committee members, Drs. Allan Andales, Timothy Gates, and Jay Ham. Dr. Allan Andales also generously provided the Eddy Covariance system used in this study. Dr. Darrell Fontane provided invaluable assistance in creating the Excel-based tool for processing the LAS data. Mr. Stuart Joy (M.S.) helped in a significant way by processing the Eddy Covariance data. Mr. Gale Allen was generous to host our experiment on his ranch near Timpas, CO. Further, the staff (Dr. Michael Bartolo and Lane Simmons) of the Arkansas Valley Research Center near Rocky Ford, CO has been very gracious over multiple years of hosting our experiments. Obviously the deployment of the LAS systems has not been a one-man effort, and credit is due to multiple people for assisting in the fieldwork efforts. Finally, I would like to thank the one true God who gives all men life and breath, and has also given us spiritual life in Jesus Christ – ‘Unless the LORD builds the house, they labor in vain who build it; unless the LORD guards the city, the watchman stays awake in vain.’

Psalm 127:1

TABLE OF CONTENTS

Abstract	ii
Acknowledgements	iv
List of Tables	vii
List of Figures	viii
Introduction	1
Study objectives	7
Methodology	10
Large Aperture Scintillometer theory	10
Eddy Covariance theory and methods	15
Experimental site and methods	17
Site 1 (Timpas, CO)	18
Site 2 (AVRC, Rocky Ford, CO)	20
LAS data processing methods	23
Field data collection and raw data preparation	23
Ancillary data preparation	24
Execution of LAS data processing	27
Analysis methods	29
Data quality control / filtering	29
Comparison methods	31
Monin-Obukhov Similarity Theory (MOST) check	33
Uncertainty and LAS model sensitivity	33
Results	37
Inter-LAS comparison	37
Inter-method comparison	40
<i>H</i> comparison (Timpas)	41
Friction velocity (u_*) comparison (Timpas)	44
<i>H</i> comparison (AVRC)	46
Friction velocity (u_*) comparison (AVRC)	48
LAS to EC comparison	50
Timpas	50
AVRC	53
MOST Agreement (Timpas)	58

MOST Agreement (AVRC).....	61
Discussion.....	63
Effects of LAS alignment on H	63
Friction velocity (u_*) findings.....	64
Impacts of LAS effective height determination.....	66
LAS data evaluation with Monin-Obukhov Similarity Theory (MOST).....	67
Evaluation of H_{LAS} using H_{EC}	69
Timpas	69
AVRC	71
Differences in analysis for irrigated versus non-irrigated sites	72
H_{LAS} model uncertainty.....	74
H_{LAS} model sensitivity	75
Conclusions	78
References	83
Appendix 1. LAS setup / alignment procedure	88
Appendix 2. LAS effective height determination.....	89
Appendix 3. Hartogensis (2006) correction for C_n^2	92
Appendix 4. Computation of G	93
Appendix 5. Alternate methods for time series θ_v estimation.....	94
Appendix 6. Spatial average R_n and G estimation procedures	96
Appendix 7. LAS-1 Timpas input modifications for testing.....	99
Appendix 8. Kormann and Meixner (2001) source area model	100
Appendix 9. LAS uncertainty analysis methods.....	104
Appendix 10. LAS (on-site) calibration test.....	107
Appendix 11. Experiment photos	108

LIST OF TABLES

Table 1. LAS experimental results from selected studies	5
Table 2. LAS input uncertainty values.....	35
Table 3. LAS model input sensitivity	36
Table 4. Deviation statistics for LAS-1 to EC H comparison; Timpas site	53
Table 5. Deviation statistics for LAS-2 to EC H comparison; AVRC site	54

LIST OF FIGURES

Figure 1. Location of 2011 LAS study sites in Colorado.....	18
Figure 2. Aerial image overview of the Timpas grassland site	19
Figure 3. Aerial image overview of the AVRC site.....	22
Figure 4. Simplified LAS data processing flowchart.....	28
Figure 5. Inter-LAS H comparison regression plots.....	38
Figure 6. Inter-LAS H comparison time series plots	39
Figure 7. LAS inter-method H comparison regression plots, u_{*1-L} versus u_{*2-L} for LAS-1, -2, and -3; Timpas site.....	41
Figure 8. LAS inter-method H comparison regression plot, u_{*1-L} versus u_{*2-L} for LAS-1; July 8 th – Oct. 4 th ; Timpas site.	42
Figure 9. Same as Fig. 8, for wind speed greater than 2 m s^{-1} and H greater than zero.....	42
Figure 10. Same as Fig. 8, for wind speed greater than 4 m s^{-1} and H less than zero.....	43
Figure 11. LAS inter-method H comparison regression plots, u_{*1-L} , u_{*2-L} , and u_{*EC} versus $u_{*+L_{moEC}}$ for LAS-1; Timpas site.	44
Figure 12. LAS inter-method H comparison regression plot, original input versus modified input for LAS-1 (u_{*1-L}); Timpas site.	44
Figure 13. LAS inter-method u_{*} comparison regression plots, u_{*1-L} versus u_{*2-L} (LAS-1); Timpas site.	45
Figure 14. LAS inter-method u_{*} comparison regression plots, u_{*LWP} (LAS-1) versus u_{*EC} ; Timpas site.	46
Figure 15. LAS inter-method H comparison regression plots for LAS-2; AVRC site.....	47
Figure 16. LAS inter-method u_{*} comparison regression plots for LAS-2; AVRC site	49
Figure 17. LAS to EC H comparison for LAS-1, -2, and -3; Timpas site	51
Figure 18. Comparison plots for mean absolute error (MAE) between LAS and EC and mean uncertainty (δ) for H_{LAS} and H_{EC} , for LAS-1, -2, and -3; Timpas site	52
Figure 19. LAS to EC H comparison for LAS-1, July 9 th – August 26 th ; Timpas site	53
Figure 20. LAS to EC H comparison for LAS-2; AVRC site	55
Figure 21. Comparison plot for mean absolute error (MAE) between LAS-2 and EC and mean uncertainty (δ) for H_{LAS-2} and H_{EC} ; AVRC site.....	56
Figure 22. LAS to EC H comparison for LAS-2, August 28 th – Sept. 5 th and Sept. 21 st – Oct. 21 st ; AVRC site	57
Figure 23. Scatter plot for evaluation of MOST agreement, for LAS-1, -2, and -3; Timpas site	58
Figure 24. Scatter plot for evaluation of MOST agreement, for LAS-1; Andreas (1988), Thiermann and Grassl (1992), and Hill et al. (1992) f_T formulations shown for reference; Timpas site	59
Figure 25. Same as Fig. 24, modified for z_{LAS} equal to 2.48 m	60
Figure 26. Scatter plot for evaluation of MOST agreement, for LAS-2; Andreas (1988), Thiermann and Grassl (1992), Hill et al. (1992), and De Bruin et al. (1993) f_T formulations shown for reference; AVRC site.....	61
Figure 27. Same as Fig. 25, modified for z_{LAS} equal to 1.86 m	62
Figure 28. Same as Fig. 19c, showing only negative H_{LAS} and H_{EC}	68
Figure 29. Same as Fig. 19c, showing only positive H_{LAS} and H_{EC} less than 150 W m^{-2}	69
Figure 30. Bowen ratio (β , $H/\lambda E$) time series plots for Timpas and AVRC sites.....	74

Figure 31. Scatter plots showing relationship between C_T^2 and C_n^2 and positive H_{LAS} ; Timpas site
.....76

INTRODUCTION

Estimation of water evaporation and transpiration over a crop surface is an important part of irrigation water management in arid and semi-arid regions where typical rainfall does not support seasonal crop water needs. The timing and depth of applied irrigation water to a crop root zone will depend (often predominantly) on the rate of evapotranspiration (ET). Different techniques for estimation and measurement of ET have emerged in the last half century which range in level of accuracy and complexity. As the general level of technology and computing power increase, research methods befitting the current state of both have emerged, including Eddy Covariance, Scintillometry, and Remote Sensing. Satellite- and airborne-based remote sensing methods are unique in their capability to provide land surface maps of information which can lead to production of ET raster maps. Limiting the discussion to satellite-based methods, various image-capturing instruments include the Advanced Spaceborne Thermal Emission and Reflection Radiometer (**ASTER**, NASA/Japan METI, ERSDAC), **Landsat** (5 or 7, NASA/USGS), the Moderate Resolution Imaging Spectroradiometer (**MODIS**, NASA) and the Advanced Very High Resolution Radiometer (**AVHRR**, NOAA). These vary, in order, in spatial pixel resolution (generally) from high to low although the temporal resolution (frequency of image capture) tends to increase with decrease in spatial resolution (Landsat 5 TM 30/120 m, once every 16 days; AVHRR 1.09 km, two times per day¹). Remote sensing energy balance (RS-EB) algorithms demonstrate one way to incorporate remote sensing data for the estimation of ET. These methods use energy balance principles to compute ET as the residual of the available energy less the sensible heat flux at the surface (Eq. 1). A few examples of algorithms are described in Gowda et al. (2007), notably the Surface Energy Balance Algorithm for Land (SEBAL; Bastiaanssen et al.

¹ This information can be found on the respective websites for the image-capturing instruments

1998) and Mapping Evapotranspiration with Internalized Calibration (METRICTM; Allen et al. 2007). These two algorithms incorporate remotely sensed surface radiometric temperature (T_c , °C) and reflectance values with an inverse-calibrated model which back-calculates a dT ($T_0 - T_a$) profile at two extremes (dry/wet) in the image (Gowda et al. 2007). Lagouarde et al. (2002) obtained fair results in comparison with Large Aperture Scintillometer (LAS) fluxes using SEBAL and Gowda et al. (2008) showed fair results in comparison with soil moisture budget derived ET estimates using METRIC. For the purpose of validating RS-EB ET, large aperture scintillometry is considered an appropriate tool due to the relatively large spatial scale of measurement (Brunsell et al. 2011, Meijninger 2003, Lagouarde et al. 2002). A Large Aperture Scintillometer (LAS) yields a spatial average of sensible heat flux over path lengths up to 4.5 km. Nonetheless, for a heterogeneous landscape which varies in terms of surface roughness and moisture, caution must be taken to account for the variability especially in surface roughness input parameters within the LAS source area (Timmermans et al. 2009). The LAS is an instrument which captures turbulence in the near surface atmosphere by means of propagating an electromagnetic beam from transmitter to receiver. Using Monin-Obukhov similarity theory (MOST, see below), the LAS signal can be related to the surface sensible heat flux (H , $W m^{-2}$). Subsequently, representative measurements of net radiation (R_n , $W m^{-2}$) and ground heat flux (G , $W m^{-2}$) can be used to solve for latent heat flux (λE , $W m^{-2}$) as a residual (similar to the methodology of the RS-EB methods; Eq. 1). Other energy balance terms, such as storage and advection (horizontal energy transport), are considered negligible if the measurements are made close to the surface and the vegetation canopy is relatively low (Hoedjes et al. 2002, Solignac et al. 2009).

$$R_n - G = H + \lambda E \quad (1)$$

As indicated above, the LAS is dependent on MOST, which stipulates that conditions are horizontally homogeneous, stationary, and that fluxes are constant with height (Meijninger 2003). In order to determine LAS sensible heat flux (H_{LAS}), the effective path height (z_{LAS}) and length (L_{LAS}) must be known. For a relatively flat surface, the estimation of the path height is fairly trivial, but when the topography varies non-uniformly over the LAS path, more information is necessary to determine the effective height. Hartogensis et al. (2003) suggests that a weighted average of LAS beam heights along the path according to the given (LAS) path weighting function will yield a fairly accurate result provided that the variation in beam height along the path is not extreme. In any case, this requires knowledge of the topography along the LAS path. In addition, the LAS requires independent estimates of the Bowen Ratio² (β), friction velocity (u_* , m s⁻¹), and the condition of the atmospheric stability. The estimation of these variables may not be trivial and generally requires extra instrumentation. Moene et al. (2005) highlight that H is significantly impacted by β for $|\beta|$ less than 0.5, approximately, which would be the case for a well-irrigated surface. Sensible heat flux (H) is directly proportional to the friction velocity (u_*), suggesting the importance of accurate estimation of this variable. The value of u_* may be modeled with the logarithmic wind profile (LWP) or measured using a three-dimensional (3-D) sonic anemometer (Arya 2001). If horizontal wind speed measurement at only one height is available, estimation of u_* using the LWP relies further on estimation of the momentum roughness length (z_{om} , m) which is a characteristic of the land surface / vegetation type. For all cases with the LWP, an estimate of the zero displacement height (d , m) is required, which is also dependent on the presence and density of vegetation / surface roughness elements. The estimation of the atmospheric stability (i.e., whether H flux is directed upward or downward), is generally only uncertain for a few (30 minute) time steps during the morning and

² Bowen Ratio defined as ratio of sensible heat flux over latent heat flux.

afternoon atmospheric inversions. Nonetheless, over a well-irrigated surface where the magnitude of H is small, the determination of stability is often more uncertain. Finally, since H is a turbulent flux and is measured by the LAS within the surface layer, the measurement source area is not simply defined by the horizontal beam path but also by an area upwind of the path (Schmid 1994). The size of this is dependent on z_{LAS} (and L_{LAS}), surface roughness, and atmospheric stability. Thus, the representative area for the LAS comes into question when the extent of horizontal homogeneity is not large, and it may be necessary to monitor this area with a source area model (e.g. Kormann and Meixner 2001, Hsieh et al. 2000).

The evaluation of LAS performance has been undertaken (extensively) for both homogeneous and heterogeneous surfaces and some results from primarily homogeneous surfaces are described here. Results range from poor to good depending on LAS manufacturer and surface condition. Hoedjes et al. (2002) reported fair results for LAS sensible heat flux (H_{LAS}) against Eddy Covariance (EC) sensible heat flux (H_{EC}) for an irrigated homogeneous wheat surface surrounded by dry areas in Mexico (Table 1). Solignac et al. (2009) showed good results using a custom-calibrated LAS against an EC tower for drier conditions (June and September) over a wheat field in France (Table 1). Gowda (2010) has presented *preliminary* results of a Bushland, Texas study comparing flux data derived from weighing lysimeter ET with Kipp and Zonen LAS flux data, showing very poor results in irrigated conditions and fair results in dryland conditions (Table 1). Van Kesteren and Hartogensis (2011) reported sensible heat flux bias of +30% in the Kipp and Zonen LAS relative to a Wageningen University (Netherlands) designed LAS model. Kleissl et al. (2009) reported bias of +25% when comparing the Kipp and Zonen LAS to a Boundary Layer Scintillometer (BLS900, Scintec, Germany). Gowda (2010) (see Table 1) and

Kleissl et al. (2008) both also showed inter-LAS variability for the Kipp and Zonen LAS, where Kleissl et al. (2008) showed between 2-21% variability in H expressed in terms of the linear regression slope. Brunsell et al. (2011) reported fair to good results for a Kipp and Zonen LAS operating over a grassland surface in Kansas with a path length near 1 km, where elevation and soil water conditions were heterogeneous. Two EC stations were placed to represent the variation in moisture between upland and lowland areas, and the resulting flux magnitudes from the LAS,

Table 1. Results from selected LAS studies.

Study	Results (H , $W m^{-2}$; ET , mm)	Comments
Hoedjes et al., 2002	Unstable: $H_{LAS} = 0.982 \times H_{EC} - 1.63$, $r^2=0.94$; $\lambda E_{LAS} = 1.02 \times \lambda E_{EC} - 2.61$, $r^2=0.97$; Stable+Advection daytime: $H_{LAS} = 1.02 \times H_{EC} + 2.69$, $r^2=0.81$; $\lambda E_{LAS} = 0.92 \times \lambda E_{EC} + 12.2$, $r^2=0.99$	The EC H and λE fluxes were corrected using the Bowen Ratio Energy Balance Closure method (Twine et al. 2000) except during stable + advective conditions, the method was not applied to EC (very small) H fluxes
Solignac et al., 2009	April: $H_{LAS} = 1.02 \times H_{EC}$, $r^2=0.74$, RMSE=7.9; June: $H_{LAS} = 0.99 \times H_{EC}$, $r^2=0.95$, RMSE=17.4; September: $H_{LAS} = 1.02 \times H_{EC}$, $r^2=0.91$, RMSE=26.3	April data showed poorer results since Bowen Ratio (β) was small – the near one-to-one slope may be spurious since 30 min. (β) values were derived from the EC data
Gowda, 2010	Dryland cotton: $ET_{LAS} = 1.1042 \times ET_{LYS}$, $r^2=0.77$; Irrigated cotton: $ET_{LAS} = 0.4126 \times ET_{LYS}$, $r^2=0.32$	Inter-LAS variability of 15-20% noted (Kipp and Zonen LAS); preliminary study results
Van Kesteren and Hartogensis, 2011	$H_{WagLAS} = 1.07 \times H_{EC} + 4.8$, $r^2=0.968$; $H_{LAS(K+Z)} = 1.37 \times H_{EC} + 21$, $r^2=0.96$	Wageningen University designed LAS outperforms Kipp and Zonen LAS
Brunsell et al., 2011	Upland EC: $H_{LAS} = 0.94 \times H_{EC}$, $r^2=0.96^*$, RMSE=7.4, MBE= -6.2; Lowland EC: $H_{LAS} = 0.86 \times H_{EC} + 25.9$, $r^2=0.84$, RMSE=13.6, MBE=17.7	Bias errors show that H_{LAS} was in between EC_{up} and EC_{low} H fluxes (Kipp and Zonen LAS)

*Brunsell et al. (2011) indicate “correlation” or “overall correlation”, assumed here to be r^2 .

which spanned upland and lowland areas, were in between the flux magnitudes for the EC stations. This suggested successful flux averaging by the LAS, and further, RMSE values for H were less than $15 W m^{-2}$ between the LAS and the two EC stations (Table 1).

The EC method is a direct way of measuring latent (evaporative) and sensible heat fluxes using high frequency measurements of water vapor concentration, air temperature, and vertical wind speed. A more complete description of the EC method is given in the methodology section. A typical setup may consist of a 3-D sonic anemometer and a hygrometer which are mounted together within the surface boundary layer. Despite its prevalent use, the EC method has been criticized for underestimation of the sum of sensible (H) and latent (λE) fluxes, which corresponds to failing to close the energy balance (Foken 2008a). This can be reported as the ratio of the sum of H and λE divided by the difference of R_n and G , which is referred to as the energy balance closure ratio (EBCR; Eq. 2). The formulation of Eq. 2 is based on the same assumptions made in Eq. 1 to neglect other components of the surface energy balance.

$$\text{EBCR} = \frac{H + \lambda E}{R_n - G} \quad (2)$$

Twine et al. (2000) reported an EBCR of 70 to 90 percent for EC instruments from different manufacturers set up over multiple surfaces with relatively short or no vegetation (0-1 m vegetation height) during summertime in Oklahoma. The same authors also, nonetheless, indicated some studies where a good EBCR was obtained (Jarvis et al. 1997, Unland et al. 1996, Wright et al. 1992) although it is not readily clear the reason for the good closure. Wilson et al. (2002) evaluated the performance of 22 FLUXNET (<http://fluxnet.ornl.gov/>) eddy covariance deployments in the US and Europe in terms of EBCR. The evaluation was mostly of forested sites, although data from sites including agriculture, tundra, and rangeland land use were included. The mean regression slope between ($H + \lambda E$) values and ($R_n - G - S$) (where S is canopy storage) values was reported to be 0.8 for daytime data, which approximately represents

an 80% EBCR. They observed a maximum slope of 0.97 and minimum of 0.56. Wilson et al. (2002) also reported an improvement in the EBCR over the course of the day, which was near 1.0 between 16:00 – 17:00. Schuettemeyer (2005) showed long term daytime EBC of 97% for an EC setup (10 m height) over grassland with some trees (5-8 m height) in a semi-arid region in West Africa after the rainy season. However, he showed a 77% EBCR when examining only the afternoon periods, in contrast to the good EBCR found by Wilson et al. (2002) during afternoon periods. Some common assertions regarding the lack of energy balance closure include the following: (1) The source areas of the energy balance components do not match and/or the energy balance neglects components which may be significant such as heat storage and/or advection; (2) The eddy covariance method suffers from ‘missing’ low/high frequency eddy structures due to the temporal and spatial scale of the turbulent eddies (Wilson et al. 2002, Twine et al. 2000). The latter assertion suggests a limitation of the EC method for accurate estimation of turbulent heat fluxes, although a lack of energy balance closure in general does not absolutely invalidate EC accuracy (Allen et al. 2011). Despite the common issues with energy balance closure, use of the eddy covariance method is prevalent likely because of the advantage of continuous, direct measurement of turbulent H and λE fluxes. It is also observed to be the common method for evaluation of LAS H (and λE) (Brunsell et al. 2011, Van Kesteren and Hartogensis 2011, Solignac et al. 2009, Schuettemeyer 2005, Hoedjes et al. 2002, Green and Hayashi 1998, etc.).

STUDY OBJECTIVES

The primary purpose of this study was to evaluate the performance of the Kipp and Zonen LAS for estimation of H by means of two case studies. The first case study tested LAS performance

over predominantly dry, homogeneous grassland, providing a near-optimum evaluation environment. In addition, three LAS units were deployed together in the first case study. The second case study tested the LAS performance for a single LAS over irrigated alfalfa. This experiment provided an opportunity to evaluate LAS performance when H fluxes were small, and further incorporated issues of source area heterogeneity (between LAS and reference). An eddy covariance (EC) system was deployed during both case studies to facilitate the evaluation of LAS performance³. Based on results from previous studies, the following results are expected: The LAS may overestimate sensible heat flux (Kleissl et al. 2009, Van Kesteren and Hartogensis 2011); sensible heat flux from the three LAS units at the first study site may be significantly different (Kleissl et al. 2008; Gowda 2010; Van Kesteren and Hartogensis 2011); LAS performance may be better for the case study over dry terrain than the study over irrigated crops (Solignac et al. 2009; Gowda 2010). The specific study objectives are listed below:

1. Evaluate inter-LAS variability for estimation of sensible heat flux (H)
2. Evaluate absolute LAS accuracy to estimate H (with H_{EC})
3. Evaluate estimation of friction velocity (u_*) by LWP (with EC u_*)
 - This includes estimation of u_* by LWP with two levels of wind speed measurement and with only one level of wind speed measurement
4. Compare performance of LAS over irrigated and non-irrigated terrain
5. Sub-objectives:
 - Evaluate the uncertainty of H predicted by the LAS (H_{LAS}) based on input uncertainties
 - Evaluate the sensitivity of H_{LAS} to changes in input variables

³ EC sensible heat (H) fluxes were not adjusted for lack of energy balance closure before comparison to H_{LAS} .

- Evaluate the agreement of LAS output with the prescribed MOST similarity function⁴

⁴ Refer to methodology section for description of MOST similarity function.

METHODOLOGY

LARGE APERTURE SCINTILLOMETER THEORY

The Kipp and Zonen LAS functions by transmitting an electromagnetic beam between a source unit (transmitter) and a receiver of equal aperture diameter. The propagation of the beam through the lower atmosphere is affected by turbulence resulting from gradients of temperature, humidity, and to a lesser degree, pressure. Wang et al. (1978) described the relationship between the variance of the beam intensity (σ_{int}^2) sensed at the receiving unit and the structure parameter of the air refractive index (C_n^2 , $\text{m}^{-2/3}$) for a LAS (Eq. 3)⁵.

$$C_n^2 = 1.12 \sigma_{\text{int}}^2 D^{7/3} L_{\text{LAS}}^{-3} \quad (3)$$

In Eq. 3, D is the LAS aperture diameter (0.152 m) and L_{LAS} is the LAS path length (m). The structure function is a measure of the change in a variable and thus C_n^2 represents the change in the air refractive index resulting from the turbulence structures described above. The C_n^2 value resulting from Eq. 3 is a weighted average which carries strongest weight in the path center. The Kipp and Zonen Large Aperture Scintillometer (LAS) operates at a near-infrared wavelength (880 nm) and is considered in this regime to be primarily affected by turbulence from temperature fluctuations (Moene et al. 2005). This permits a relatively straightforward approximation of the temperature structure parameter (C_T^2) from C_n^2 with additional input of the

⁵ In order for Eq. 3 to be valid, Moene et al. (2005) explain criteria which should be met including: $D/l_0 > 30$, $L_0/D > 10$, and $D > 2(AL)^{1/2}$, where D is aperture diameter (m), l_0 represents the eddy size separating the inertial range of turbulence from the dissipation range (m), L_0 represents the eddy size separating the inertial range from the production range of turbulence (m), A is the electromagnetic wavelength (m), and L is the path length (m). Moene et al. (2005) also notes that L_0 can be estimated as the height of the LAS beam from the surface.

Bowen Ratio (β). Note from Eq. 4 that the use of β in the LAS method is indirect⁶ – i.e. H is not derived directly from the input of β . In Eq. 4 and the definition of A_T , T is air temperature (K), BP is barometric pressure (Pa), R_v is the water vapor gas constant (461.5 J kg⁻¹ K⁻¹) and q is specific humidity (kg kg⁻¹). After obtaining C_T^2 , a Monin-Obukhov similarity function derived for the C_T^2 parameter (Andreas 1988) is employed to derive the temperature scale (T^* , K; Eq. 5). In Eq. 5, f_T represents the MOST function, which is uniquely defined for unstable and stable atmospheric conditions. Further, z_{LAS} is LAS effective beam height (m), d is the zero displacement height (m), and L_{mo} is the Obukhov stability length (m; described below).

$$C_T^2 = \frac{T^2}{A_T^2} \cdot \frac{C_n^2}{\left(1 + \frac{0.03}{\beta}\right)^2}, \quad (4)$$

$$\text{where } A_T = -0.78 \times 10^{-6} \left(\frac{BP}{T}\right) + 0.126 \times 10^{-6} (R_v q)$$

$$T^* = \left(\frac{C_T^2 \times (z_{LAS} - d)^{\frac{2}{3}}}{f_T \left(\frac{z_{LAS} - d}{L_{mo}}\right)} \right)^{\frac{1}{2}} \quad (5)$$

In order to finally calculate sensible heat flux from the LAS data, further input of the friction velocity (u_* , m s⁻¹; Eq. 6) is necessary⁷;

$$u_* = \frac{k_v \times (U_2 - U_1)}{\ln\left(\frac{z_2 - d}{z_1 - d}\right) - \psi\left(\frac{z_2 - d}{L_{mo}}\right) + \psi\left(\frac{z_1 - d}{L_{mo}}\right)}, \quad (6)$$

⁶ The formulation of Eq. 4 was suggested by Wesely (1976) and explained in detail in Moene et al. (2005). It involves assumptions regarding the correlation of temperature and humidity, which can be summarized by the assumption that (the absolute value of) the temperature and humidity correlation coefficient ($|r_{Tq}|$) is equal to 1. Wesely (1976) also gives an alternate formulation for r_{Tq} equal to 0 as $C_T^2 = (C_n^2 T^2 / A_T^2) / (1 + (0.03/\beta)^2)$.

⁷ It is worth clarification that the definition provided for u_* is applicable if the LWP method is used to derive u_* (rather than, e.g., measurement by a 3-D sonic anemometer).

where U is the horizontal wind speed at the lower (1) and upper (2) levels (m s^{-1}), z is the wind speed height at level 1 and 2 (m), and k_v is the Von Karman constant (0.41). Similar to T_* in Eq. 5, u_* is dependent on MOST for non-neutral atmospheric conditions – this dependence is accounted for with ψ in Eq. 6. Both f_T and ψ are functions of the stability parameter (z/L_{mo}), where z (m) represents the height of the LAS or wind speed measurement over the zero displacement height (d , m), and are defined along with L_{mo} in Equations 8-10. As mentioned in the introduction, u_* can be computed with just one level of wind speed measurement by replacing U_1 with zero (m s^{-1}) and z_1-d with z_{om} (m). After obtaining u_* and T_* , the sensible heat flux (H , W m^{-2}) can be calculated as shown in Eq. 7 (Meijninger 2003), where ρ_{air} is the moist air density (kg m^{-3}) and c_p is the specific heat of dry air at constant pressure ($\sim 1005 \text{ J kg}^{-1} \text{ K}^{-1}$).

$$H = -\rho_{air} c_p u_* T_* \quad (7)$$

The Monin-Obukhov similarity theory provides a method to characterize turbulent exchange in a thermally stratified surface layer (Arya 2001). Thermal stratification means that there is a gradient of temperature increasing (stable atmosphere) or decreasing (unstable atmosphere) with height. Generally, during the daytime, radiation from the sun heats the land surface more quickly than the near-surface air, causing unstable conditions to develop in which sensible heat flux (H) is directed upward into the air. Subsequently, when the radiation source is cut off in the evening, the surface cools more quickly than the near-surface air and stable conditions develop where H is directed toward the surface. Neutral atmospheric conditions are represented by the lack of a temperature gradient (i.e. constant temperature in the surface layer). Daytime neutral (or stable) conditions can develop where surface temperature is influenced by the presence of moisture and

subsequent high evaporation/transpiration (ET). By dimensional analysis, profiles of temperature, momentum, and water vapor can be described as a unique function of the above mentioned dimensionless stability parameter (z/L_{mo} ; Arya 2001 Arya). The definition of L_{mo} (Eq. 8) demonstrates that the variable is a ratio of mechanical (u_*) to buoyant (convective; T_*) turbulence, and has been described by Arya (2001) as the thickness of the layer near the surface affected by mechanical (wind shear) turbulence. In Eq. 8, T is air temperature (K), g is the earth gravitational acceleration constant (9.81 m s^{-2}), and k_v is the same Von Karman constant found in Eq. 6.

$$L_{mo} = \frac{u_*^2 T}{g k_v T_*} \quad (8)$$

It is apparent in Equation 6 that L_{mo} is a function of u_* and T_* , which requires that Eqs. 5, 6, and 8 are solved in an iterative fashion. Similarity functions of z/L_{mo} have been empirically derived from field experiments (e.g. 1968 Kansas Field Program, Izumi 1971 via Arya 2001) which permit description of surface fluxes as a function of corresponding vertical profiles and vice versa (i.e./e.g. f_T and ψ described above). The similarity function used for u_* in this study (ψ ; Eq. 9) was recommended by Dyer (1974) and is only slightly different from the formulation given in Arya (2001). Note that the function is defined differently for unstable ($L_{mo} < 0$) and stable ($L_{mo} > 0$) conditions. In Eq. 9, z is written generically but refers to either z_1 or z_2 and must be distinguished from z_{LAS} . More directly applicable to the LAS theory is the similarity function (f_T) used to relate C_T^2 , which represents the temperature profile, to the surface sensible heat flux (H) via the temperature scale (T_*). For this study, the relationship given by Andreas (1988) was used (Eq. 10). It is worth clarification that, rigorously, the temperature gradient applicable to surface

sensible heat flux is expressed in terms of the potential temperature (θ). However, for observations close to the surface, replacing θ with T and neglecting adiabatic temperature lapse will not incur serious error (Arya 2001).

$$\psi\left(\frac{z-d}{L_{mo}}\right) = \begin{cases} 2 \ln\left(\frac{1+x}{2}\right) + \ln\left(\frac{1+x^2}{2}\right) - 2 \tan^{-1}(x) + \frac{\pi}{2}, & L_{mo} < 0 \\ -5 \times \frac{(z-d)}{L_{mo}}, & L_{mo} > 0 \end{cases} \quad (9)$$

$$x = \left(1 - 16 \times \frac{(z-d)}{L_{mo}}\right)^{\frac{1}{4}}$$

$$f_T\left(\frac{z_{LAS}-d}{L_{mo}}\right) = \begin{cases} 4.9 \times \left(1 - 6.1 \times \frac{(z_{LAS}-d)}{L_{mo}}\right)^{-\frac{2}{3}}, & L_{mo} < 0 \\ 4.9 \times \left(1 + 2.2 \times \left(\frac{(z_{LAS}-d)}{L_{mo}}\right)^{\frac{2}{3}}\right), & L_{mo} > 0 \end{cases} \quad (10)$$

Since the LAS instrument does not sense the direction of H , upward or downward, post-processing requires independent estimation of the atmospheric stability condition to derive a unique H solution (i.e. computations for Eqs. 5-10 yield an unstable and stable solution of H , T_* , u_* , and L_{mo} for each time step). For determination of the atmospheric stability condition, measurement of the near-surface air temperature profile is preferred, but in the absence of this measurement, the output signal of the LAS (C_n^2 , $m^{-2/3}$) can be analyzed for morning and evening atmospheric inversions (Hoedjes et al. 2002).

EDDY COVARIANCE THEORY AND METHODS

The Eddy covariance method is based on the principles of turbulent motion in the surface boundary layer. Foken (2008b) describes that for turbulent motion, the Navier-Stokes equations of motion must undergo Reynold's decomposition, for which the variables are defined equal to the mean plus variance ($x + x'$). Further, within the constant flux (surface) layer, it appears that other flux terms in the Navier-Stokes equations can be disregarded such that only turbulent fluxes need to be considered (Foken 2008b). Finally, with the assumption of zero mean vertical wind speed, the turbulent flux of a variable can be described solely in terms of the covariance of the variable with the vertical wind speed (Foken 2008b)⁸. This can be used to describe the turbulent fluxes of momentum (τ), sensible heat (H), and latent heat (λE) (Eqs. 11-13).

$$H = \rho_{\text{air}} c_p \overline{w'T'} \quad (11)$$

$$\lambda E = \rho_{\text{air}} \lambda \overline{w'q'} \quad (12)$$

$$\tau = -\rho_{\text{air}} \overline{w'u'} \quad (13)$$

In these equations, $\overline{w'x'}$ is the covariance of the vertical wind speed (w) with the corresponding variable (x) of air temperature (T , K), specific humidity (q , kg kg⁻¹), or horizontal wind speed (u , m s⁻¹). In this case, u is the wind speed along the mean direction, such that the other horizontal

⁸ Foken (2008b) shows five postulates (requirements) of Reynold's decomposition, where the second is considered the basis for the eddy covariance method, given as $\overline{xy} = \overline{x\bar{y}} + \overline{x'y'}$, where y could represent the vertical wind speed (w), x the flux variable, and x' and y' represent the variances; For \overline{xy} representing the total flux, it is apparent that if $\bar{w} = 0$, the total flux is defined solely in terms of the covariance term.

wind component (v) has a mean of zero⁹. The other variables are as described for the LAS, with exception of the latent heat of vaporization (λ , J kg⁻¹). It is notable that the friction velocity (u_* , m s⁻¹) can be defined in terms of the momentum flux (τ) (Eq. 14; Foken 2008b).

$$u_* = \left(\frac{\tau}{\rho_{\text{air}}} \right)^{\frac{1}{2}} \quad (14)$$

The eddy covariance (EC) method requires sampling frequency of at least 10 Hz (readings per second). Further, Foken (2008b) recommends an averaging interval of 30 minutes to account for low frequency eddies and to maintain the theoretical requirement of steady-state (stationary) conditions. In this study, a 3-D sonic anemometer (CSAT3, Campbell Scientific, Inc. (CSI), Logan, UT) was used to measure the wind speed in three orthogonal directions (u , v , w ; m s⁻¹) and the sonic temperature (T_s , K). An ultraviolet krypton hygrometer (KH20, CSI, Logan, UT) was used to measure the water vapor concentration (or specific humidity, q , kg kg⁻¹). Measurements were made at 10 Hz frequency and processed for averaging intervals of 30 and 60 minutes. The EC data were processed and post-processed using EdiRe® software (Clement 1999). The processing was performed accounting for the following, fairly standard, procedures. The u , v , w , and T_s raw signals were de-spiked to remove outliers. Subsequently, with a user-input of the CSAT3 azimuth, the x and y wind speed were used to derive a vector average wind speed and wind direction. Further, a double coordinate rotation method (Kaimal and Finnigan 1994) was used to rotate the wind coordinates such that the vertical wind component was perpendicular to the plane of mean wind velocity. The KH20 data were lagged so that the

⁹ The computation of u_* in this study was performed using the covariance of the u and v portions of the horizontal wind speed, even though coordinate rotation had set v approximately equal to zero.

recorded data were aligned in time with the CSAT3 data. Subsequently, the covariance values of temperature, vapor concentration, and horizontal wind speed (u , v) with the vertical wind speed (w) were computed for the averaging interval. Corrections which were iteratively included in the processing include frequency response correction (Moore 1986) and density correction (Webb et al. 1980). Further, the sonic temperature (T_s) heat flux correction to transform the T_s flux ($\overline{w'T_s'}$) to air temperature flux ($\overline{w'T'}$) was performed after Schotanus et al. (1983). These corrections were iterated three times within the EdiRe protocol. Data quality control parameters were computed based on the steady state (stationarity) test and integral turbulence characteristics test (ITT) proposed by Foken and Wichura (1996). The same authors suggest the data quality is good if the experimental data do not violate the theoretical standard by more than 30%. It is notable that the EC raw data were processed by Stuart Joy (M.S. Civil Engineering, CSU, Fall 2011).

EXPERIMENTAL SITE AND METHODS

During the summer and fall of 2011, experiments were carried out in southeastern Colorado with three Kipp and Zonen LAS units. One of these (LAS-1) was first deployed in 2009, while LAS-2 and -3 were first deployed in 2010. The first experiment was carried out at a dry, flat grassland site near Timpas, CO (Lat. 37.8173, Long. -103.82304) and involved the inter-comparison test of the three LAS units, along with comparison to a reference EC unit. The second experiment was performed at the Colorado State University (CSU) Arkansas Valley Research Center (AVRC) near Rocky Ford, CO (Lat. 38.03779, Long. -103.68941) and involved the deployment of one LAS unit (LAS-2) and an EC unit. Figure 1 shows the study locations in Colorado. Some photos of the experiment sites are shown in Appendix 11.

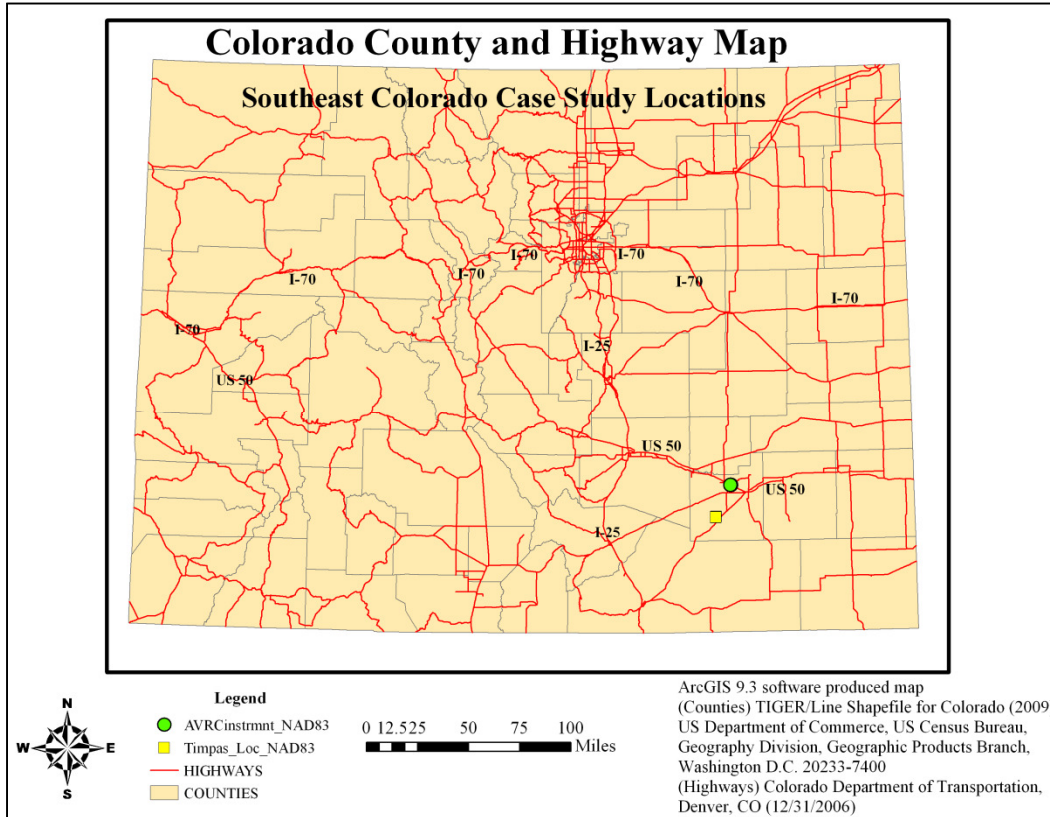


Figure 1. 2011 LAS study sites shown for reference to location within Colorado. (Yellow) square represents Timpas, CO site and (green) circle represents AVRC site near Rocky Ford, CO – Both sites are in Otero County, near the Arkansas River and US Route 50.

SITE 1 (TIMPAS, CO)

The Timpas, CO site is at an elevation of approximately 1370 m and is relatively flat over the area of study. LAS-1 was installed and operational at the Timpas site from July 2nd to October 21st, 2011 (Figure 2). LAS-2 and LAS-3 were also installed at the Timpas site by July 2nd on a parallel path to LAS-1¹⁰. In each case, the LAS path length was near 600 m. The setup height of the units was approximately 2.25 m, although the effective beam height of the LAS path would depend on the topography between the transmitter and receiver (see App. 2). The vegetation cover at Timpas was dry and did not seem to change significantly over the study period. There

¹⁰ A description of the general setup and alignment procedure for a LAS is given in Appendix 1.

was a mix of short grass (9 cm approx.) and tall grass (25 cm approx.), along with occasional shrubs and cactus bushes (0.4 -1.2 m approx.). Approximately 76 mm of rainfall were recorded over the study period. The soil type (Web Soil Survey, USDA, NRCS) is a Manvel Silt Loam with an estimated bulk density of 1.225 g cm⁻³. On August 3rd, LAS-2 was moved to site 2 (AVRC near Rocky Ford, CO) and LAS-3 was also moved to a different research location.

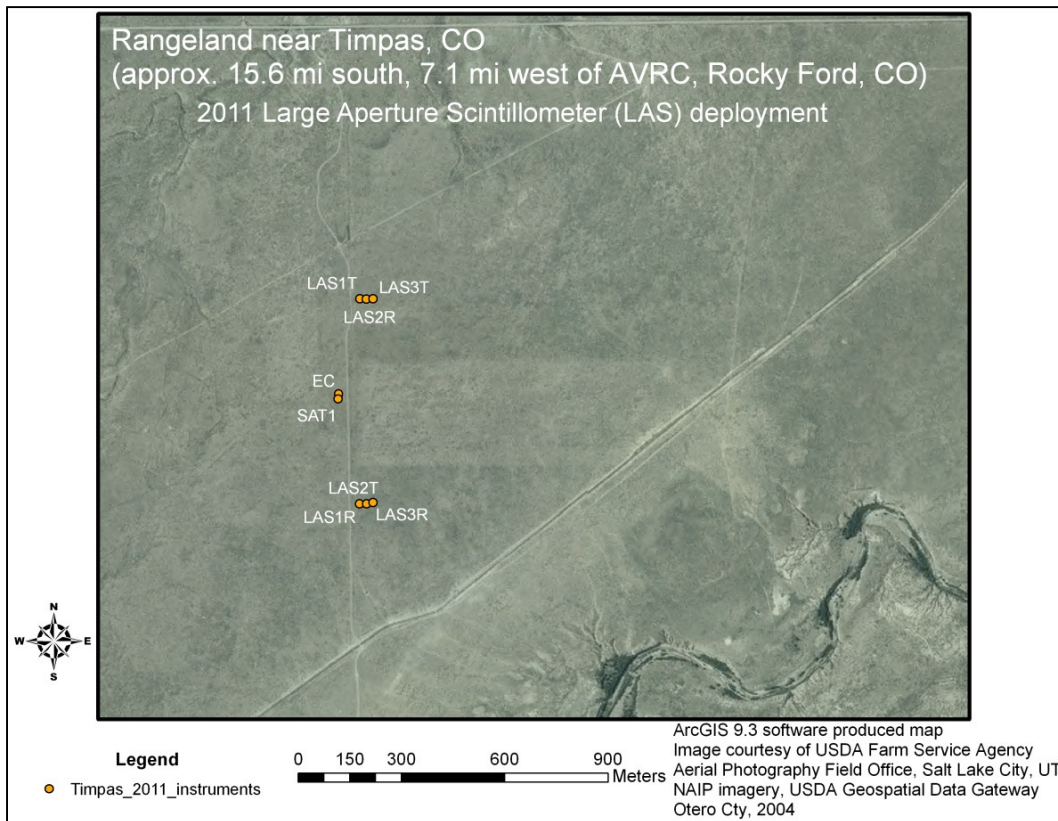


Figure 2. Aerial image overview of the Timpas grassland site. An access (dirt) road ran parallel to the LAS paths, in between the LAS units and the EC and SAT towers. LASxT represents LAS transmitter and LASxR represents LAS receiver.

An aerodynamic profile (SAT) tower was installed to capture information on the vertical gradients of temperature, humidity, and wind speed. Six levels (1 m – 6 m approx.) were outfitted with air temperature and relative humidity sensors (Vaisala, Inc. HMP45C, CSI, Logan, UT) and wind speed cup anemometers (R.M. Young Wind Sentry 03101, CSI, Logan, UT). The

SAT tower at the Timpas site was operational from July 8th to October 21st, although nearly all sensors appeared to stop functioning after October 3rd, which may be attributed to a power supply issue. An eddy covariance (EC) unit was operational from July 8th to August 26th at the Timpas site, after which it was moved to the AVRC site. The SAT and EC towers were installed approximately 40 m west of the closest LAS path, and at the approximate north-south path center (Figure 2). The LAS paths were spaced approximately 20 m apart, horizontally. At the SAT tower and the LAS-1 receiver ancillary instrumentation to measure net radiation (NR-Lite, Kipp and Zonen, CSI, Logan, UT), radiometric surface temperature (IRT SI-111, Apogee, CSI, Logan, UT), soil heat flux (REBS HFT3, CSI, Logan, UT), soil temperature (T107, CSI, Logan, UT), and soil moisture (CS616, CSI, Logan, UT) was installed. Finally, barometric pressure (CS106, Vaisala BAROCAP, CSI, Logan, UT) and precipitation (TE525, CSI, Logan, UT) were measured at the LAS-1 receiver.

SITE 2 (AVRC, ROCKY FORD, CO)

The Colorado State University Arkansas Valley Research Center (AVRC; elevation 1274 m) is located just southeast of Rocky Ford, CO in an irrigated agriculture region which follows the Arkansas River. During the 2011 growing season, several different crops were grown at the AVRC, including corn, alfalfa, and forage sorghum. It is notable that two large monolithic weighing lysimeters were installed in two different (adjacent) alfalfa fields and were operational over the entire 2011 growing season. LAS-2 was installed on August 4th across the same two alfalfa fields with a path length of approximately 460 m and was operational until October 22nd. The height of the transmitter and receiver was approximately 2.25 m, similar to the setup at Timpas. In the southwest alfalfa field, an SAT tower identical to the one in Timpas was installed at the north end over the entire 2011 growing season. On August 27th, the EC unit was installed

approximately 10 m west of the SAT tower, immediately following an alfalfa cutting. In addition, two stations for measurement of net radiation (R_n) and soil heat flux (G) were installed and operational in the northwest corners of the two alfalfa fields, one on August 27th and the other September 7th. Two further stations for measurement of R_n and G were available as part of the weighing lysimeters' ancillary instrumentation. The net radiometers included one 4-way model (Kipp and Zonen CNR1, CSI, Logan, UT), one NR-Lite (Kipp and Zonen, CSI, Logan, UT), and two Q7.1 models (REBS, CSI, Logan, UT). Soil heat flux (SHF) instrumentation included SHF plates (REBS HFT3, CSI, Logan, UT), soil temperature thermocouples including Type E (TCAV, CSI, Logan, UT) and type T (HTMTSS-125(G)-6, Omega Inc., Stamford, CT), and soil moisture sensors (CS616, CSI, Logan, UT). Barometric pressure was measured at one of the lysimeter stations (CS105, Vaisala PTB101B, CSI, Logan, UT). An aerial overview of the experimental setup at the AVRC is shown in [Figure 3](#). The image date was likely in June or July of 2011. The 'SW/NE ancill' points represent the approximate locations of the ancillary R_n and G measurement stations. The 'SW/NE Lys' points represent the weighing lysimeters, where additional R_n and G measurements were made. The (SW and NE) alfalfa fields are those which contain the instrumentation points. Fields south of study fields were corn, fields directly east and south of study fields were planted in July with forage sorghum, the field directly north and west of study fields was forage sorghum (receiving more than one cutting in 2011), the field directly west of the latter was corn, and the field directly west of the SW alfalfa field was onion. With exception of the SAT tower and weighing lysimeters, sensors were shut down and removed from the fields by October 22nd. There were issues during the 2011 growing season especially in the southwest alfalfa field with some dry patches developing due to irrigation water not reaching the locations ([Figure 3](#)). Further, the northeast field alfalfa had only been planted in August 2010,

and is considered to have been still to some degree in the developing stage during the 2011 growing season (the crop height records showed the northeast field growth to lag behind that of the southwest field). Also, because the irrigations did not occur for both alfalfa fields at the same time, there was further potential for heterogeneous moisture conditions between both fields. Nonetheless, examination of net radiation and surface temperature data from both fields for the period of record appears to show that canopy cover became similar from September 22nd to October 22nd, approximately.

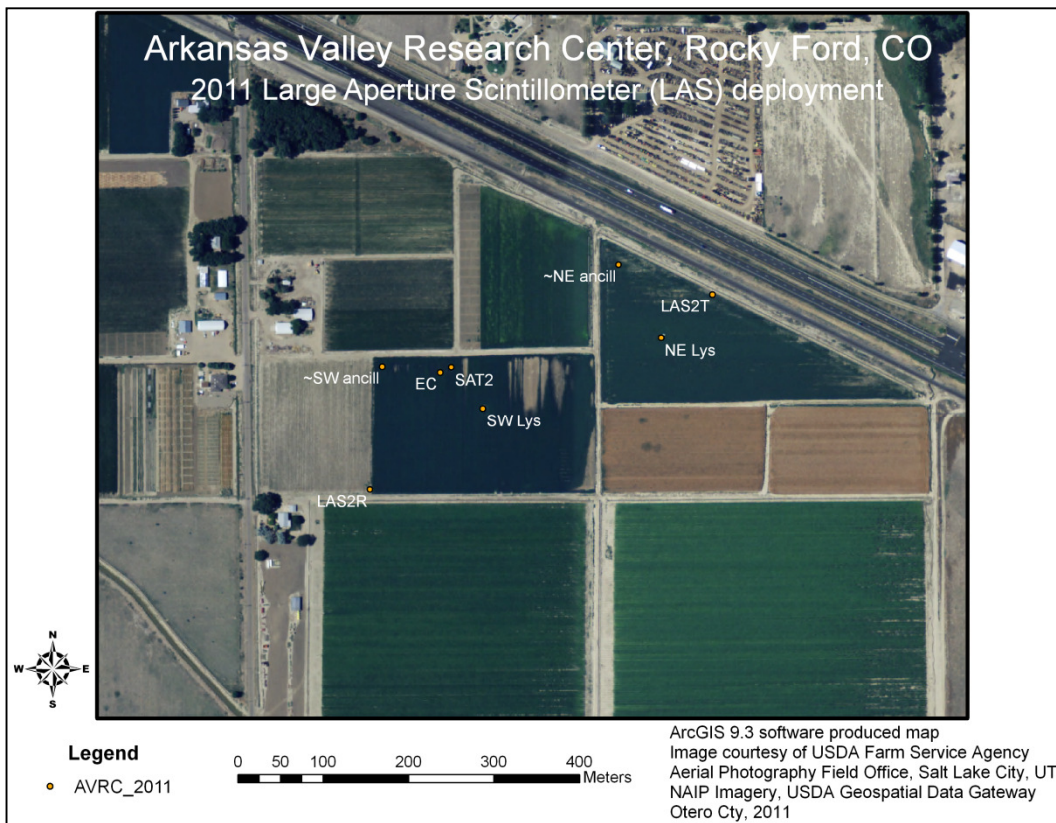


Figure 3. Aerial image overview of the AVRC site showing the instrument locations for the 2011 deployment.

LAS DATA PROCESSING METHODS

FIELD DATA COLLECTION AND RAW DATA PREPARATION

Site visits were performed after the initial installation (July 2nd) on July 8th, 21st, August 3rd-4th, 26th-27th, September 16th-17th, October 11th, and 21st-22nd. These visits were used to re-locate/install instruments, monitor instrument status, and collect data. Data were stored on a CSI CR1000 or CR3000 data logger, generally outfitted with a CSI CFM100 storage module for external Compact Flash (CF) card data storage, and powered by a deep cycle marine battery connected to a solar panel. Meteorological (T , RH , U) data and LAS data were stored at 1 Hz frequency, while other variables were sampled at 1 Hz frequency and internally averaged for storage at 15 or 30 minute intervals. Further, 15 minute averages of meteorological data were computed internally and stored, in addition to the 1 Hz data storage. The primary LAS output signal (U_{Cn2} , Volts (V)) represents the $\log(C_n^2)$ signal, computed by the LAS receiver electronics. The secondary LAS output signal ($Demod$, millivolts (mV)) represents the signal strength, which was used as a quality control (QC) parameter. The interval average value of C_n^2 used for data processing was computed with Eq. 15,

$$C_n^2 = 10^{(U_{Cn2} - 12 + 1.15 \times Var_{U_{Cn2}})} \quad (15)$$

where $Var_{U_{Cn2}}$ is the signal variance over the averaging interval (V^2). Microsoft Office ExcelTM software (hereafter Excel) was used to compute 30 minute average and variance values for U_{Cn2} , and 30 minute average values for $Demod$ using the 1 Hz stored data. Some data quality control parameters were monitored in this process to count samples which did not meet specific criteria,

including *Demod* less than 50 mV, U_{Cn2} greater than 0 V, and NAN (no record) values¹¹. The 15 minute meteorological data were also averaged to 30 minute values in Excel.

ANCILLARY DATA PREPARATION

The methods for determination of additional inputs necessary for the LAS data processing are described below, although in some cases further explanation of the methods is provided in the Appendices section.

LAS Path Length and Beam Height

The LAS path length values were retrieved from northing and easting field readings using a handheld Garmin eTrex GPS unit, whose accuracy was generally ± 4 m. The LAS effective beam height was taken as the average of the measured height of the transmitter and receiver units. The LAS height was also alternatively derived according to path length topography and the LAS path weighting function. For details of this method, the reader is referred to Appendix 2. The effect on H_{LAS} from using the alternative LAS height was tested for both study sites.

Momentum Roughness Length and Zero Displacement Height

In order to estimate canopy roughness parameters for both sites, vegetation heights were sampled periodically at different locations within the LAS path area. For the Timpas site, vegetation sample heights were recorded on July 1st, 21st, August 26th, and Sept. 16th. For the AVRC site, the field crop height was sampled approximately weekly or bi-weekly by Lane Simmons (AVRC) near the weighing lysimeter in the southwest and northeast alfalfa fields. In addition, the crop height was sampled at multiple locations in both the southwest and northeast alfalfa fields on Sept. 17th. For the Timpas site, the effective vegetation height was somewhat difficult

¹¹ Optimum alignment $|Demod| = 375$ mV, and manufacturer recommends low *Demod* limit to avoid issues associated with LAS misalignment; Manufacturer U_{Cn2} range: $-5 < U_{Cn2} < 0$ V

to discern, based on the nature of the grasses having variable heights. First, the effective height of the taller grasses and shorter grasses were individually determined for the study area. Finally, the area effective vegetation height was determined as the average of the ‘tall grass’ (0.25 m), ‘short grass’ (0.09 m), and bare surface (0 m) heights. Further, the vegetation height was assumed to be static over the study period, which was probably a reasonable assumption, since the site was not irrigated. For the AVRC site, the samples recorded by Lane Simmons were used to represent the effective field crop heights, based on fair agreement between these samples and the independent (extensive) sampling on Sept. 17th. This neglected the impact of any portion of the fields which were not growing as well (as the Simmons sample locations). Linear interpolation between the sampling dates was used to estimate daily crop height. Finally, the effective crop height for the LAS path was estimated as a weighted average of the southwest (67%) and northeast (33%) alfalfa fields, since the LAS path length was approximately two-thirds in the southwest alfalfa field. This did not account for the LAS path weighting function, but was assumed acceptable, based on uncertainties associated with the LAS source area. Once the effective vegetation height was determined for both sites, momentum roughness length (z_{om} , m) and zero displacement height (d , m) were estimated as $0.123 \times h_c$ and $0.67 \times h_c$, respectively, where h_c represents the effective vegetation height (Brutsaert 1982).

Bowen Ratio Methods

In order to compute C_T^2 from LAS C_n^2 output, input of the Bowen Ratio (β) was necessary – the relative impact of β on H_{LAS} is dependent on the magnitude of β (Eq. 44), but (as mentioned in the introduction) is relatively small for β greater than 0.5 (Moene et al. 2005). Initial daytime input for the Bowen ratio (β) was estimated using information on wetting events (irrigation, precipitation) as well as crop growth stage for the AVRC site. Basically, following wetting events, a low(er) value of β was assumed. In addition, as crop height increased at the AVRC site,

transpiration was considered to increase, so that a lower value of β was assumed. Some consideration was given to the expected magnitude of the surface energy balance fluxes for the above conditions in order to estimate the specific value of β . In order to determine an initial nighttime estimate for β , the general behavior of net radiation (R_n) and soil heat flux (G) during the nighttime hours (over the period of record) was used to hypothesize about the balance of H and λE (e.g. if nighttime $R_n \sim G$, it was assumed that $H \sim -\lambda E$, so that $\beta \sim -1$). In contrast to the daytime initial β , one constant value of β was estimated for the entire period of record at each location for nighttime data in order to simplify the estimation procedure. In order to assign an initial β value to each time step for data processing, the atmospheric stability information obtained from the observed temperature profile was used to differentiate between daytime and nighttime values of β for each location. R_n and G data (see R_n and G methods below) were used for the subsequent computation of β by energy balance (β_{EB}), along with the initial derivation of H_{LAS} , according to the energy balance method proposed by Green and Hayashi (1998) (Eq. 16). The implementation of this method is discussed in the following ‘Execution of LAS data processing’ section.

$$\beta_{EB} = \frac{H_{LAS}}{R_n - G - H_{LAS}} \quad (16)$$

Net Radiation and Soil Heat Flux Computation

For both study sites, multiple measurement locations of net radiation (R_n) and soil heat flux (G) data were available. At the Timpas site there were two stations, while four stations were available at the AVRC site. The effective R_n and G for each study site were generally determined by averaging the values from the available stations, although the methods for the AVRC site

were less straightforward. A detailed description of the methods used to determine effective R_n and G can be found in Appendix 6. The determination of surface G at each station required computation using data from the soil heat flux plates at soil depth d_{pl} (0.08 m typ.) and from the soil temperature and moisture sensors installed at a depth between the surface and the plates. The procedure given in the HFT3 SHF plate manual (Campbell Scientific, Inc. 2003) was used to compute surface G ; a summary of the method is given in Appendix 4.

EXECUTION OF LAS DATA PROCESSING

The processing of LAS data to obtain H_{LAS} was computed according to the equations discussed in the LAS theory section and the processing tool was realized in Excel Visual Basic for Applications (VBA) code, which facilitated the automation of the iterative procedures necessary for processing. A flow chart of the processing procedure is shown in Figure 4. The basic procedure is summarized here. An initial guess of neutral stability length (L_{mo} ; $\pm 1 \cdot 10^5$ m) was used to compute friction velocity (u_*) and the temperature scale (T_*), which were subsequently used to compute a new value of L_{mo} . This procedure was iterated 10 times, after which H was computed according to Eq. 7. The condition of atmospheric stability was judged using the measured air temperatures from the first (T_1) and third (T_3) levels of the SAT tower. If T_1 was greater than T_3 , conditions were unstable, but stable if T_1 was less than T_3 . The stability condition was subsequently used to determine the solution of H , u_* , T_* , and L_{mo} . Next, a correction of the C_n^2 variable was performed based on Hartogensis (2006) for contributions to the LAS signal from the dissipation range of turbulence. The dissipation range of turbulence represents a zone of energy dissipation or loss, and is bounded by the inner scale eddy size (l_0 , m) (Meijninger 2003). As the LAS must operate in the inertial sub-range where the LAS diameter (D) is much larger

than l_0 (Meijninger 2003), the dissipation range correction is necessary for cases where l_0 is larger relative to D . These conditions can occur during periods with low wind speed. A summary of this method is given in Appendix 3. This procedure was performed iteratively with the

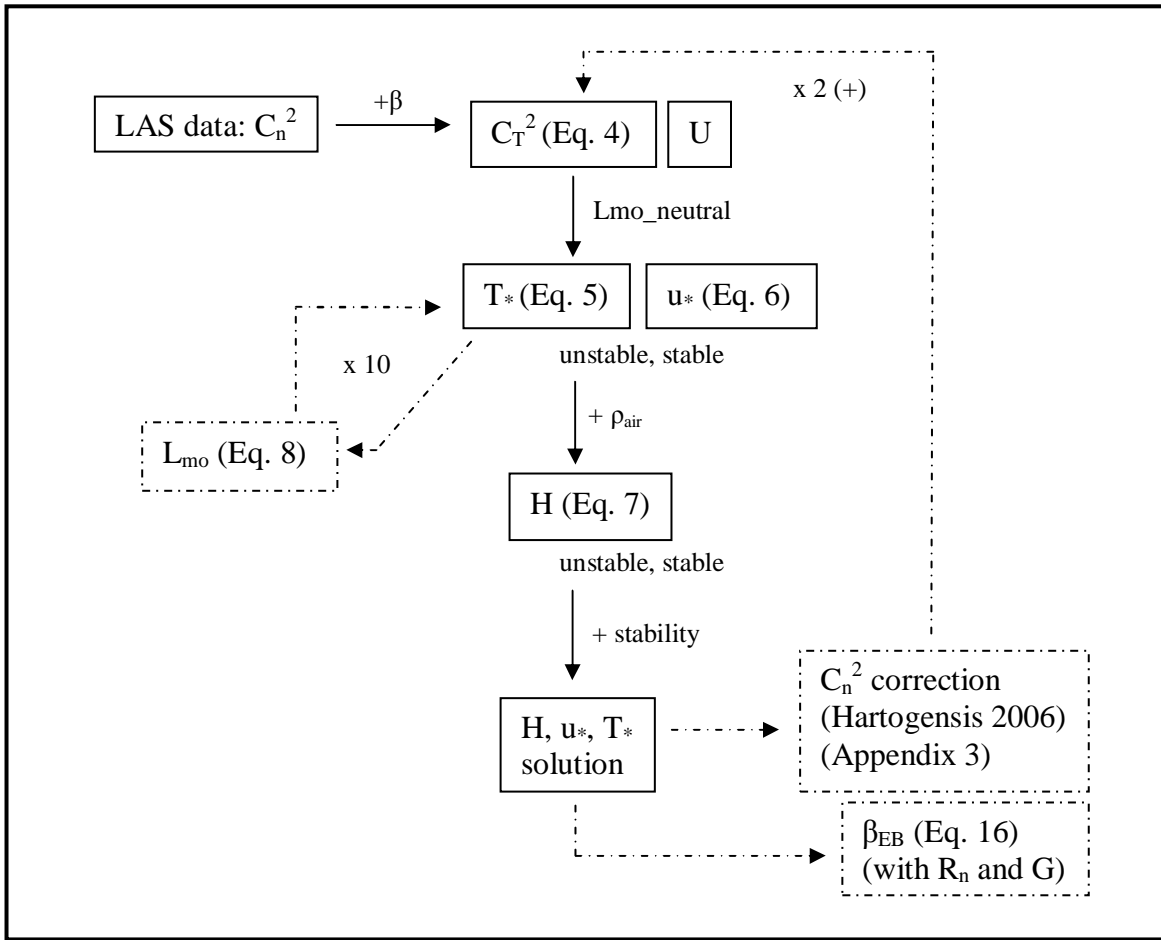


Figure 4. Simplified LAS data processing flowchart. Iterative processes are shown with a dashed line. ‘ β ’ represents Bowen Ratio, ‘U’ represents wind speed, ‘ $L_{mo_neutral}$ ’ represents the initial guess of L_{mo} ($\pm 1 \cdot 10^5$ m), ‘ ρ_{air} ’ represents air density, and ‘ β_{EB} ’ represents the Bowen Ratio computed by energy balance.

computation of H_{LAS} , since it requires input of u^* and L_{mo} , which were taken from the LAS processing output. Simultaneous with the C_n^2 correction, β_{EB} was computed using the initial solution of H_{LAS} (Eq. 16). The corrected C_n^2 and β_{EB} were subsequently entered as input for the

new computation of H_{LAS} ; the procedure was repeated until ΔH_{LAS} between iterations converged to a near zero value, which was typically achieved by the third iteration of H^{12} .

ANALYSIS METHODS

DATA QUALITY CONTROL / FILTERING

Prior to comparison of the LAS data to the EC reference, certain measures were taken to restrict the data from both datasets as a quality control (QC) measure. During processing, the LAS data were removed for signal strength (*Demod*) less than 50 mV to eliminate periods when the LAS units were severely out of alignment (App. 1)¹³. Further, LAS data were automatically removed if C_n^2 was greater than $\{0.18 \times D^{5/3} L_{LAS}^{-8/3} \Lambda^{2/6}\}$, where D is the LAS diameter (m), L_{LAS} is the LAS path length (m), and Λ is the LAS operation wavelength (m) (Ochs and Hill 1982). This filtering was done to avoid signal saturation conditions, which could occur in cases of strong turbulence (Meijninger 2003). Both of these initial filters were recommended by the manufacturer. In addition, low wind speed conditions often led to non-convergence of the LAS stable solution of H (thus also u_* , T_* , and L_{mo}) resulting in a near-zero solution; these data were excluded from the comparison. LAS data were further filtered for all periods with precipitation, small air temperature gradient ($|T_1 - T_3| < 0.2$ °C), and low friction velocity ($u_* < 0.15$ m s⁻¹)¹⁴. The small air temperature gradient filter was applied due to the dependence of the sign of H_{LAS} on the sign of ΔT and because the manufacturer-provided sensor accuracy is 0.2 °C (at 20°C). The low u_* filter was applied to ensure well developed turbulence conditions. The same low u_* filter was applied to the eddy covariance (EC) data. In addition, data where wind direction was from a 60°

¹² The final solution of H_{LAS} was determined generally when the mean period of record ΔH was less than 1 W m⁻² and the count of ΔH values larger than 5 W m⁻² was small.

¹³ This filter was not applied to a subset of LAS-2 data from the Timpas site, after the unit had become almost completely misaligned, in order to test the effect on LAS performance for such a case.

¹⁴ For the AVRC site, the minimum $|T_1 - T_3|$ value was set to 0.1 °C and the minimum u_* to 0.1 m s⁻¹, in order to include more data in the comparison.

window directly behind the EC tower were excluded to avoid conditions where the wind was obstructed before reaching the sensors. For the AVRC site, periods with wind direction from the north (0-90°, 270-360° azimuth) were excluded, since the EC tower had been set up near the northern edge of the field. The stationarity and ITT QC parameters (Foken and Wichura 1996) were at times fairly restrictive, especially for the AVRC site EC data. For this reason, the data were filtered as follows: Data where the horizontal wind and temperature stationarity violation exceeded 30% were excluded. The humidity stationarity test was not used to filter the EC data, which is not of significant concern, since the comparison dealt with H fluxes from the LAS and EC. The ITT tests for horizontal wind speed and temperature were fairly restrictive, and it was thus decided to filter data where any ITT violations exceeded 50% (rather than 30%) in order to permit more data for comparison. The amount (%) of data filtered from the LAS and EC datasets is reported in the ‘LAS to EC comparison’ results section. Finally, the comparison of H_{EC} and H_{LAS} at the AVRC site was *enhanced* with information from a source area model which was resolved for the EC and LAS instruments. Both instruments are subject to the same constraint of horizontal homogeneity, and further similarly capture H based on the assumption of flux unchanging with height in the measurement domain. This requires that the upwind distance of homogeneous surface conditions be substantial enough to create an equilibrium sub-layer deeper than the sensor measurement height (Foken 2008b). For the AVRC data, source area information was modeled using the program developed by Neftel et al. (2008) according to the Kormann and Meixner (2001) algorithm. The Neftel et al. (2008) utility computes the percent contribution to the flux from fields whose coordinates were specified by the user as model input. Since the LAS derived H flux was measured not at a point but on a line, the upwind source area model (derived for point measurement setups) needed to be adapted. For more detail on the source area model

methodology, the reader is referred to Appendix 8. It is notable that the north wind direction filter for the AVRC site acted as a partial source area filter, excluding EC (and LAS) data which came from outside the alfalfa field(s).

COMPARISON METHODS

For the inter-comparison of the LAS data, only the automatic filters (low *Demod*, high (saturation) C_n^2 , near-zero H) were applied to the data, since each of the LAS units was processed with the same data and methods. As an exception, the AVRC LAS data were filtered more strictly for the inter-method comparison. The filters discussed in the above section were applied to the LAS to EC comparison. Data correlation was assessed for comparison of variables including friction velocity (u_* , m s^{-1}) and sensible heat flux (H , W m^{-2}). Statistical performance measures were taken in part from Willmott (1982), including mean absolute error (MAE; Eq. 17) and mean bias error (MBE; Eq. 18);

$$\text{MAE} = \frac{1}{n} \sum_{i=1}^n |P_i - O_i| \quad (17)$$

$$\text{MBE} = \begin{cases} \frac{1}{n} \sum_{i=1}^n (|P_i| - |O_i|), & P_{i..n} \text{ and } O_{i..n} < 0 \\ \frac{1}{n} \sum_{i=1}^n (P_i - O_i), & \text{otherwise} \end{cases}, \quad (18)$$

where P represents the predicted (experimental) value, O represents the observation (reference), and the subscript ‘i’ represents any 30 minute average. These parameters are defined with absolute units (i.e., W m^{-2} , m s^{-1}). Further, the definition of MBE in Eq. 18 is conditional for H (not shown in Willmott 1982), since H can assume negative and positive values. The conditional

definition describes the bias intuitively (magnitude bias) if not rigorously or mathematically correctly. In addition, relative (%) MAE and MBE were computed as shown in Eqs. 19 and 20, respectively.

$$\text{MAE \%} = \frac{1}{n} \sum_{i=1}^n \left| \frac{P_i - O_i}{O_i} \right| \times 100 \quad (19)$$

$$\text{MBE \%} = \frac{1}{n} \sum_{i=1}^n \left(\frac{P_i - O_i}{O_i} \right) \times 100 \quad (20)$$

The definition of relative MBE is appropriate (again, intuitively) for cases when H is negative or positive¹⁵. In some cases the relative MAE and MBE were deemed questionable or erroneous due to influence of extreme values resulting from a very small denominator in Equations 19 and 20. For these cases, $\text{MAE}/|\bar{O}|$ and $\text{MBE}/|\bar{O}|$ parameters were used, where MAE and MBE were in absolute units (W m^{-2} or m s^{-1}), and $|\bar{O}|$ was the mean absolute value of the observation or reference (W m^{-2} or m s^{-1}). This parameter was computed to reveal the approximate relative error, and the use of absolute value of the reference ensured a stable (magnitude) value of the parameter. Linear regression statistics were evaluated in Excel using the linear ‘trendline’ tool, which optimizes the coefficient of determination (r^2) for a given data pair set. Slope of the linear regression (m), y -intercept (b), and the coefficient of determination (r^2) were reported along with the absolute and relative MAE and MBE statistics.

¹⁵ Both absolute and relative MBE parameters will have difficulty representing the correct (intuitive) sign of bias for cases when only one of the data are negative, but the occurrence of these cases should not be common, resulting thus in little impact on the overall mean error statistics.

MONIN-OBUKHOV SIMILARITY THEORY (MOST) CHECK

An alternative method for evaluation of LAS performance which has been proposed in the literature (Hoedjes et al. 2002, Solignac et al. 2009, De Bruin et al. 1993) is to test whether the LAS data has a good fit with the MOST relationship (Eq. 10) used to relate C_T^2 to H . In order to perform this test, a reference value of T^* and of L_{mo} are necessary since the LAS output of the same were derived using the MOST relationship. These reference values were taken from the EC data, where EC T^* (T^*_{EC}) was derived with u^*_{EC} and $L_{mo\ EC}$ according to Eq. 8. The testing was performed for the three LAS units which were set up parallel to one another at the Timpas site, as well as for the LAS-2 unit at the AVRC site. This test has the advantage of providing an evaluation of the LAS (C_T^2) data early in the processing procedure. Multiple (empirical) formulations of the C_T^2 similarity function (f_T) have been presented in the literature, including those of Andreas (1988; A1988), used in this study, as well as those of Hill et al. (1992; H1992), Thiermann and Grassl (1992; TG1992), and De Bruin et al. (1993; DB1993). Moene et al. (2005) show that the f_T curves are generally similar, but that the H1992 and the TG1992 f_T formulations are larger for near-neutral unstable conditions and that the DB1993 stable f_T is a constant value (4.9). Testing of the LAS data for MOST agreement included the evaluation of these various formulations of the $C_T^2 f_T$.

UNCERTAINTY AND LAS MODEL SENSITIVITY

Especially regarding the comparison of LAS to EC H fluxes, it is desirable to know the (random) uncertainty (δ)¹⁶ associated with each instrument/method in order to better evaluate the inter-instrument H flux correlation. For example, if the LAS method for estimating H resulted in a

¹⁶ The value of δ being found using Gaussian error propagation, assuming random and independent uncertainties of model inputs; the value of δ may be approximated as the standard deviation (σ) of the measured value (Taylor).

value of $H_{LAS} \pm \delta H_{LAS}$ (based on the random uncertainties of the method inputs) while the EC-derived H was $H_{EC} \pm \delta H_{EC}$, the correlation of H_{LAS} and H_{EC} would be arguably good if the expected range of H_{LAS} overlapped with the expected range of H_{EC} , even if there was some disagreement between the best estimates of the same. Therefore, some effort was given to understand the uncertainties associated with the LAS method of H estimation. In a study in western Africa, Marx et al. (2008) found approximately 7-8% uncertainty in H_{LAS} using Gaussian error propagation with estimated uncertainties for the LAS inputs. Solignac et al. (2009) found H_{LAS} uncertainty to be dependent on the magnitude of Bowen Ratio (β) in France and reported (also by Gaussian error propagation) approximately 13% uncertainty for more dry (large β) conditions compared to approximately 18% uncertainty for wet (small β) conditions. For the Timpas and AVRC site analyses, normally distributed (random and independent) uncertainties were assumed for the analysis of uncertainty propagation from input to LAS H output. Biases in input data are generally unknown unless a second (reference) measurement is available, which was generally not the case for the Timpas and AVRC data. Further, if the bias of an instrument is known, this should be corrected prior to data processing and would therefore not play a role in the error/uncertainty propagation analysis. Values for uncertainties of LAS data inputs were adopted from Marx et al. (2008) with a few exceptions (Table 2). A detailed description of the LAS algorithm uncertainty propagation can be found in Appendix 9. The LAS uncertainty propagation analysis was performed for a data subset from both (Timpas and AVRC) sites for the different methods of processing. For estimation of the uncertainty associated with EC measurements of H , results of a study by Nemitz et al. (2009) were applied to the Timpas and AVRC site data. The authors of this study compiled flux data from several EC units which had been set up over grassland in northern Germany. The study included variable instrumentation

Table 2. LAS input uncertainty values.

Variable	Estimated Uncertainty (δ)	Source
Air Temperature (T , °K)	0.1 K	Marx et al. (2008)
Relative Humidity (RH , Pa/Pa)	0.02 ($RH < 0.9$), 0.03 ($RH > 0.9$)	Measurement δ (HMP45c, CSI, Logan, UT)
Wind Speed (U , m s ⁻¹)	0.5 %	Marx et al. (2008)
Barometric Pressure (BP , Pa)	100 Pa	Marx et al. (2008)
Bowen Ratio (β , unitless)	¹⁷ 0.25, 0.1 (AVRC 10/08-10/21)	--
C_n^2 (m ^{-2/3})	0.5 %	Marx et al. (2008)
LAS height (z_{LAS} , m)	10 %	--
Wind Speed cup height (z_U , m)	0.03 m	--
Roughness length (z_{om} , m)	10 %	Marx et al. (2008)
Displacement height (d , m)	¹⁸ 10 %	--
Net Radiation (R_n , W m ⁻²)	6 % (Timpas), 10% (AVRC)	¹⁹ Solignac et al. (2009)
Soil Heat Flux (G , W m ⁻²)	10 % (Timpas), 20% (AVRC)	²⁰ Solignac et al. (2009)
Friction Velocity (u_* , m s ⁻¹ ; Sonic Anemometer)	$\delta u_*/u_* = 0.0234 + (0.04233/(u_* + 0.049))$	Nemitz et al. (2009)
Sensible Heat Flux (H_{EC} , W m ⁻²)	$\delta H/H = 0.0767 + (18.87/(H + 20.29))$	Nemitz et al. (2009)

models and different processing algorithms, providing thus an estimate of the uncertainty associated with the EC method in general. The inter-sensor/method standard deviations were adopted to approximate the friction velocity (u_*) and sensible heat flux (H) uncertainty for a case where only one EC unit is available. Nemitz et al. (2009) considered the standard deviations dependent on the magnitude of u_* and H and developed equations to represent variable uncertainty in terms of the variable value (Table 2). In order to further ascertain the sensitivity of the LAS model to individual inputs, a brief examination of the equations involved in LAS data processing was performed to estimate the proportionality of H to each input variable / parameter. For example, with C_n^2 , H is directly proportional to T^* (Eq. 7), T^* is proportional to C_T^2 raised to the half power (Eq. 5), and C_T^2 is directly proportional to C_n^2 (Eq. 4) – thus H is proportional to

¹⁷ (Tab. 2) 0.25 was assumed for initial (guess) Bowen Ratio, and subsequent $\delta\beta$ was determined by propagating the initial δH and estimates for δR_n and δG

¹⁸ (Tab. 2) Uncertainty for zero displacement height assumed the same as for momentum roughness length, since both parameters were estimated as a function of the crop height

¹⁹ (Tab. 2) Value for Timpas δR_n (6%) was taken from Solignac et al. (2009) but AVRC δR_n (10%) was estimated to account for additional spatial variability in R_n at the AVRC

²⁰ (Tab. 2) Use of δG equal to 10% for Timpas was not based on a literature recommendation but the assumption that the Timpas estimated G was more certain than the recommended 15-20% δG range given in the literature.

C_n^2 raised to the half power. The expected sensitivities for some of the variables are reported in [Table 3](#). Occasionally the proportionalities found in this study disagreed with literature assertions; these situations are noted in the table. Sensitivity of H_{LAS} to wind speed (U) or friction velocity (u_*) is shown in [Table 3](#) to be 100%. However, it is known that u_* becomes more or less important depending on the atmospheric stability condition, where H_{LAS} becomes insensitive to u_* during free convective (very unstable) conditions ([Moene et al. 2005](#)).

Table 3. Summary of the LAS model sensitivity analysis.

Variable/Parameter	Proportionality (α) to H	Justification	Comments
C_n^2 ($m^{-2/3}$)	$H \propto (C_n^2)^{1/2}$	$H \propto T^*$; $T^* \propto (C_T^2)^{1/2}$	$H \propto (C_T^2)^{3/4}$ (Martin Veenstra, Kipp and Zonen, personal communication)
L_{LAS} (m)	$H \propto L_{LAS}^{-3/2}$	$H \propto (C_n^2)^{1/2}$	$H \propto L^{-9/4}$ (Moene et al. 2005)
z_{mLAS} (m)	$H \propto z_{mLAS}^{1/3}$	$H \propto T^*$; $T^* \propto z_{mLAS}^{1/3}$	$H \propto z_{mLAS}^{1/3}$ neglects effect of stability; Hartogensis et al. (2003) $H \propto z_{mLAS}$ (free convective conditions), $H \propto z_{mLAS}/2$ (neutral cond.); $z_{mLAS} = z_{LAS} - d$;
U ($m\ s^{-1}$) ^{T3.1}	$H \propto U$	$H \propto u_*$; $u_* \propto U$	

^{T3.1}When computing the LWP friction velocity using two wind speed measurements, H is proportional to $U_2 - U_1$, rather than U .

The sensitivity of H_{LAS} to u_* based on the results from this study will be demonstrated in the results section. Further, sensitivity of H_{LAS} to air temperature (T), barometric pressure (BP), and relative humidity (RH) is not addressed here. The RH has a generally very small effect on the A_T parameter (Eq. 4) and on ρ_{air} (not shown). [Moene et al. 2005](#) suggested that sensitivity of H_{LAS} to T , BP , and RH is not large. In order to know the sensitivity of H_{LAS} to each input parameter (for a range of environmental conditions), a robust sensitivity analysis is recommended, such as a Monte Carlo or other comparable analysis.

RESULTS

INTER-LAS COMPARISON

The inter-LAS comparison results are based on approximately one month of data collected at the dry grassland (Timpas) site during July of 2011. The comparison was performed for three Kipp and Zonen LAS units set up on parallel paths approximately 600 m in length. The setup procedure is discussed in Appendix 1. After one week of operation, the signal strength of both LAS-2 and LAS-3 fell to approximately 25%, deteriorating further to less than 20% over the subsequent two weeks. The units had been aligned and the power adjusted to achieve signal strength of 50% at the time of setup, although the signal strength of LAS-3 had already dropped just below 40% shortly after setup, before data were analyzed. During a site visit on July 21st (2011), the alignment was restored in LAS-2 and -3, although a storm the same afternoon appears to have caused the subsequent (complete) misalignment observed with LAS-2. Units LAS-1 and LAS-3 remained aligned during the remainder of the data collection period. Also on July 21st, an on-site calibration test²¹ was performed for LAS-1 and -2, which showed LAS-1 to be out of calibration, but LAS-2 to be well calibrated. The same calibration test was performed at a later date for LAS-3, showing LAS-3 to be only slightly out of calibration. LAS-2 especially was observed to have a significant amount of apparently out-of-range (positive value) U_{Cn2} data during the midday periods.

The results for the inter-LAS H comparison are shown for three data subsets, based on the above discussion of the alignment issues over the period of record. For the first week when all units were well aligned, there was very little scatter between the H solutions for any of the LAS units

²¹ See Appendix 10.

(Figure 5a, d, and g). However, there was a mean bias (${}^{22}\text{MBE}/|\bar{O}|$) of approximately -11% for LAS-1 to LAS-2 and -9% for LAS-1 to LAS-3. Units LAS-2 and LAS-3 were very well correlated with little bias.

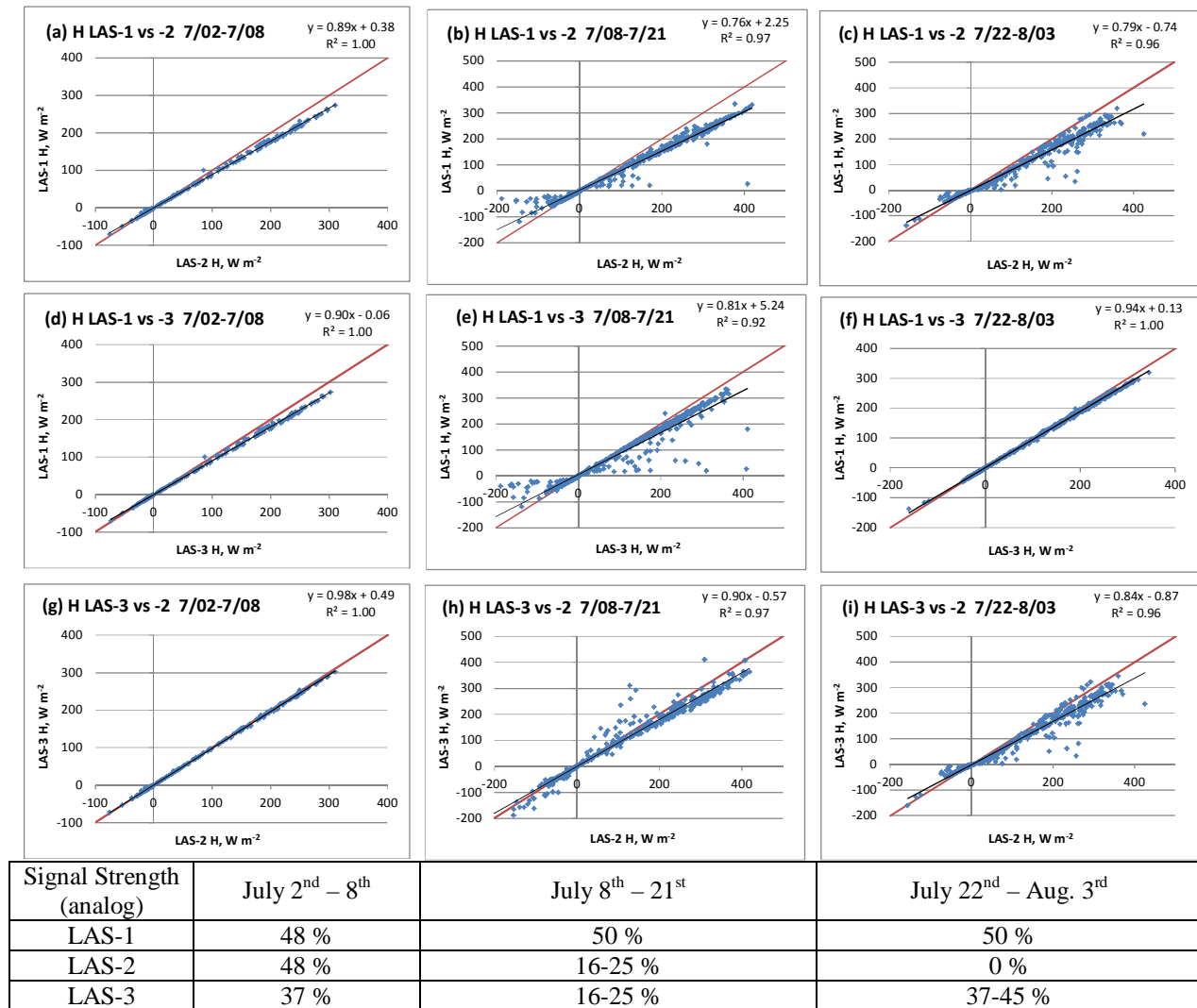


Figure 5. Inter-LAS comparison regression plots for the period July 8th – August 3rd. Comparison of LAS-1 and -2 ($H, W m^{-2}$) for July 2nd – 8th (a), 8th – 21st (b), and 22nd – August 3rd (c); comparison of LAS-1 and -3 for the same periods (d, e, f); comparison of LAS-1 and -2 for the same periods (g, h, i). Timpas H_{LAS} processed using friction velocity (u_*) computed using one wind speed measurement and an estimate for z_{om} . Solid black line represents best-fit linear regression. Solid red line represents 1:1 line.

²² The $|\bar{O}|$ reference data were taken from either LAS-2 or LAS-3 for the inter-LAS comparison. LAS-2 was the reference for any comparison involving LAS-2, and LAS-3 was the reference for comparison between LAS-1 and -3.

Following the decrease in signal strength of LAS-2 and -3 observed on July 8th (the drop was more significant for LAS-2), scatter increased between all LAS units and bias increased between LAS-1 and -2 (Figure 5b, e, and h). The $MBE/|\bar{O}|$ between LAS-1 and -2 increased to 24%, where scatter was especially apparent for late afternoon/nighttime periods associated with larger wind speeds. Further, an $MBE/|\bar{O}|$ of -7% was observed between LAS-3 and -2, making apparent that the slip in alignment did not affect LAS-2 and -3 the same. It is notable that the trend between LAS-1 and -3 H did not seem to change after the July 8th slip in alignment, although scatter did increase (Figure 5d, e).

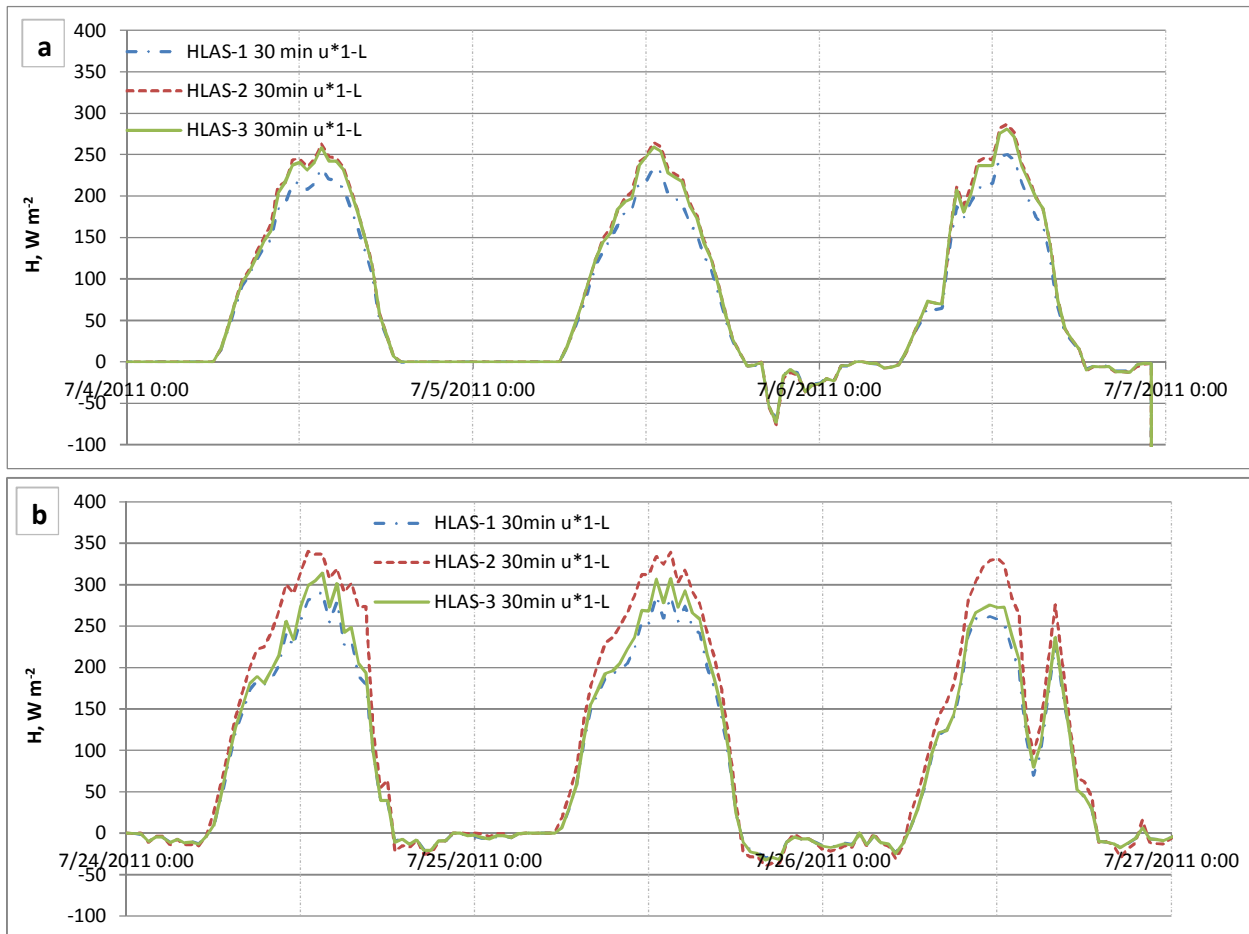


Figure 6. Time series plots of H for LAS-1, -2, and -3 for data subsets from July 4th – 6th (a; good LAS alignment) and July 24th – 26th (b; poor alignment LAS-2, good alignment LAS-1 and -3). Timpas H_{LAS} processed using friction velocity (u_*) computed using one wind speed measurement and an estimate for z_{om} . Fig. 6a represents data shown in Figs. 5a, d, and g. Fig. 6b represents data shown in Figs. 5c, f, and i.

After the complete misalignment of LAS-2 late July 21st along with the improved alignment of LAS-3, the level of scatter and bias between LAS-1 and -2 remained similar to the prior subset, but the scatter and bias between LAS-1 and -3 were reduced (Figure 5c, f, and i). The $MBE/|\bar{O}|$ between LAS-1 and -3 was reduced from -18% to -6% (even less than the first subset value of -9%). Despite the signal strength of LAS-2 being near zero, the general diurnal pattern in LAS-2 H was similar to that of LAS-1 and -3 (Figure 6b). Furthermore, the deviation between LAS-1 and -2 H was not larger than for the prior period when LAS-2 had approximately 20% signal strength. The approximate signal strength pattern for each LAS is tabulated and shown at the bottom of Figure 5.

INTER-METHOD COMPARISON

The inter-method comparison results represent the comparison of LAS output for testing of different processing methods, especially associated with the method of calculating friction velocity (u_* , $m\ s^{-1}$). The inter-method comparison includes results from the dry grassland (Timpas) and AVRC sites. For the Timpas site, the comparison included data from all LAS units, although a more rigorous analysis was performed for LAS-1, since this LAS unit remained at the Timpas site for the entire summer data collection period. For the AVRC site, an additional test was performed to test a different humidity correction factor (HCF) to compute C_T^2 from the LAS C_n^2 output signal. This is because the standard HCF assumes temperature and humidity are well correlated ($r_{Tq} = 1$)⁶. The test was performed using the Wesely (1976) HCF assuming r_{Tq} equal to zero and the comparison of the resulting H was included in the analysis. Friction velocity (u_*) was computed using the two variations of the logarithmic wind profile (LWP) discussed in the methodology section. First, the LWP was defined with level one being at height ($z_{om} + d$), where

wind speed is theoretically assumed equal to zero – for this model, an estimate of the roughness length (z_{om}) and measurement of wind speed at one level (height) were necessary (u_{*1-L}). Second, the standard definition of the LWP was used, where wind speed measurements at two levels were required (u_{*2-L}). For an additional method, u_* was taken directly from the EC sonic anemometer (u_{*EC}). Finally, LAS data were processed using both u_* and the Obukhov stability length (L_{mo} , m) derived from the sonic anemometer. With this method, input of L_{mo} allowed direct (analytical) computation of the temperature scale (T_* , °K) and subsequently H , requiring no iteration for stability ($u_*+L_{mo} EC$).

H COMPARISON (TIMPAS)

Comparison of H computed with u_{*1-L} and u_{*2-L} was consistent for all LAS units during the LAS inter-comparison study period at the Timpas site (July 8th – August 3rd). Scatter was observed between H solutions for small negative H and also increased with increasing positive H (Figure 7a-c). In addition, $MBE/|\bar{O}|$ of approximately -15% was observed where $H_{u_{*1-L}}$ was less than $H_{u_{*2-L}}$.

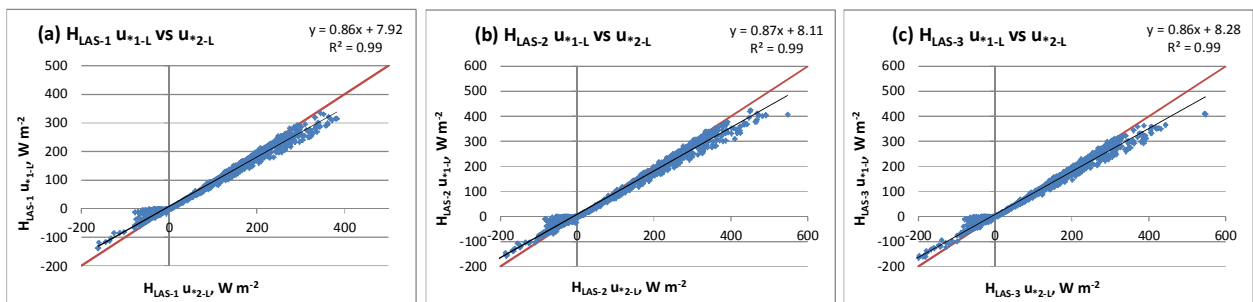


Figure 7. LAS Inter-method H comparison regression plots, u_{*1-L} versus u_{*2-L} for LAS-1 (a), LAS-2 (b), and LAS-3 (c); July 8th – August 3rd. Solid black line represents best-fit linear regression. Solid red line represents 1:1 line. Timpas site.

The same comparison for only LAS-1 (Timpas site) for the entire available data record (July 8th – Oct. 4th) showed consistent results for the regression parameters (Figure 8) and the statistical

deviation parameters ($MBE/|\bar{O}| = -16\%$; $H_{u^*1-L} < H_{u^*2-L}$). After filtering data to show only conditions where wind speed was larger than 2 m s^{-1} and H was positive, the $MBE/|\bar{O}|$ was reduced to -9% and the regression slope was improved (Figure 9). Further, the negative H data were isolated to discern the reason for the small negative H scatter. The negative H was shown only for periods with wind speed greater than 4 m s^{-1} . From Figure 10 it is apparent that the small negative H scatter was eliminated at larger wind speeds, although the relative dependence of H on u^* was apparently larger for negative (stable) H considering the $MBE/|\bar{O}|$ was -20% , where $|H_{u^*1-L}|$ was less than $|H_{u^*2-L}|$.

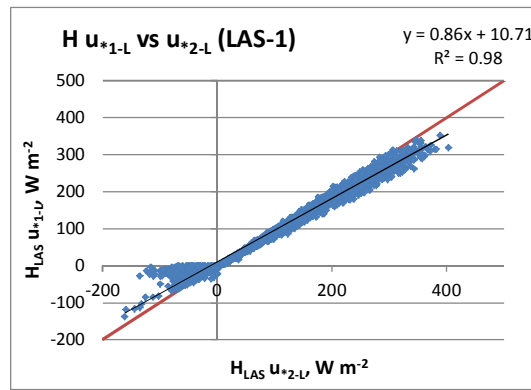


Figure 8. LAS Inter-method H comparison regression plot, u_{*1-L} versus u_{*2-L} for LAS-1; July 8th – Oct. 4th. Solid black line represents best-fit linear regression. Solid red line represents 1:1 line. Timpas site.

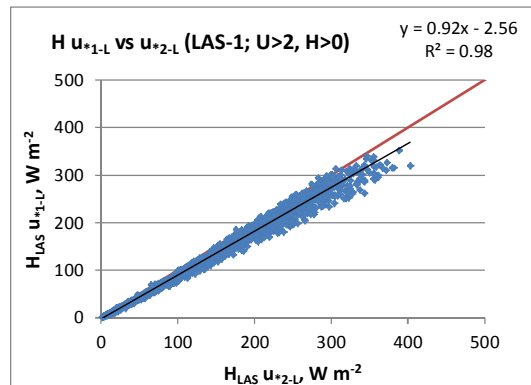


Figure 9. Same as Fig. 8, for wind speed greater than 2 m s^{-1} and H greater than zero.

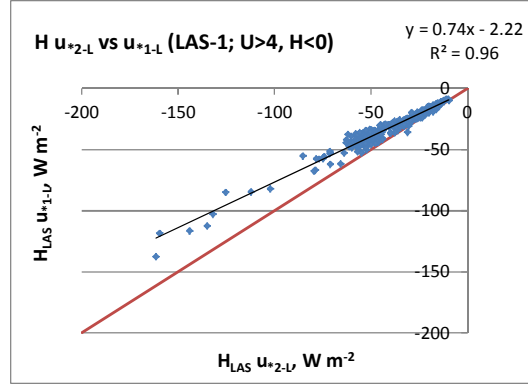


Figure 10. Same as Fig. 8, for wind speed greater than 4 m s^{-1} and H less than zero.

The comparison of the additional methods requiring sonic anemometer input of u^* was performed for the available EC tower period of record at the Timpas site (July 9th – August 26th; LAS-1 only). For this comparison, the H_{LAS} derived from the u^*+L_{mo} EC method was used as a reference, rather than showing the comparison of all possible combinations of methods. The u^*_{1-L} method was shown to underestimate H relative to the u^*+L_{mo} EC method ($\text{MBE}/|\bar{O}| = -5\%$), whereas the u^*_{2-L} method was shown to overestimate H ($\text{MBE}/|\bar{O}| = 9\%$) relative to the u^*+L_{mo} EC method. Finally, u^*_{EC} method H was not significantly different from the u^*+L_{mo} EC method H , where $\text{MBE}/|\bar{O}|$ was less than $+1\%$ and $\text{MAE}/|\bar{O}|$ was only 2% . The scatter in H relative to the reference (u^*+L_{mo} EC) method was largest for the u^*_{2-L} method (Figure 11 a-c). The results showed that the u^*_{1-L} and u^*_{2-L} methods were not similar for the derivation of H , which suggested some bias in the z_{om} estimate. The LAS-1 data were reprocessed using a refined z_{om} estimate, along with a corrected z_{LAS} and calibration-corrected U_{Cn2} signal²³. The resulting modified inputs were larger, also corresponding to a larger H_{LAS} . For the LAS-1 record period (July 2nd – Oct. 4th), the original u^*_{1-L} H was on average less than the modified u^*_{1-L} H by 16% ($\text{MBE}/|\bar{O}|$). The

²³ The justification for these modifications to the LAS input data can be found in Appendix 7. The value of z_{LAS} was adjusted considering the topography along the LAS path. The U_{Cn2} signal was adjusted approximately to account for the observed calibration drift.

relationship between original and modified was consistent over the period of record with little scatter (Figure 12).

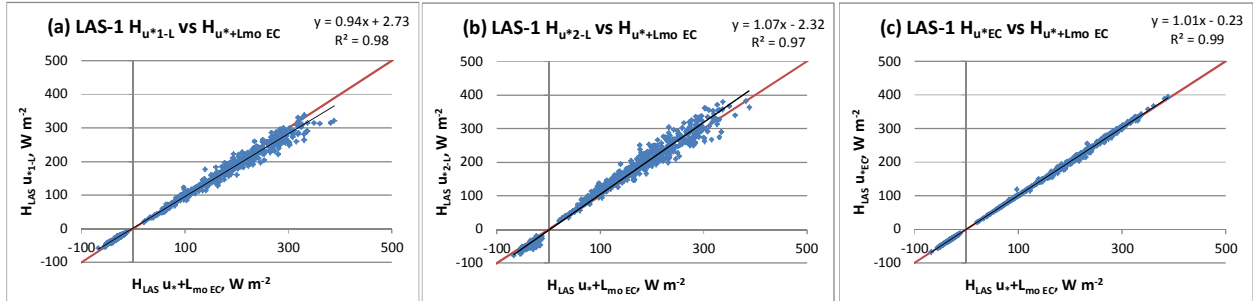


Figure 11. LAS Inter-method H comparison regression plots for LAS-1, July 9th – August 26th; u_{*1-L} (a), u_{*2-L} (b), and u_{*EC} (c) versus $u_{*+Lmo EC}$. Solid black line represents best-fit linear regression. Solid red line represents 1:1 line. Timpas site.

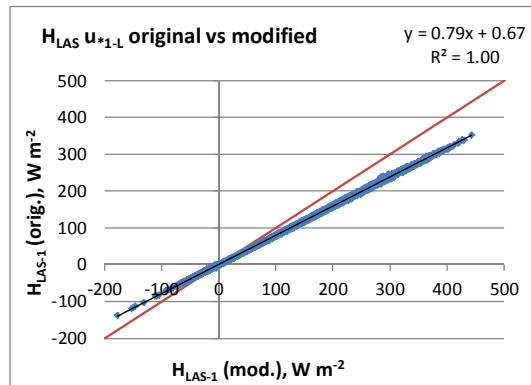


Figure 12. LAS Inter-method H comparison regression plot for LAS-1 (u_{*1-L}), July 2nd – Oct. 4th; original input versus modified input (z_{LAS} , z_{om} , and U_{Cn2} offset). Solid black line represents best-fit linear regression. Solid red line represents 1:1 line. Timpas site.

FRICITION VELOCITY (u_*) COMPARISON (TIMPAS)

The comparison of u_* allows more insight into the above patterns observed for H . For the period from July 9th – August 26th, LAS-1 u_* data were compared between the different LWP methods and the EC measurement, excluding data where u_* was less than 0.15 m s^{-1} . The original ($z_{om} = 0.014 \text{ m}$) u_{*1-L} was found to be on average slightly less than u_{*EC} (MBE = -5%), whereas u_{*2-L}

had a positive bias of 19% (MBE) with respect to u_{*EC} . The modified ($z_{om} = 0.03$ m)²⁴ u_{*1-L} was on average larger than u_{*EC} (MBE 12%). Subsequent comparison of u_{*1-L} to u_{*2-L} (original and modified) showed much better agreement between u_{*1-L} and u_{*2-L} for the modified ($z_{om} = 0.03$ m) case (Figure 13a, b). This confirmed the suspected bias in the original z_{om} estimate. Deviation between u_{*1-L} and u_{*2-L} was especially apparent for low values of u_* ($u_{*1-L} < 0.3$ m s⁻¹) even after filtering for u_* values less than 0.15 m s⁻¹.

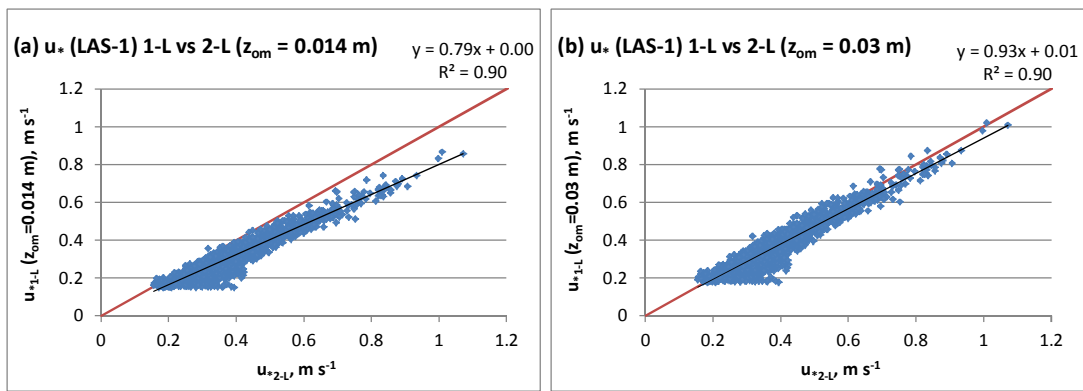


Figure 13. LAS inter-method u_* comparison regression plots, u_{*1-L} versus u_{*2-L} (LAS-1); z_{om} equal to 0.014 m (a) and 0.03 m (b); July 9th – August 26th; original input versus modified input (z_{LAS} , z_{om} , and U_{Cn2} offset). Solid black line represents best-fit linear regression. Solid red line represents 1:1 line. Timpas site.

The error might have been in u_{*2-L} , since the deviation was also apparent when comparing u_{*2-L} and u_{*EC} (Figure 14b). Comparison of u_* for wind speed partitions revealed that the correlation between u_{*EC} and u_{*LWP} improved in all cases with increased wind speed. Deviation between u_{*LWP} and u_{*EC} was significant for wind speed less than 2 m s⁻¹, demonstrated by regression slopes far from 1.0 and very low r^2 values (Figure 14). Despite better correlation for higher wind speed, there was apparent bias for u_{*LWP} to overestimate u_{*EC} (Figure 14b-c). Overall, correlation

²⁴ Although reprocessing the LAS-1 data included modification of z_{LAS} and U_{Cn2} in addition to z_{om} , the effect of z_{LAS} and U_{Cn2} on u_* is little (only through L_{mo}), and it was considered reasonable to include the modified LAS-1 u_{*1-L} in the comparison.

between different u_* solutions was worse than that between H_{LAS} computed by different u_* methods, demonstrating that H_{LAS} was not extremely sensitive to u_* .

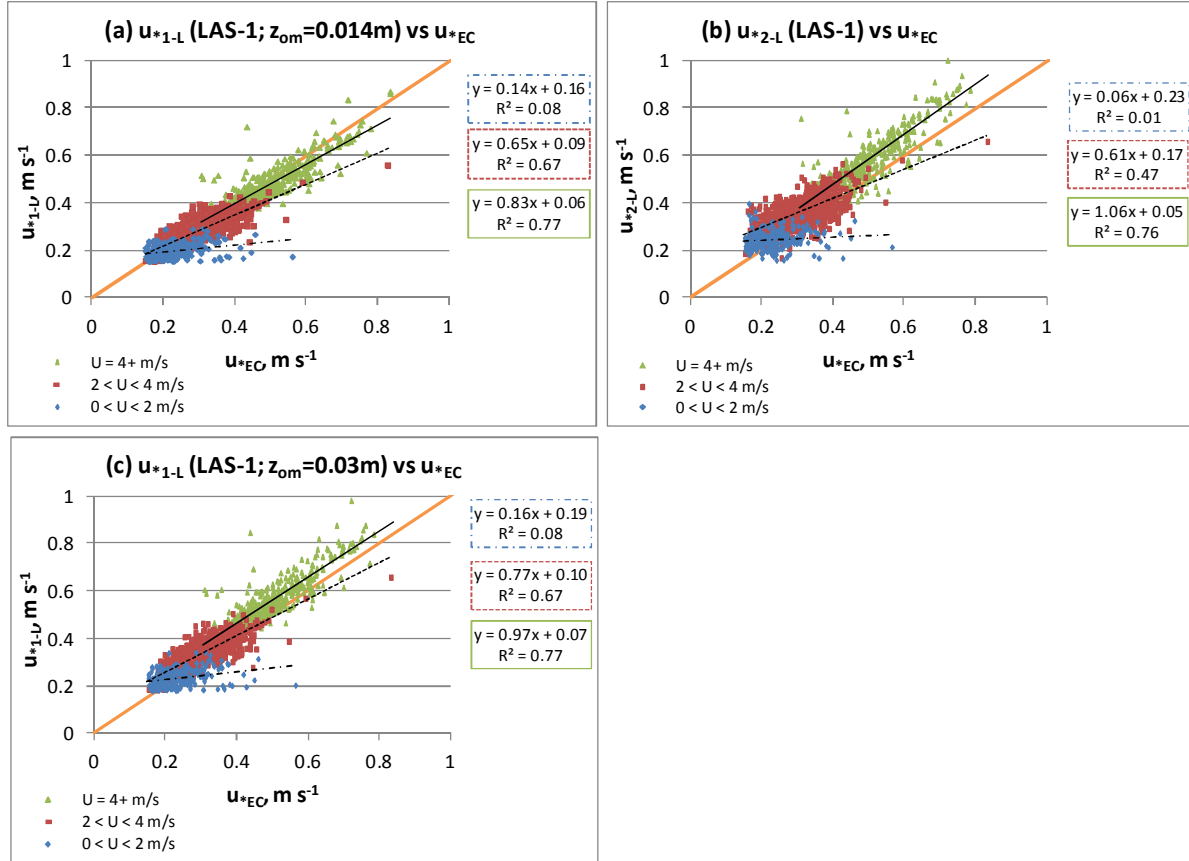


Figure 14. LAS inter-method u_* comparison regression plots, u_{*LWP} (LAS-1) versus u_{*EC} ; u_{*1-L} ($z_{om} = 0.014 \text{ m}$) (a), u_{*2-L} (b), and u_{*1-L} ($z_{om} = 0.03 \text{ m}$) (c); July 9th – August 26th; Solid or dashed black lines represent best-fit linear regression. Solid orange line represents 1:1 line. Blue diamond represents wind speed less than 2 m s^{-1} , red square between $2 - 4 \text{ m s}^{-1}$, green triangle greater than 4 m s^{-1} . Timpas site.

H COMPARISON (AVRC)

The inter-method comparison for the AVRC site included seven methods as follows: u_{*1-L} with the assumption of $r_{Tq} = 1.0$ (HCF1 method), u_{*1-L} with assumption of $r_{Tq} = 0$ (HCF2 method), u_{*2-L} using SAT tower levels 1 and 3 (1m/3m method), u_{*2-L} using levels 2 and 4 (2m/4m method), u_{*EC} method, $u_{*+L_{mo} EC}$ method, and finally, u_{*1-L} with new estimation of the effective z_{LAS}

(modified HCF1 method). Although results at the Timpas site for H u^*_{2-L} were similar for different arm-pairs (not shown), the two methods were tested for the AVRC site to assess the similarity for a limited fetch case. For the inter-method comparison, the reference H was from the u^*_{EC} method unless otherwise noted. The regression plots and corresponding statistics are shown in Figure 15a-f for the different H_{LAS} methods for the period from August 28th – Oct. 21st when LAS and EC data were available (since u^*_{EC} was needed for LAS processing).

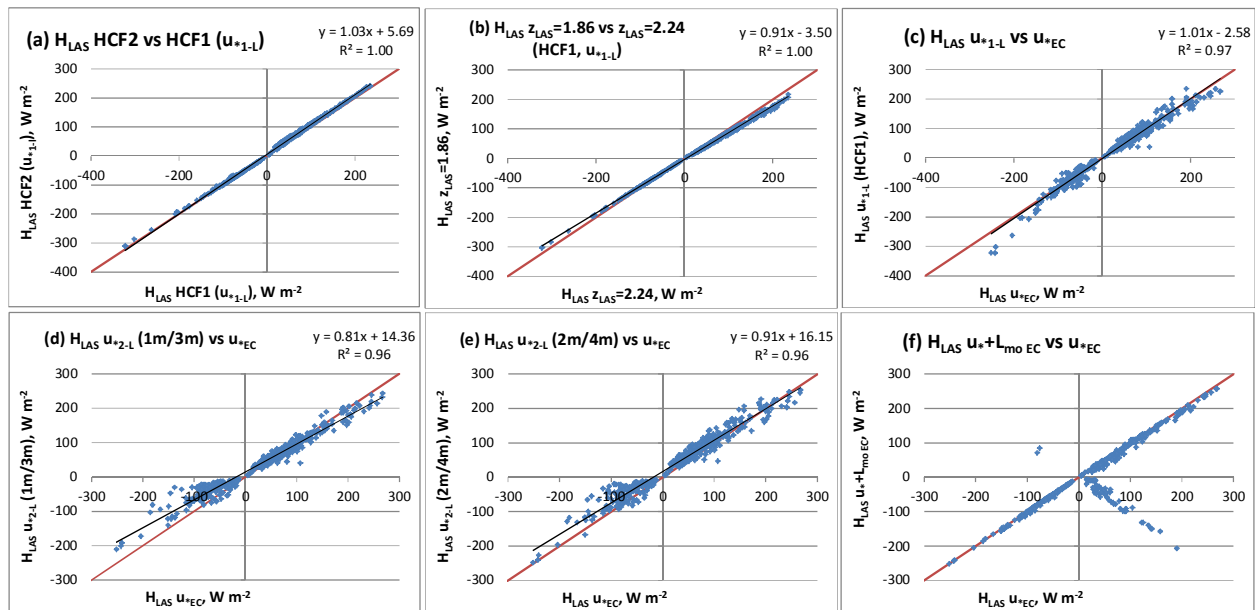


Figure 15. LAS Inter-method H comparison regression plots for LAS-2 (AVRC site), August 28th – Oct. 21st; humidity correction factor (HCF) 2 versus HCF1 (u^*_{1-L}) (a), modified z_{LAS} (1.86 m) versus original z_{LAS} (2.24 m) (b), u^*_{1-L} (HCF1) (c), u^*_{2-L} (1m/3m) (d), u^*_{2-L} (2m/4m) (e), and $u^*_{+Lmo EC}$ (f) versus u^*_{EC} . Solid black line represents best-fit linear regression. Solid red line represents 1:1 line.

Data were filtered according to the LAS criteria indicated in the methodology ‘Data quality control / filtering’ section and filtered to exclude periods with wind direction from the north (0-90°, 270-360° azimuth). The effect of assuming r_{Tq} equal to zero (HCF2 method) was to increase H by approximately 6% with respect to the original HCF1 method (MBE/ \bar{O}); Figure 15a), although it is apparent from Figure 15a that the overestimation was restricted to positive H

periods and for negative H , the HCF2 method underestimated the magnitude of H with respect to the HCF1 method. The 1m/3m method H_{LAS} was less than the u_{*EC} H_{LAS} by approximately 15% on average, whereas the 2m/4m method H_{LAS} was only less than the u_{*EC} H_{LAS} by 3% on average, showing apparent difference between the two u_{*2-L} methods. Further, both u_{*2-L} methods showed more bias and scatter for negative than for positive H (Figure 15d, e). The $u_{*+L_{mo}}$ EC method H_{LAS} was very similar to the u_{*EC} method reference except for periods when the stability condition was different between LAS and EC²⁵ (Figure 15f). Due to the obvious discrepancy for this case, represented by the points approximately perpendicular to the one-to-one line, mean period statistics were not computed for the $u_{*+L_{mo}}$ EC method. Despite some deviation for larger (positive and negative) H , the HCF1 method H_{LAS} was very well correlated with the u_{*EC} method H_{LAS} ($MBE/|\bar{O}| = 2\%$; Figure 15c). Finally, the modified HCF1 method H_{LAS} was shown to have a bias of -10% with respect to the original HCF1 method ($MBE/|\bar{O}|$; Figure 15b). Note²⁶ that the modified estimate of z_{LAS} equal to 1.86 m was 17% less than the original estimate of 2.24 m.

FRICITION VELOCITY (u_*) COMPARISON (AVRC)

The inter-method comparison of u_* was performed for four methods including the u_{*1-L} method, both u_{*2-L} methods, and u_{*EC} ; the reference for comparison was u_{*EC} . Data were filtered in the same manner as for the H inter-method comparison (above). Albeit some scatter and overestimation bias for larger u_* , u_{*1-L} compared very closely to u_{*EC} with mean bias of only 2% ($MBE/|\bar{O}|$; Figure 16a). The $u_{*1m/3m}$ showed a tendency to underestimate u_{*EC} for larger u_* (Figure 16b) and had a mean bias of -11% with respect to u_{*EC} ($MBE/|\bar{O}|$). The solution of $u_{*2m/4m}$, on the

²⁵ Recall the method for determining stability for the LAS processing via the SAT tower temperature profile. The stability from this method and from the EC was more often in disagreement at the AVRC site compared to the Timpas site.

²⁶ The justification for modification of z_{LAS} is the same as for Timpas; see Appendix 2.

other hand, was on average 4% larger than u^*_{EC} ($MBE/|\bar{O}|$). Nonetheless, the scatter between $u^*_{2m/4m}$ and u^*_{EC} was significant ($r^2 = 0.57$) and many data points were also observed below the 1:1 line (Figure 16c). The relationship between $u^*_{2m/4m}$ and $u^*_{1m/3m}$ is shown in Figure 16d, revealing good correlation between both u^*_{2-L} methods, despite the bias for $u^*_{2m/4m}$ to be greater than $u^*_{1m/3m}$. Further, it seems apparent from Figure 16b-c that there was some non-linearity between u^*_{2-L} and u^*_{EC} , showing an apparent minimum u^* threshold for u^*_{2-L} at approximately 0.2 m s^{-1} . This suggests that the relationship between u^*_{2-L} and u^*_{EC} changed depending on the value of u^* . It could be argued that this pattern was observed also with the Timpas data for u^*_{2-L} versus u^*_{EC} (Figure 14b).

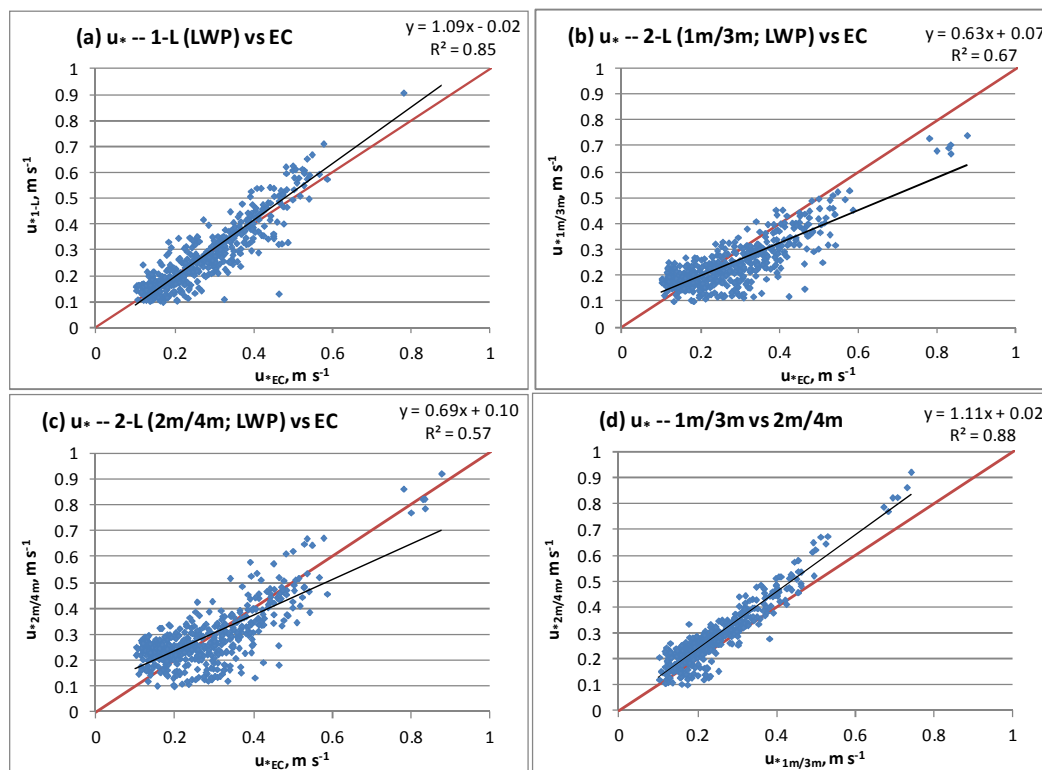


Figure 16. LAS Inter-method u^* comparison regression plots for LAS-2 (AVRC site), August 28th – Oct. 21st; u^*_{1-L} (HCF1) (a), u^*_{2-L} (1m/3m) (b), and u^*_{2-L} (2m/4m) (c) versus u^*_{EC} , and u^*_{2-L} 2m/4m versus 1m/3m (d). Solid black line represents best-fit linear regression. Solid red line represents 1:1 line.

LAS TO EC COMPARISON

The primary basis of the LAS performance evaluation is the comparison of H_{LAS} to H_{EC} . For the Timpas site, this comparison was performed for all three LAS units, and for the different LAS processing methods. For the AVRC site, the comparison included the various LAS processing methods. LAS and EC H data were filtered as discussed in the methodology section. The data filtering measures for the Timpas site resulted in removal of approximately 61% of the EC data, whereas removal of LAS data was dependent on the processing method, showing approximately 50% removal of the LAS u_{*1-L} data, 31% removal of u_{*2-L} data, and 44% removal of u_{*EC} data. For the AVRC site, filtering measures resulted in removal of between approximately 43-58% of the LAS data and approximately 87% of the EC data, where the EC data filtering included the restriction of wind direction from the north (0-90°, 270-360° azimuth). This additional filter was imposed with consideration of the flux source areas for both instruments. Furthermore, the AVRC LAS to EC comparison was restricted to positive H (unstable condition) data only. Although the loss of data was substantial, it was observed that LAS data were removed mostly from evening until morning, such that midday data were generally retained. The LAS to EC comparison for the Timpas site was performed first for the period of record common for all three LAS units and the EC unit (July 9th – August 2nd). Subsequently, LAS-1 data were compared to EC data from July 9th – August 26th. For the AVRC site, data were compared for the common LAS and EC record period (August 28th – October 21st).

TIMPAS

The comparison of LAS-1, -2, and -3 H to H_{EC} for the original u_{*1-L} , u_{*2-L} , and u_{*EC} methods is shown in [Figure 17a-i](#) for July 9th – August 2nd.

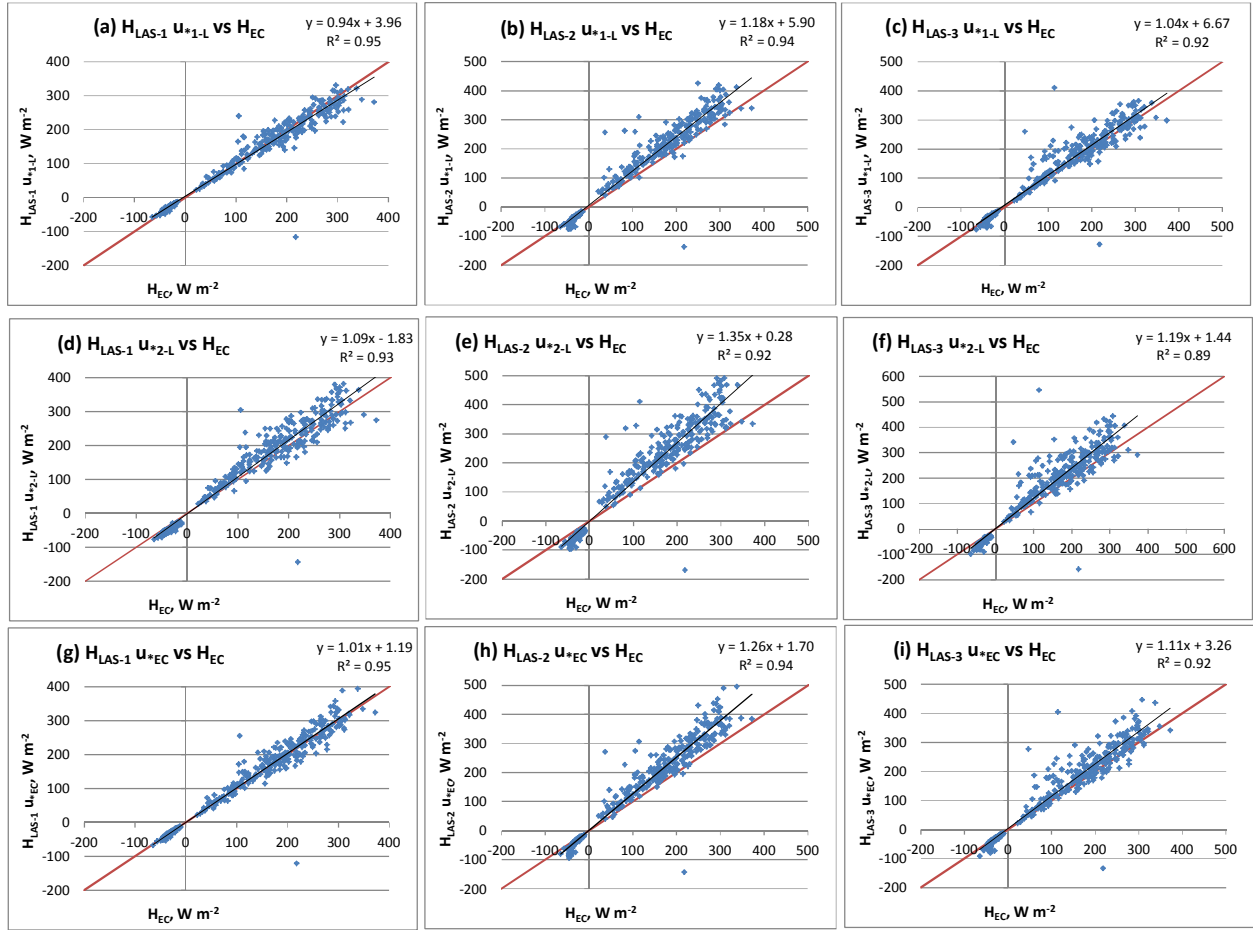


Figure 17. LAS to EC H comparison for LAS-1, -2, and -3 (Timpas site) from July 9th – August 2nd; u_{*1-L} method LAS-1 (a), LAS-2 (b), and LAS-3 (c) versus H_{EC} ; u_{*2-L} method LAS-1 (d), LAS-2 (e), and LAS-3 (f) versus H_{EC} ; u_{*EC} method LAS-1 (g), LAS-2 (h), and LAS-3 (i) versus H_{EC} . Solid black line represents best-fit linear regression. Solid red line represents 1:1 line.

The derived slope uncertainties for H_{LAS} (App. 9) and the given uncertainty formula for H_{EC} (Table 2) were used to compute mean period values of δH ($W m^{-2}$). These values were compared with the mean absolute deviations (MAE, $W m^{-2}$) between LAS and EC for each LAS and each processing method in Figure 18a-c. The H_{LAS} u_{*1-L} uncertainty was less than that of the u_{*2-L} and u_{*EC} methods. Further, H_{EC} uncertainty was generally larger than H_{LAS} uncertainty, especially in comparison to the LAS u_{*1-L} method. If, hypothetically, the LAS-to-EC MAE magnitude is similar to the sum of the mean δH values for H_{LAS} and H_{EC} , there is potential (within the realm of

random method uncertainties) for overlap of the H_{LAS} and H_{EC} solutions. Although LAS-2 MAE did not exceed the sum of mean δH_{LAS} and δH_{EC} except for the u_{*2-L} case, it was in all cases higher than mean δH_{EC} . The LAS-1 MAE, on the other hand, did not approach the sum of mean δH_{LAS} and δH_{EC} for any case. The LAS-3 MAE only approached the sum of mean δH_{LAS} and δH_{EC} for the u_{*2-L} method. This suggests that LAS-2 H was significantly different from H_{EC} , and that for each LAS, $H_{u_{*2-L}}$ was significantly different from H_{EC} .

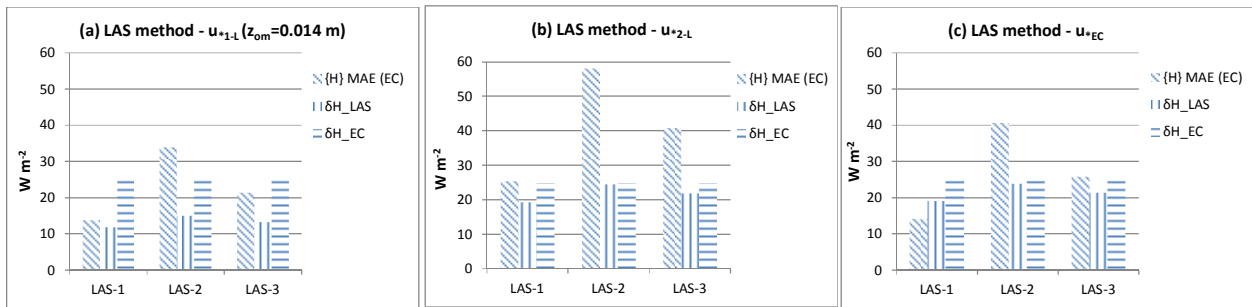


Figure 18. Plots showing period of record (July 9th – August 2nd) mean absolute error (MAE, $W m^{-2}$) between LAS and EC (Timpas site) along with mean uncertainty (δ , $W m^{-2}$) for H_{LAS} and H_{EC} , for LAS-1, -2, and -3; u_{*1-L} method (a), u_{*2-L} method (b), and u_{*EC} method (c). Diagonal line texture represents MAE, vertical line texture represents δH_{LAS} , and horizontal line texture represents δH_{EC} .

The Timpas LAS evaluation was further developed for LAS-1 considering data through August 26th. Further, two additional processing methods were considered: explicit H_{LAS} evaluation using u_* and L_{mo} from the EC unit, and the modified input u_{*1-L} case. The results for each LAS-1 processing method comparison of H_{LAS} to H_{EC} are shown in Table 4 and Figure 19a-e. The regression and deviation statistics for the original u_{*1-L} , u_{*2-L} , and u_{*EC} methods were similar to the July 9th – August 2nd period, implying a consistent LAS-1 to EC relationship over time. The $u_{*+L_{mo}}$ EC method H_{LAS} showed only slightly better correlation with H_{EC} than that from the u_{*EC} method (comp. $MBE/|\bar{O}|$ 3% to 4%; Figure 19c, d). Thus the $u_{*+L_{mo}}$ EC method H_{LAS} showed the overall best correlation to H_{EC} . Comparison of the modified input (u_{*1-L}) H_{LAS} to H_{EC} revealed

significant bias for H_{LAS} greater than H_{EC} ($MBE/|\bar{O}| = 24\%$; Figure 19e). This disagreement suggests inappropriate modifications to the LAS inputs and/or (inherent) LAS bias to overestimate H .

Table 4. Deviation statistics for LAS-1 to EC H comparison (Timpas site) for the July 9th – August 26th period of record (n = 597).

H_{LAS} method	MAE, $W m^{-2}$	MBE, $W m^{-2}$	MAE/ $ \bar{O} $, %	MBE/ $ \bar{O} $, %
u_{*1-L}	13.8	-2.8	10	-2
u_{*2-L}	24.8	17.5	18	12
u_{*EC}	15.0	5.5	11	4
$u_{*+L_{mo}EC}$	12.6	4.8	9	3
u_{*1-L} (modified)	35.8	34.0	25	24

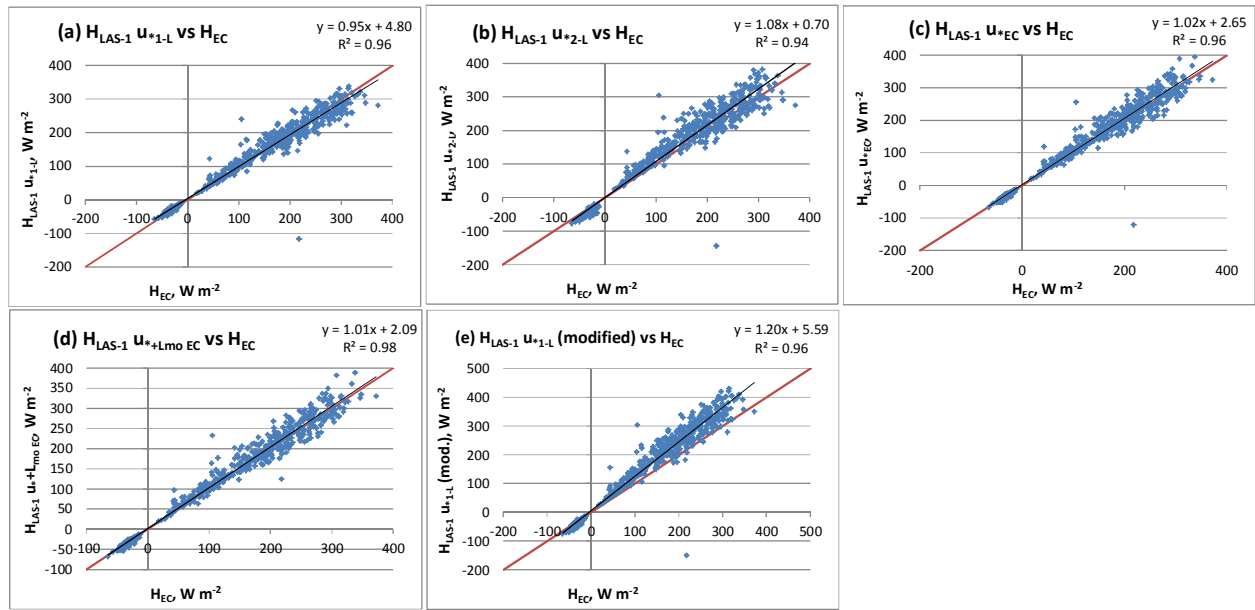


Figure 19. LAS to EC H comparison for LAS-1 only (Timpas site) from July 9th – August 26th; u_{*1-L} method (a), u_{*2-L} method (b), u_{*EC} method (c), $u_{*+L_{mo}EC}$ method (d), and u_{*1-L} method with modified inputs (e) versus H_{EC} . Solid black line represents best-fit linear regression. Solid red line represents 1:1 line.

AVRC

The comparison of H_{LAS} to H_{EC} was performed using the same (n = 7) methods as for the inter-method comparison. Because of the filtering procedures, and limiting the data to positive H

(unstable conditions), only 120 points (30 minute average) were available for comparison. The overall relationship between LAS and EC H did not vary significantly between methods, where H_{LAS} was greater than H_{EC} . The regression plots of H_{LAS} versus H_{EC} with statistics are shown in Figure 20a-g and tabulated comparison statistics are shown in Table 5. Both H_{LAS} methods incorporating u^*_{EC} (with and without $L_{mo\ EC}$) showed the least scatter ($r^2 > 0.9$) and the smallest y-intercept value with respect to H_{EC} , where the $u^*+L_{mo\ EC}$ method was slightly better than the u^*_{EC} method (Figure 20f, g). Nonetheless, these methods also showed more apparent bias to overestimate H_{EC} for larger H . The HCF2 (u^*_{1-L}) and the u^*_{2-L} (2m/4m) methods had similar performance to one another with respect to H_{EC} (Figure 20c, e; Table 5); these results apparently reflect the lack of reduction of C_T^2 with the alternate HCF and the tendency for u^*_{2-L} (2m/4m) to be larger than u^*_{2-L} (1m/3m), both of which would result in a larger H . Subsequently the original HCF1 (u^*_{1-L}) and the u^*_{2-L} (1m/3m) methods showed similar and slightly better correlation with H_{EC} (Figure 20a, d; Table 5). Finally, the modified HCF1 (u^*_{1-L} ; $z_{LAS} = 1.86$ m) method showed the best correlation with respect to H_{EC} with a mean bias of only 4% ($MBE/|\bar{O}|$), despite a similar tendency to overestimate H_{EC} for low H (Figure 20b).

Table 5. Deviation statistics for LAS-2 to EC H comparison (AVRC site) for the August 28th – Oct. 21st period of record. HCF1 unless otherwise noted; $z_{LAS} = 2.24$ m unless otherwise noted (n = 120).

H_{LAS} method	MAE, $W\ m^{-2}$	MBE, $W\ m^{-2}$	MAE/ $ \bar{O} $, %	MBE/ $ \bar{O} $, %
u^*_{1-L}	20.9	16.6	24	19
u^*_{1-L} ($z_{LAS} = 1.86$ m)	15.8	3.2	18	4
u^*_{1-L} (HCF2)	26.9	24.8	31	29
u^*_{2-L} (1m/3m)	20.7	15.8	24	18
u^*_{2-L} (2m/4m)	27.9	25.5	33	30
u^*_{EC}	24.6	23.1	29	27
$u^*+L_{mo\ EC}$	19.9	18.6	23	22

Random propagated uncertainty in H was computed in the same manner as for the Timpas site, but only for three of the H_{LAS} methods (u^*_{1-L} , u^*_{2-L} (1m/3m), and u^*_{EC}).

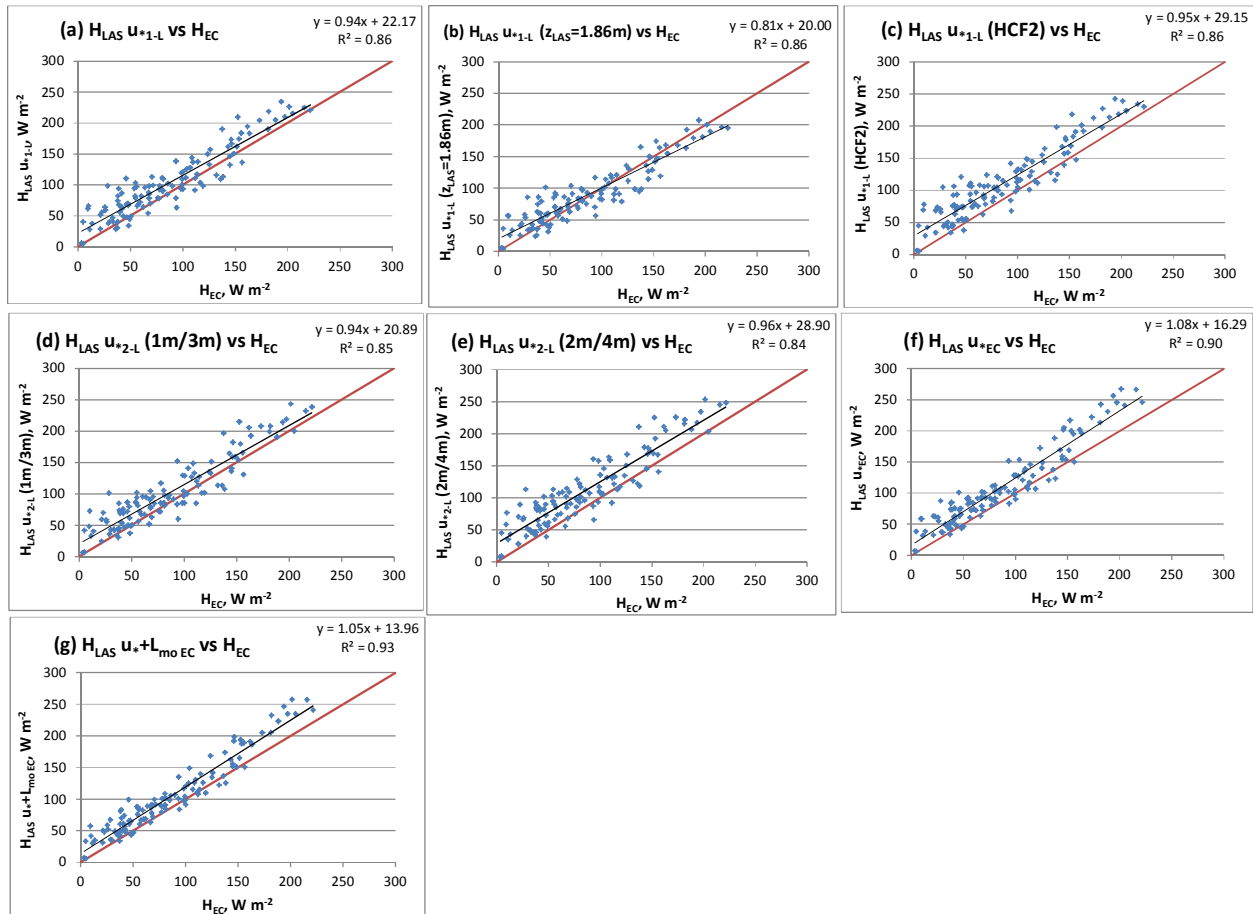


Figure 20. LAS to EC H comparison for LAS-2 (AVRC site) from August 28th – Oct. 21st; u_{*1-L} method (a), u_{*1-L} method with modified z_{LAS} (1.86 m) (b), u_{*1-L} method with alternate HCF (HCF2) (c), u_{*2-L} (1m/3m) method (d), u_{*2-L} (2m/4m) method (e), u_{*EC} method (f), and $u_{*+L_{mo}EC}$ method (g) versus H_{EC} . HCF1 unless otherwise noted; $z_{LAS} = 2.24$ m unless otherwise noted. Solid black line represents best-fit linear regression. Solid red line represents 1:1 line.

Figure 21 shows the mean uncertainties in H ($W m^{-2}$) along with the mean absolute deviation between H_{LAS} and H_{EC} (MAE, $W m^{-2}$) for the AVRC period of record. The slope (%) uncertainty (δH) for H_{LAS} was lowest for the u_{*1-L} method and highest for the u_{*EC} method. The mean δH in H_{EC} ($W m^{-2}$) was in all cases greater than the mean δH in H_{LAS} . It is apparent from Figure 21 that the sum of LAS and EC δH values would exceed (significantly) the corresponding MAE values for each method, suggesting that H_{LAS} was not extremely different from H_{EC} .

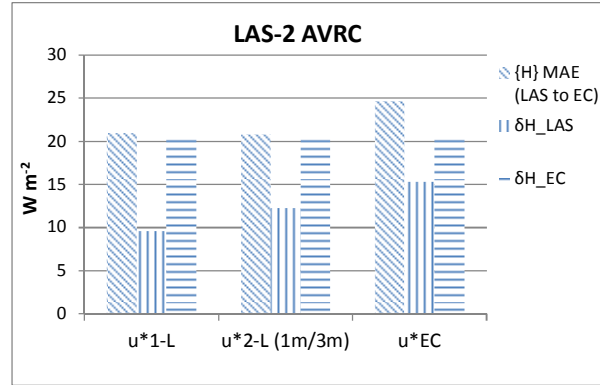


Figure 21. Plot showing mean period of record (August 28th – Oct. 21st) mean absolute error (MAE, $W m^{-2}$) between LAS-2 and EC (AVRC site) along with mean uncertainty (δ , $W m^{-2}$) for H_{LAS} and H_{EC} , for methods u^*_{1-L} , u^*_{2-L} (1m/3m), and u^*_{EC} . Diagonal line texture represents MAE, vertical line texture represents δH_{LAS} , and horizontal line texture represents δH_{EC} .

The above results, although strictly filtered, were for the entire August 28th – October 21st period of record, and thus did not consider the various field conditions observed during the period. A few additional analyses were performed to better understand the relationship between H_{LAS} and H_{EC} at the AVRC. The data from August 28th – Sept. 5th were isolated ($n = 58$) to represent the post-harvest condition when H was larger and conditions were expected to be similar in both alfalfa fields. Similarly, data from Sept. 21st – October 21st were isolated ($n = 33$) to represent conditions with substantial alfalfa growth when H was smaller. The northeast alfalfa field was being irrigated on Sept. 21st, and the southwest alfalfa field had already been irrigated. Although growth conditions were ahead in the southwest field, it is considered that the northeast field began to catch up after the Sept. 21st irrigation event, so that the Sept. 21st – Oct. 21st conditions were considered to be generally similar in both fields. [Figure 22](#) shows a regression plot of H_{LAS} (u^*_{EC} method) versus H_{EC} for both of the above-mentioned subsets. It is not apparent that the relationship between H_{LAS} and H_{EC} was different during both conditions, since the points were generally clustered together.

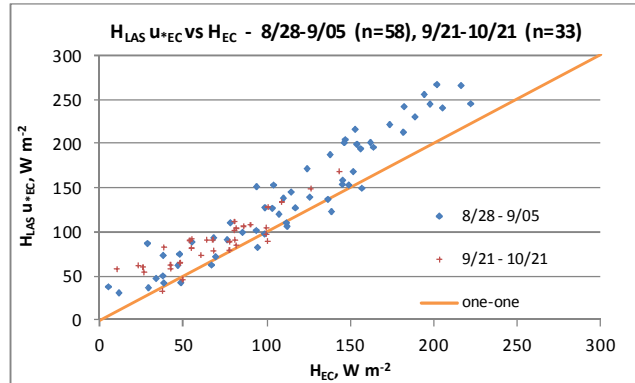


Figure 22. LAS to EC H comparison for LAS-2 (AVRC site) from August 28th – Sept. 5th (blue diamond; post-harvest conditions) and Sept. 21st – Oct. 21st (red plus sign; established crop conditions); $u^*_{EC} H_{LAS}$ method ($z_{LAS} = 2.24$ m). Solid orange line represents 1:1 line.

Another analysis was performed to investigate periods when H_{LAS} was well correlated with H_{EC} . This analysis was performed prior to the implementation of the EC ITT and stationarity filters, and wind direction was only filtered from 60° behind the EC tower, rather than from the entire northern direction. Data were isolated for conditions with MAE less than 15% and less than 10 W m^{-2} , where MAE was between H_{LAS} (u^*_{EC} method) and H_{EC} ($n = 81$). The following patterns were noted in the data: the data were distributed across the period of record (little to no bias based on the time period); the data were generally from a window within 2-3 hours of noon; the wind direction came from the east ($30^\circ < \text{WD} < 150^\circ$) 80% of the time; on average, 90% of the EC source area was within the southwest alfalfa field; on average, 73% of the LAS source area came from the southwest and northeast alfalfa fields. The source area statistics were based on the results from the Neftel et al. (2008) model. These findings suggest that good comparison of H_{LAS} and H_{EC} was dependent on the wind direction as well as the contribution of alfalfa field area to the measured flux. It is further notable that the LAS and EC source areas were ‘never’ completely similar due to the setup (locations) of the instruments and the nature of the LAS measurement; thus direct comparison of H_{LAS} and H_{EC} is uncertain.

MOST AGREEMENT (TIMPAS)

The Timpas MOST analysis was performed using the final LAS C_T^2 found for both the u_{*EC} and $u_*+L_{mo} EC$ method. However (especially for the Timpas case), the C_T^2 for different LAS processing methods was nearly identical, since the methods diverged only after the calculation of C_T^2 . The data were not filtered, except eventually to eliminate u_* less than 0.15 m s^{-1} . Figure 23 shows the general agreement between LAS data and the A1988 MOST curve for the three LAS units. The x -axis represents the stability condition, where $[(z_{LAS}-d)/L_{mo}]$ is zero for neutral conditions, positive for stable conditions, and negative for unstable conditions. The y -axis represents the $C_T^2 f_T$ – the reference curve was found using Equation 10, and the LAS data

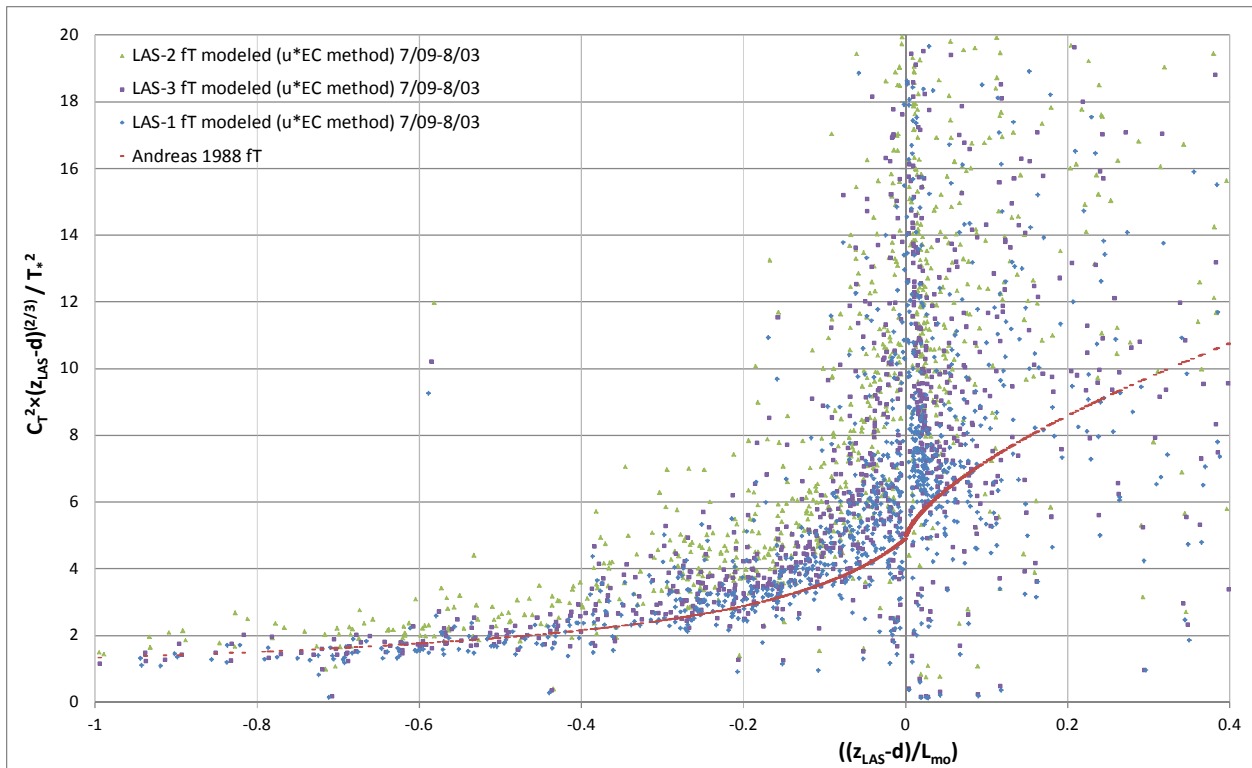


Figure 23. Scatter plots for evaluation of MOST agreement (Timpas site) for LAS-1, -2, and -3 for July 9th – August 2nd period. Data not filtered; C_T^2 taken from u_{*EC} method processing; Andreas (1988) f_T shown for stable and unstable conditions for reference. Horizontal (x) axis represents stability condition; vertical (y) axis represents f_T value (reference or LAS-modeled). Blue diamond represents LAS-1, green triangle LAS-2, and purple square LAS-3.

modeled f_T using Equation 5, rearranging to solve for f_T . The bias for $H_{LAS-2} > H_{LAS-3} > H_{LAS-1}$ observed in the inter-LAS comparison was reflected in this plot as well, and it is apparent that the LAS-1 data approach the reference curve more closely, especially for near-neutral conditions. Further analysis was performed for LAS-1 only. Scatter was dramatically reduced by limiting data to u_* greater than 0.15 m s^{-1} (Figure 24). It is also apparent that scatter was larger for stable condition data, which corroborates the lack of consensus in the literature regarding MOST validity for stable conditions (Kipp and Zonen B.V. 2007).

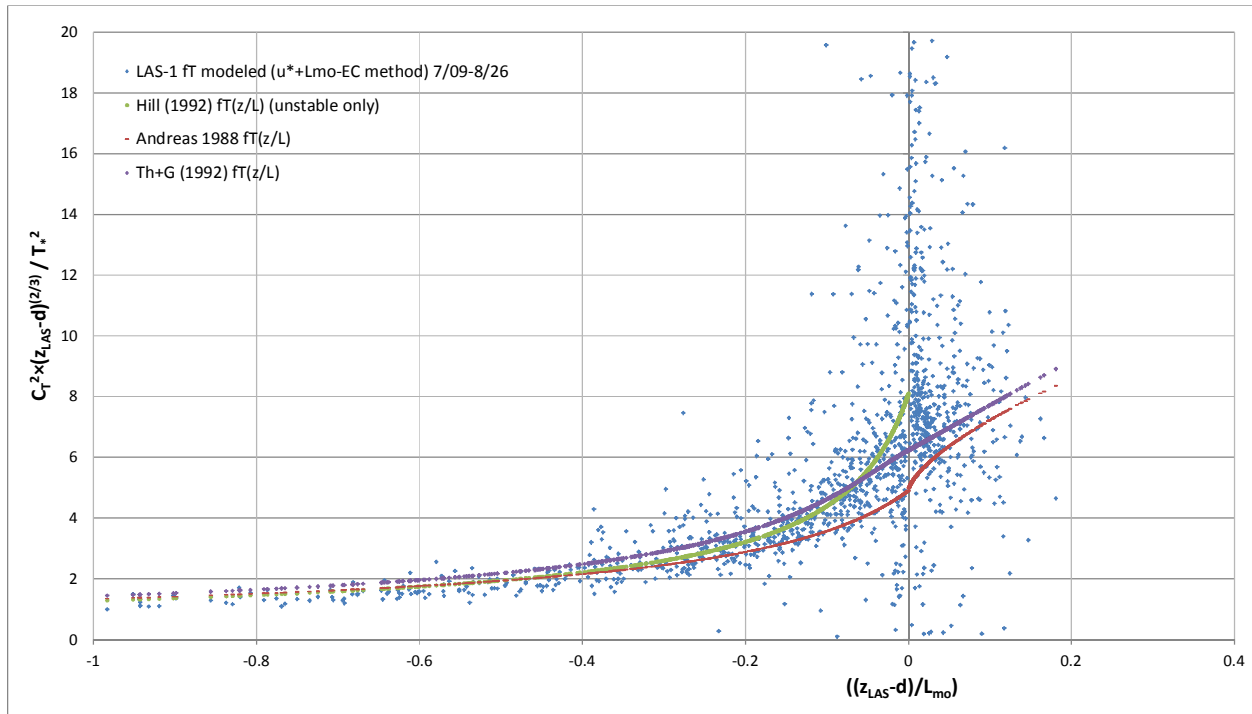


Figure 24. Scatter plot for evaluation of MOST agreement (Timpas site) for LAS-1 for July 9th – August 26th period. Data filtered for u_* greater than 0.15 m s^{-1} ; C_T^2 taken from $u_*+L_{mo} EC$ method processing; Andreas (1988) (red), Thiermann and Grassl (1992) (purple), and Hill et al. (1992) (green) f_T formulations shown for reference. Horizontal (x) axis represents stability condition; vertical (y) axis represents f_T value (reference or LAS-modeled).

Figure 24 shows the $C_T^2 f_T$ curves from H1992 and TG1992 in addition to the A1988 curve. The MOST agreement is good for unstable conditions for all curves. For near-neutral unstable and

stable data the LAS-1 data overestimated the A1988 f_T , which prompted the inclusion of the other f_T formulations. The TG1992 f_T was slightly larger than LAS-1 data for $[(z_{LAS}-d)/L_{mo}]$ less (more negative) than -0.1, but represented the best overall fit to the near-neutral data. The H1992 f_T , given only for unstable conditions, fit the LAS data well for -0.3 less than $[(z_{LAS}-d)/L_{mo}]$ less than -0.1, but was larger than the LAS data for more near-neutral conditions (Figure 24). A further check was to include LAS-1 data modified with z_{LAS} equal to 2.48 m (rather than 2.267 m) (Figure 25). This was achieved using the C_T^2 from the original u^*+L_{mo} EC method, and changing the height in the computation of f_T and $[(z_{LAS}-d)/L_{mo}]$. The results were not dramatically different, but showed further departure of the LAS data from the A1988 f_T curve; from Figure 25, the TG1992 and H1992 f_T curves appear to fit the LAS data similarly for near-neutral unstable conditions. Further, the stable conditions fit for the modified z_{LAS} case was worse for the A1988 and TG1992 f_T curves.

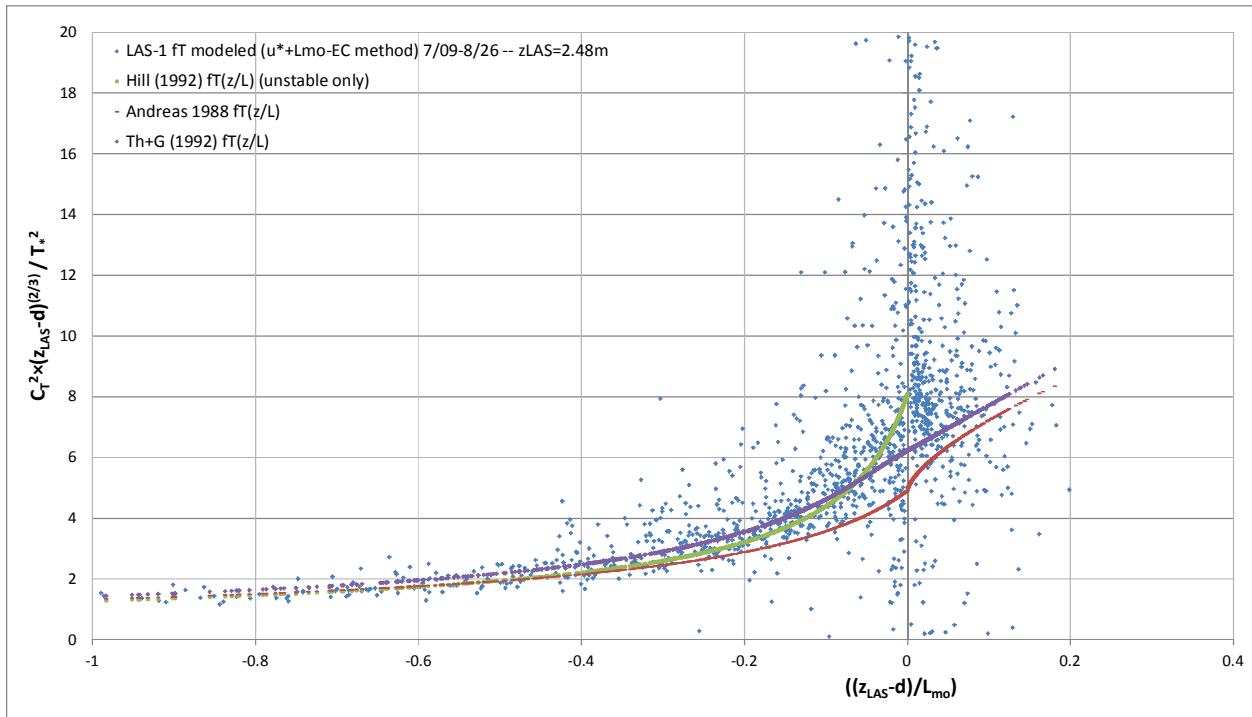


Figure 25. Same as Fig. 24, but the LAS-1 modeled f_T was modified for z_{LAS} equal to 2.48 m.

MOST AGREEMENT (AVRC)

The MOST analysis for the AVRC site was performed similarly to the Timpas analysis. Data were filtered if u_* was less than 0.1 m s^{-1} , in accordance with the filtering measures used for the AVRC analysis. The DB1993 f_T was included for stable conditions, and the LAS-2 data were checked for the original z_{LAS} (2.24 m) and the modified z_{LAS} (1.86 m). There was much more scatter apparent in the AVRC data relative to the Timpas data, although the fit for unstable data was relatively good (original z_{LAS} ; Figure 26).

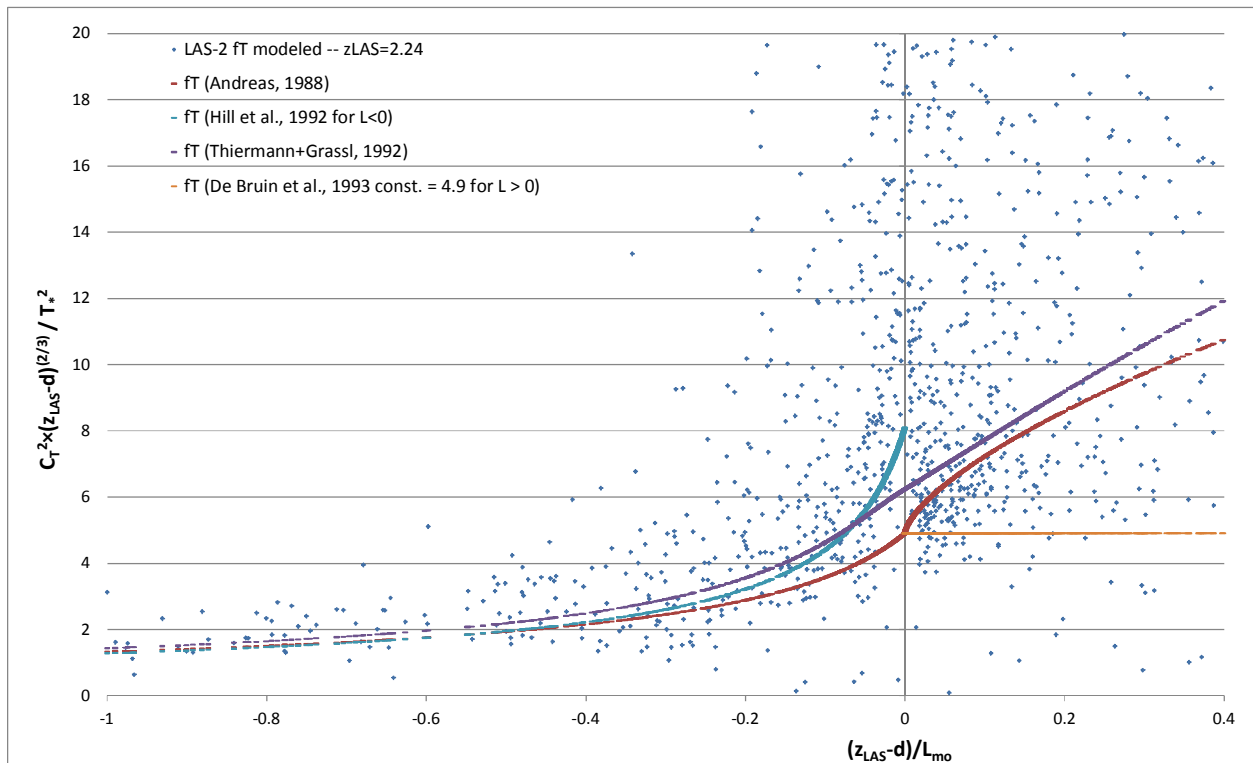


Figure 26. Scatter plot for evaluation of MOST agreement (AVRC site) for LAS-2 for August 28th – Oct. 21st period. Data filtered for u_* greater than 0.1 m s^{-1} ; C_T^2 taken from $u_* + L_{mo} EC$ method processing; Andreas (1988) (red), Thiermann and Grassl (1992) (purple), Hill et al. (1992) (blue), and De Bruin et al. (1993) (orange) f_T formulations shown for reference. Horizontal (x) axis represents stability condition; vertical (y) axis represents f_T value (reference or LAS-modeled).

It is apparent that the near-neutral unstable LAS data overestimated the A1988 f_T curve, but fit the curve fairly well for stable conditions. Despite the relatively large scatter, it appears the

H1992 f_T fit the near-neutral unstable LAS data best. For stable conditions, the A1988 curve appeared to fit the LAS data best. Further checking the modified z_{LAS} data showed the predicted f_T to trend slightly smaller (Figure 27). Nonetheless, the H1992 f_T still appeared to fit the near-neutral unstable data best, albeit some scatter. For the stable condition data, the constant DB1993 f_T appeared to fit the LAS data as well as or better than the A1988 stable f_T . Overall the scatter for the AVRC data made conclusions regarding the optimum f_T difficult.

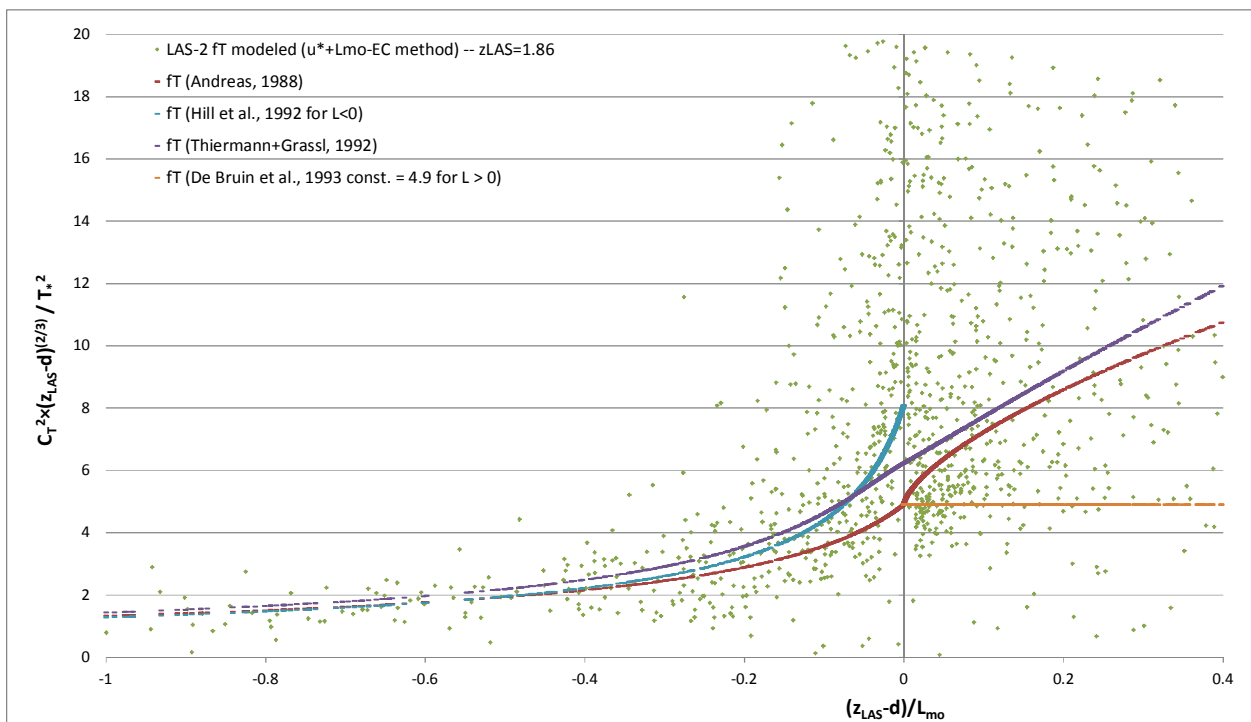


Figure 27. Same as Fig. 25 but the LAS-2 modeled f_T was modified for z_{LAS} equal to 1.86 m.

DISCUSSION

EFFECTS OF LAS ALIGNMENT ON H

It was found during the inter-LAS comparison period that inter-sensor biases in H ranged between 6-11% ($MBE/|\bar{O}|$) as long as the units were in good alignment. The alignment was judged by checking the LAS *Demod* signal – if the signal strength had not decreased from the initial setup value, the alignment was considered good. Scatter and bias were observed to increase after decrease in signal strength of one or more LAS units. In particular, periods of disagreement in H pattern between the well-aligned and poorly-aligned units seemed to correspond to periods of large wind speed during the evening. One possible explanation for this finding is that the misalignment of the units loosened the connection between the LAS head and support, making the unit more susceptible to wind speed vibrations. A possible explanation for the increased bias is noise resulting from the edge of the transmitter beam being too close to the receiver aperture. According to the manufacturer, the accuracy of the C_n^2 signal can be compromised due to this occurrence. Misalignment (horizontal or vertical) would naturally cause the beam edge to be closer to the receiver aperture (see App. 1). The reader may recall from the results that the trend between LAS-3 and -1 H was not apparently affected by the slip in alignment on July 8th, yet bias was apparently reduced after the July 21st improvement in LAS-3 alignment. Further, the increased bias between LAS-2 and -1 H after the July 8th misalignment was clearer, which supports the conclusion that, in general, misalignment of the LAS can cause a variable (scatter) and systematic (bias) change in the solution of H . In addition, the manufacturer recommends setting a lower limit on the *Demod* variable in order to ensure good quality of the C_n^2 output, which was set at -50 mV in this study. However, based on the observation with LAS-

2 that the solution of H was equally poor when the signal strength was at 20% (-160 mV) and when it was near zero (% , mV), the *Demod* lower limit would not have adequately controlled the quality of the LAS C_n^2 output. It seems more prudent to recommend flagging the C_n^2 solution after any significant (and prolonged) drop in signal strength, based on the results observed in this study.

FRICITION VELOCITY (u_*) FINDINGS

The findings for u_* for both (Timpas and AVRC) sites had some site-unique patterns and some commonalities. For both sites, the correlation between u_{*LWP} and u_{*EC} was (surprisingly) better for the 1-L method than the 2-L method. This refers to the relationship scatter as well as the bias between u_{*LWP} and u_{*EC} . The u_{*2-L} method depends on the difference between wind speed at two heights and therefore is considered subject to more uncertainty than the u_{*1-L} method. Further, for periods of low wind speed, where more scatter in the u_{*2-L} solution was observed, it is considered that especially the lower wind speed level (U_l) may have been affected by the minimum U threshold of the Wind Sentry 03101 sensor, which would have led to bias in the ΔU input to the u_{*2-L} method. Nonetheless, it is clear for the Timpas site that u_{*2-L} shows overestimation bias with respect to u_{*EC} for higher u_* values (Figure 14b). The reason for this bias is not known, however could be attributed to limitations in accuracy of either the Wind Sentry 03101 sensor or the CSAT3 sonic anemometer²⁷. Further, with the improved estimate of z_{om} (0.03 m) for the Timpas site u_{*1-L} showed a similar bias to overestimate u_{*EC} (Figure 14c). This finding suggests that u_{*1-L} and u_{*2-L} should be very similar if an appropriate value of z_{om} is used, which highlights the

²⁷ Justification for potential CSAT3 underestimation of u_* can be found in Kochendorfer et al. (2012), resulting from angle of attack induced underestimation of vertical wind speed.

advantage of the u_{*2-L} method to not require an estimate of z_{om} . Data from the AVRC site revealed clear bias between u_{*2-L} computed using different arm pairs (Figure 16c). The geometric mean height²⁸ of the 1m/3m method was 2.15 m compared to 3.37 m for the 2m/4m method. It is likely that the surface variability at the AVRC site contributed to the observed bias between methods, since the source area of the wind speed measurement depends on the sensor height. Meanwhile the EC sonic anemometer was installed at a height of 2 m and the u_{*1-L} method was derived from wind speed measurements at 2.47 m. The prediction of u_* using the 2m/4m method is considered to have been effected by areas outside of the alfalfa field more often than the other methods due to the larger effective height (3.37 m). For this reason, u_* derived from the 1m/3m method is considered to have been more representative of the alfalfa field, along with u_{*EC} and u_{*1-L} , such that the consequent observations can be made: The z_{om} estimate for the AVRC site may have been biased, considering the tendency for u_{*1-L} to be greater than $u_{*1m/3m}$, especially for larger u_* (assuming, as for Timpas, that u_{*1-L} should agree with u_{*2-L} with a correct z_{om} value). Nonetheless, $u_{*1m/3m}$ exhibited significant scatter with respect to u_{*EC} ($r^2 = 0.67$) in contrast to the better correlation observed between u_{*1-L} and u_{*EC} ($r^2 = 0.85$). Indeed both u_{*2-L} solutions exhibited the same apparent non-linearity with respect to u_{*EC} (Figure 16b, c), which was not evident with the u_{*1-L} solution. This suggests inconsistent performance of the u_{*2-L} method (especially at the AVRC), potentially due to the impact of the low wind speed threshold on the lower arm sensor, discussed above. Finally, the $u_{*1m/3m}$ solution showed bias to underestimate u_{*EC} especially for larger u_* (Figure 16b). This is in contrast to the observed overestimation of u_{*EC} for the Timpas site.

²⁸ Geometric mean height (z_m) defined as $z_m = (z_1 \times z_2)^{1/2}$

IMPACTS OF LAS EFFECTIVE HEIGHT DETERMINATION

The Timpas and AVRC sites under consideration in this study were largely flat locations. However, as the path length increases, opportunity for variability in the topography also increases. Despite limited information on the site topographies, it seemed apparent for both locations that there was variable slope within the LAS paths. More information on the details associated with the path height determination is in Appendix 2. For the Timpas site, the slope was apparently slightly concave, and slightly convex for the AVRC site. This led to an underestimation/overestimation of LAS height for the Timpas/AVRC location/s when estimating the height using only the transmitter and receiver heights. The estimated bias in LAS height was -9.4% for Timpas, and +17% for the AVRC. The expected sensitivity of H to bias in z_{LAS} was considered to be based on a $^{1/3}$ power relationship between H_{LAS} and z_{LAS} (Table 3), although Hartogensis et al. (2003) gave a comprehensive report on the sensitivity of H_{LAS} to z_{LAS} based also on the atmospheric stability. This is discussed further in the ‘ H_{LAS} model sensitivity’ discussion section. For the Timpas site, a test was performed including the adjustment of z_{LAS} for the expected bias. However, additional parameters were modified during the test, not permitting evaluation of the sensitivity of H_{LAS} to z_{LAS} . But for the AVRC, a test was performed with adjustment of only the z_{LAS} parameter (17% reduction), resulting in a mean 10% reduction in H_{LAS} . The impact of z_{LAS} was seemingly more for unstable (positive H) conditions (Figure 15b), which would be expected based on the more dominant impact of u^* (independent of z_{LAS}) during stable conditions. This result suggests an approximate 60% sensitivity of H_{LAS} to changes in z_{LAS} . Thus the careful determination of effective z_{LAS} is considered essential for accurate H estimation with the LAS.

LAS DATA EVALUATION WITH MONIN-OBUKHOV SIMILARITY THEORY (MOST)

The MOST f_T formulations for unstable and stable conditions from Andreas (1988; A1988), which were proposed by the manufacturer, were used in this study to relate the LAS C_T^2 signal to H . These formulations were modified slightly from those derived by Wyngaard et al. (1971) using data collected during the Kansas study mentioned in the methodology ‘Large Aperture Scintillometry Theory’ methodology section. Thiermann and Grassl (1992; TG1992) proposed the use of a differently formulated f_T derived from measurements made closer to the surface. Further, Hill et al. (1992; H1992) also presented an alternative formulation of the unstable f_T based on their own experiment. Finally, the De Bruin et al. (1993; DB1993) f_T for stable conditions was proposed due to large scatter observed in their data set for stable conditions. The results from this study validate the MOST f_T relationships for unstable conditions. Data from both sites fit all curves fairly well for $[(z_{LAS}-d)/L_{mo}]$ less (more negative) than -0.2. For near-neutral (unstable) data, the TG1992 and H1992 formulations were shown to fit the data better than the A1988 f_T for the Timpas and AVRC sites (Figure 24, 26). This may be explained with the TG1992 f_T by the particular consideration for near-neutral data in the formulation, since the LAS heights in this study were (also) relatively low (< 2.5 m). For stable conditions, the data from this study (Timpas and AVRC) suggested very little pattern with respect to $[(z_{LAS}-d)/L_{mo}]$, hereafter ζ , although the AVRC data did show some increase in f_T with ζ (Figure 26) similar to that described by the A1988 formulation. Stable data from the Timpas site were concentrated below ζ equal to 0.05 (Figure 24), indicating near-neutral conditions, which could explain the lack of pattern in the data. Further, the Timpas stable data were concentrated in an f_T range between 6 and 8, higher than the approximate value of 5.5 observed for the AVRC (near-neutral) stable data; the Timpas data conformed, in this regard, better to the stable TG1992 f_T

formulation, while the AVRC data conformed better to the recommended formulations of Andreas (1988) and De Bruin et al. (1993). The increased scatter observed with the AVRC data may be explained by an increased tendency for violation of MOST requirements at this site, due to the limited extent of horizontally homogeneous conditions. The scatter in the stable data for the Timpas site did not appear to have a significant impact on the relationship between H_{LAS} and H_{EC} for stable (negative H) conditions, based on the relatively low scatter observed in the regression of H_{LAS} (LAS-1, u^*_{EC} method) against H_{EC} (Figure 28). However, for positive H less than 150 W m^{-2} , H_{LAS} appeared to be biased greater than H_{EC} (LAS-1, u^*_{EC} method; Figure 29)²⁹. This observation could be explained by the bias observed in the Timpas LAS data to exceed the A1988 f_T curve for near-neutral unstable conditions, since an underestimated f_T would correspond to an overestimated H (Eqs. 5, 7). Although not shown here, this observation could also apply to the AVRC data, in that the same MOST observations were made for near-neutral unstable conditions, and H_{LAS} was also observed greater than H_{EC} for low H unstable conditions (Figure 20f).

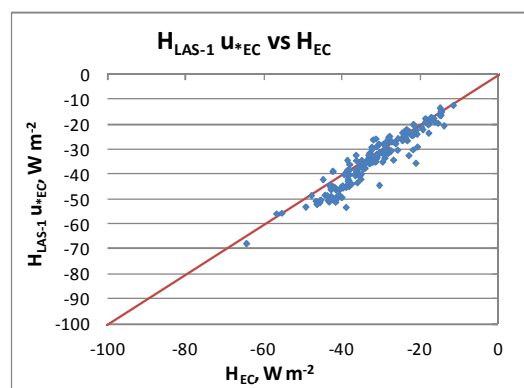


Figure 28. Same as Fig. 19c, showing only negative H_{LAS} and H_{EC} ; LAS to EC H comparison regression plot for LAS-1, u^*_{EC} method. Solid red line represents 1:1 line.

²⁹ Low positive H is used to represent near-neutral unstable conditions, although this would not always be appropriate.

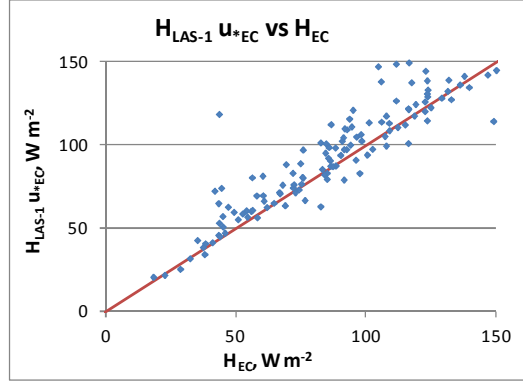


Figure 29. Same as Fig. 19c, showing only positive H_{LAS} and H_{EC} less than 150 W m^{-2} ; LAS to EC H comparison regression plot for LAS-1, u_{*EC} method. Solid red line represents 1:1 line.

EVALUATION OF H_{LAS} USING H_{EC}

TIMPAS

The preliminary results from the Timpas site in this study reveal the performance of LAS-1 to be very good, and better than the performance of LAS-2 and LAS-3 with respect to the EC data. In particular, the results from the u_{*EC} (or $u_* + L_{mo EC}$) method showed very good correlation between H_{LAS} and H_{EC} (Figure 19c, d; Table 4). The u_{*EC} method facilitated a good evaluation of the LAS C_T^2 solution, since no additional bias or uncertainty was added from the estimation of u_* , which was the same for the LAS and EC. Nonetheless, considering the potential for z_{LAS} to be higher than originally estimated, it appears that actual H_{LAS} would have overestimated H_{EC} . Further, the LAS-1 calibration drift described in the results section suggested that the U_{Ch2} signal from LAS-1 was underestimated, corresponding to an underestimation of H . The results showed that H_{LAS-1} was indeed less than that of the other LAS units in all cases during the inter-comparison (Figure 6a, b), suggesting that a well-calibrated LAS-1 would have predicted a larger H solution. Nonetheless, there was some evidence that the positive bias in H observed for LAS-2 and -3 relative to LAS-1 (during periods of good alignment) was due to discrepant power requirements

for each LAS. The analog power requirements for each LAS to achieve equal signal strength at the setup were 110 for LAS-2, 72 for LAS-3, and 55 for LAS-1. A similar issue was noted in Kleissl et al. (2008), where one LAS had significantly higher power requirements than the others; after this LAS was repaired, the predicted H was observed to trend significantly lower relative to a reference LAS. Correspondingly, the LAS-2 (and -3) unit(s) may have overestimated H_{LAS} due to this issue. In summary, H_{LAS-I} corrected for z_{LAS} and calibration drift would have likely trended higher, perhaps not very different from the solution presented in Figure 19e. In addition, H from LAS-2 and -3 may have been reduced considering alignment and power requirement issues, but increased considering actual z_{LAS} , suggesting overall little adjustment to H . These factors imply potential for LAS overestimation of H relative to H_{EC} , in line with the results reported by Kleissl et al. (2009) and Van Kesteren and Hartogensis (2011). Nonetheless, these conclusions assume accuracy of the H_{EC} solution. Considering the potential for underestimation of H by the EC, discussed in the introduction, the energy balance closure ratio (EBCR, Eq. 2) was computed for the EC H and λE data. The EBCR for the Timpas EC data was generally less than 1.0 during the daytime, increasing from morning to afternoon, with a mean value of 0.78 at 12:00 over the period of record. This suggests that the H and/or λE were underestimated on average during the daytime by a total of approximately 22% by the EC unit. Twine et al. (2000) suggested (and showed) that flux correction by preserving the EC Bowen Ratio (β) is preferred, though some other studies have suggested that the H_{EC} is more accurate than λE_{EC} . It is possible that H was underestimated by the EC, in which case LAS H appears to have the potential to be very accurate.

AVRC

The evaluation of LAS performance based on AVRC site data was complicated by the horizontal variability of surface conditions coupled with the different source areas of the LAS and EC instruments. The experimental setup was not optimum for validation of H_{LAS} using H_{EC} (Figure 3). Nonetheless, observations based on strictly filtered data showed H_{LAS} fairly well correlated with H_{EC} . H_{LAS} was generally observed to trend greater than H_{EC} , which could be attributed to two general issues: (1) contributing area to H_{LAS} was overall drier than that of H_{EC} and/or (2) instrument bias of LAS (or EC) resulted in H overestimation by the LAS (or H underestimation by the EC). The results from the Timpas site suggested that LAS-2 overestimated H (Figure 5, Figure 17)³⁰, which may explain some of the overestimation bias observed at the AVRC. The observation of better agreement (small bias) between H_{LAS} and H_{EC} when using z_{LAS} equal to 1.86 m suggests one alternate explanation for the otherwise-observed positive H_{LAS} bias. Nonetheless, as for Timpas, the certainty of this modified z_{LAS} estimate is questionable. The alternate humidity correction factor (HCF2) proposed by Wesely (1976) for r_{Tq} equal to zero was tested in a manner similar to the study of Odhiambo and Savage (2009), who cited that r_{Tq} increases toward 1.0 with increasing β . For this reason the HCF2 method was tested for the AVRC site data, where lower values of β were expected. However, the test in this study was not adequate to assess whether or not any benefit was gained in LAS performance using the alternate HCF, since other uncertainties (e.g. source area, z_{LAS}) may have played a role and also since the alternate HCF was applied to the entire dataset, without consideration of the actual value of r_{Tq} or β . Examining Figure 22, it is apparent that the H overestimation for larger H occurred during the August 28th – Sept. 5th period, when a generally dry condition was expected in both alfalfa fields (post-harvest). Further, the surrounding (southern) fields are considered to have been transpiring at a

³⁰ i.e., LAS-2 overestimated LAS-1 H , and LAS-1 $H \sim EC H$.

rate equal to or higher than that of the alfalfa fields during that period, suggesting that the LAS source area should not have been drier than the EC source area, unless the LAS received significant contribution from the dirt roads between fields. However, the low error subset analysis seemed to show that H_{LAS} was similar to H_{EC} when most of the contributing area to both instrument fluxes was from the alfalfa fields, suggesting that source area did play a role in the H_{LAS} to H_{EC} correlation. Similar to the Timpas site data, the EC EBCR was observed generally to increase from morning to afternoon, with a mean 12:00 value of 0.68, suggesting more significant lack of energy balance closure with respect to the Timpas site. A similar conclusion (as for the Timpas site) regarding potential underestimation of H_{EC} is considered applicable to the AVRC site. This may also explain some of the H_{LAS} overestimation bias observed. One further note in regards to the spatial variability for especially the LAS source area is the uncertainty introduced in the estimation of the LAS input variables such as z_{om} , β , and U . Use of u_{*EC} for LAS processing restricts the uncertainty to β , but it is notable that u_{*EC} may not have represented the u_* applicable to the LAS source area. This topic was not thoroughly addressed in this study, but is considered important for studies over heterogeneous terrain.

DIFFERENCES IN ANALYSIS FOR IRRIGATED VERSUS NON-IRRIGATED SITES

The AVRC site data included some post-harvest conditions, representing a larger H than typical of a (well-) irrigated site. However, especially the final month (Sept. 21st – October 21st) is considered representative of a well-irrigated condition for the AVRC site. In a low precipitation environment, irrigated lands tend to be oases in an otherwise dry area. When processing LAS data, there are some differences in the processing and analysis depending on whether the land is or is not irrigated. Two of the issues which are considered more important are the determination

of atmospheric stability and the estimation of Bowen Ratio (β). Over a well-irrigated terrain, the conditions can be often near-neutral (or stable) during the daytime, due to a transpiration-cooled canopy. This causes issues regarding resolving the temperature gradient in order to estimate stability for the determination of the final H solution. The impacts of this are apparent in [Figure 15f](#), which shows the relationship between LAS-derived H_{u^*EC} and $H_{u^*+Lmo\ EC}$. There is a significant amount of data showing negative $H_{u^*+Lmo\ EC}$ and positive H_{u^*EC} , indicating that an unstable condition was predicted by the SAT tower temperature (T) gradient while the EC measured fluxes predicted a stable condition. These data had already been filtered for T gradients smaller than 0.1 ($^{\circ}\text{C}$), which further suggests the difficulty of resolving the correct stability condition for an irrigated surface. Near-neutral stability conditions imply small H fluxes, which also correspond to a small (magnitude) β . The basis of the LAS theory is that C_n^2 is composed of predominantly H -induced scintillations (C_T^2); the inclusion of β to account for humidity fluctuations through the HCF relies on assumptions which may not be met regarding the correlation of temperature and humidity. The (EC) period of record β is shown for both sites in [Figure 30](#), which shows the difference in conditions between the Timpas and AVRC sites. It is apparent that the conditions at the AVRC from Sept. 14th to Oct. 14th (approx.) showed at times very small and even negative daytime β . Moene et al. (2003) showed that the use of the HCF assuming r_{Tq} equal to 1.0 resulted in significant C_T^2 error for small negative β . Therefore, use of the original HCF for the AVRC site may have resulted in H_{LAS} error especially during the mid-September to mid-October period. It is further notable that the relative contribution of H to the energy balance for a well-watered field is small, such that reasonably accurate estimates of ET could be obtained for the field even if estimates of H were not very accurate. This calls into question whether the investment of a LAS for estimation of H is worthwhile for application over

(fully) irrigated terrain. Nonetheless, the benefit of the LAS would increase with the magnitude of H , suggesting the potential for using the LAS in (e.g.) a limited irrigation management scenario, where ET would not be as dominant.

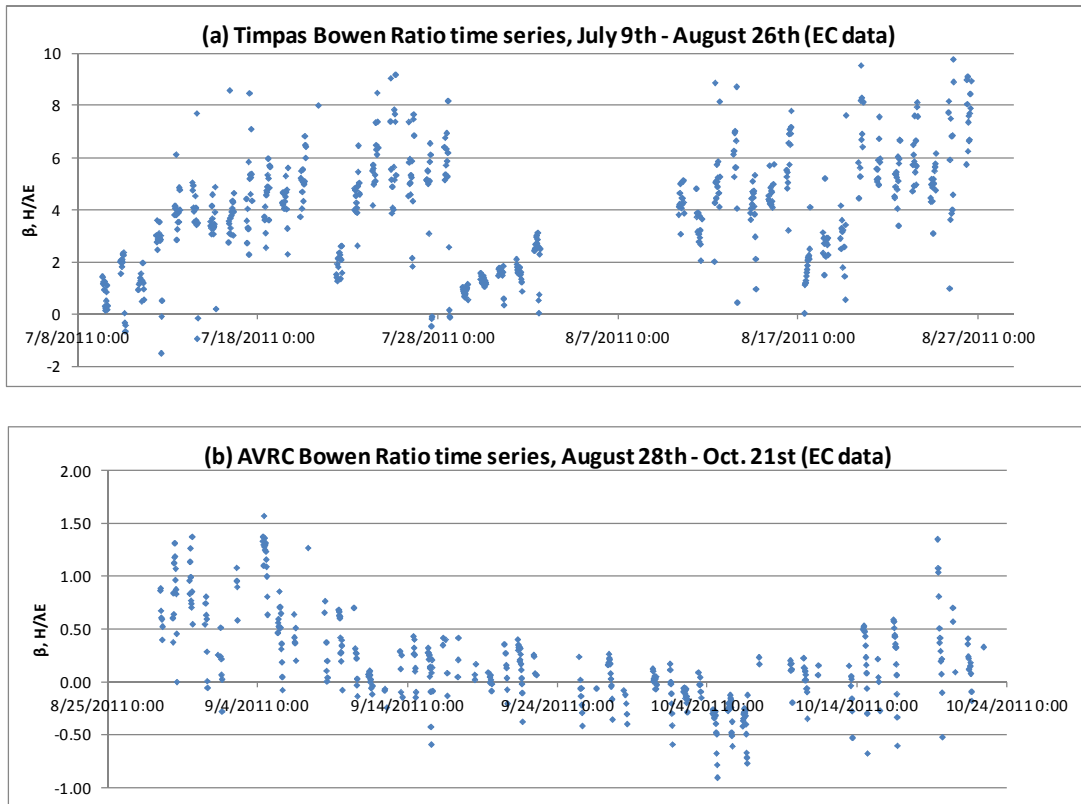


Figure 30. Bowen Ratio ($\beta, H/\lambda E$) time series plots showing patterns for Timpas (a) and AVRC (b) sites for the EC period of record (EC-derived β). AVRC data filtered to show only daytime (9:00 – 16:00), u_* greater than 0.1 m s^{-1} , and wind direction between $90 - 270^\circ$ from north; Timpas data filtered to show only daytime (9:00 – 16:00) and u_* greater than 0.15 m s^{-1} . The August 3rd – 9th gap in the Timpas data was due to technical difficulties with the data recording equipment.

H_{LAS} MODEL UNCERTAINTY

The propagation of uncertainty to H_{LAS} was found to be, in general, smaller than the computed value of δH_{EC} . For the Timpas case, mean values of δH_{LAS} for LAS-2 were larger than for LAS-1, but only because the magnitude of H was larger. The curve proposed by Nemitz et al. (2009) for δH_{EC} was based on observed deviations between H_{EC} resulting from different (EC) instruments

and processing methods. For this reason, the resulting δH_{EC} is considered a realistic estimation of the EC method uncertainty. Contrastingly, the estimation of H_{LAS} uncertainty was subject to several assumptions regarding the uncertainty of various model inputs. Marx et al. (2008) did not provide justification in their report for the values of δ shown in

Table 2, although they were considered before application to this study. Despite this consideration, the values of 0.5% δ for wind speed (U) and C_n^2 (which were applied in this study) from Marx et al. (2008) seem rather low. In particular, δU could have been larger for lower wind speeds affected by the sensor low value threshold. Low values of δU and δC_n^2 would have resulted in underestimation of δH_{LAS} . Further, the method of propagation was subject to assumptions regarding the sign of input uncertainties used to estimate positive and negative limits of δH_{LAS} (App. 9). Although consideration was given to the sign of the uncertainties in order to simulate realistic values of δH_{LAS} , the method was nonetheless approximate and could have resulted in under- or overestimation of δH_{LAS} . Values of mean δH_{LAS} for the Timpas and AVRC sites for different methods (of u_* determination) ranged between 9-14% and were very similar between the Timpas and AVRC sites³¹. This suggests that uncertainty was not increased due to decrease in β , as shown by Solignac et al. (2009), even though the δH_{LAS} values reported from the Solignac et al. study were based on the same method of determining β using the energy balance and H_{LAS} . The magnitude of δH found in this study falls in between that reported by Marx et al. (2008) and Solignac et al. (2009) and is therefore considered reasonable, despite the issues discussed above. It is notable that Marx et al. and Solignac et al. used the same values for input uncertainties.

³¹ Mean δH values were assessed by regressing δH ($W m^{-2}$) against $|H|$ ($W m^{-2}$) and taking the linear regression slope equal to the relative uncertainty. Regression r^2 values were better for the Timpas site, but in all cases better than 0.9.

H_{LAS} MODEL SENSITIVITY

Some of the H_{LAS} model sensitivities shown in Table 3 were not certain based on comments in the literature being in disagreement with the observations made based on the (LAS) equations. The results of this study tested the sensitivity of H_{LAS} to changes in z_{LAS} directly for the AVRC site. The above discussion ('Impacts of LAS effective height determination') suggests approximately 60% sensitivity of H_{LAS} to z_{LAS} . This is larger than the table value ($H \propto z_{LAS}^{1/3}$), where the $^{1/3}$ power corresponds to roughly 30% sensitivity, depending on the value of z_{LAS} . Hartogensis et al. (2003) suggested that the sensitivity is dependent on the atmospheric stability, where, for neutral conditions the sensitivity is approximately 50%, while the sensitivity would be roughly 100% for free convective (very unstable) conditions. The 60% sensitivity found in this study corresponds to (slightly) non-neutral conditions according to the range given by Hartogensis et al., which is considered to be reasonable based on the typical AVRC site conditions. In order to estimate the sensitivity of H_{LAS} to C_n^2 and C_T^2 , unstable H was plotted against C_T^2 and C_n^2 (Figure 31a, b) for a one day subset from the Timpas site. This test shows an approximate $1/2$ power relationship between H_{LAS} and C_n^2 and C_T^2 , which agrees with the value

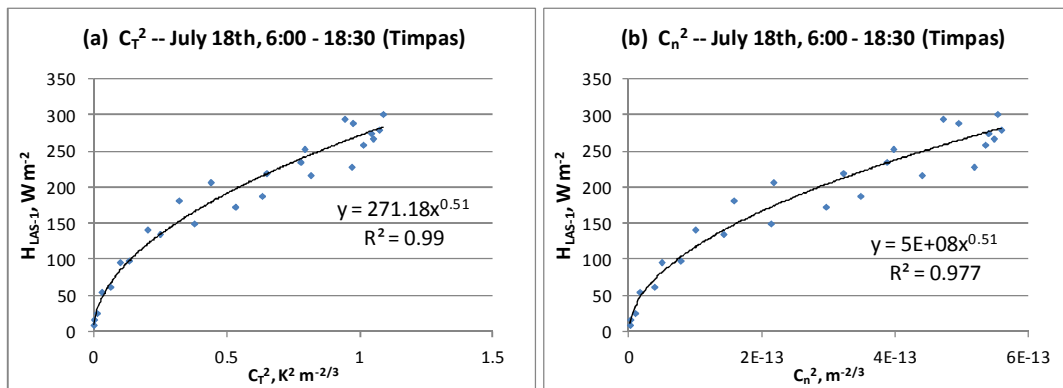


Figure 31. Scatter plots showing relationship of C_T^2 (a) and C_n^2 (b) versus positive H_{LAS} for a one-day subset (July 18th) at the Timpas site. Solid black line represents a best-fit power regression.

given in Table 3 and thus disagrees with the suggestion of Moene et al. 2005. Testing different methods of u_* input for LAS estimation of H at the Timpas and AVRC sites allowed evaluation of the sensitivity of H_{LAS} to u_* . The comparison of u_{*1-L} ($z_{om} = 0.014$ m) and u_{*2-L} at Timpas showed a regression slope of 0.79 for u_{*1-L} with respect to u_{*2-L} (Figure 13a). Comparison of H_{LAS} computed using the same u_* solutions showed a regression slope of 0.86, where H_{LAS} u_{*1-L} was less than H_{LAS} u_{*2-L} (Figure 8). This suggests that H was sensitive to changes in u_* , although not 100%. Further investigation of the same relationship between H_{LAS} u_{*1-L} and H_{LAS} u_{*2-L} showed a regression slope of 0.74 for stable H (Figure 10) and 0.92 for unstable H (Figure 9). This suggests that the sensitivity of H_{LAS} to u_* was more significant for stable (negative) H . A similar investigation with the AVRC data was not able to clearly reveal the magnitude of sensitivity of H_{LAS} to changes in u_* . The comparison of H_{LAS} for different u_* inputs was shown in Figure 15c-e and the comparison of u_* solutions was subsequently shown in Figure 16a-c. The scatter between H_{LAS} solutions for stable conditions in Figure 15d and e seems to reflect the scattered relationship between u_{*2-L} and u_{*EC} for the AVRC site (Figure 16b, c), which confirms the above finding of more extreme sensitivity of H_{LAS} to u_* for stable conditions. Observation of r^2 values better than 0.96 for the comparison of H solutions compared to r^2 values between 0.57 and 0.85 for comparison of the u_* solutions at the AVRC site does suggest that H_{LAS} was not 100% sensitive to changes in u_* , in agreement with the findings from the Timpas site.

CONCLUSIONS

Data were presented from two different sites to evaluate the performance of the Kipp and Zonen Large Aperture Scintillometer (LAS) to estimate sensible heat flux (H). The primary evaluation was carried out by comparison to eddy covariance measurements of H . Different methods were tested for the determination of H_{LAS} , largely dealing with the estimation or measurement of friction velocity (u_*). In addition, tests were performed for both sites to estimate the impact of potential input biases on the solution of H . The observations from the study are summarized here in accordance with the study objectives listed in the introduction.

1. Inter-LAS variability: Systematic biases in H between three LAS units were found between 6 and 11% ($MBE/|\bar{O}|$) for periods when all LASs were well-aligned. Biases may have been correlated with power requirement issues with LAS-2 and -3, as well as with the calibration drift found for LAS-1. Systematic and variable overestimation biases in H were introduced as a result of physical misalignment of the LAS, even if the signal strength still had a reasonable value.
2. H_{LAS} accuracy: Evaluation of LAS accuracy was clearer for the Timpas site since issues with heat flux source area differences between LAS and EC were all but irrelevant. Observations showed potential for accurate prediction of H with the LAS with respect to H_{EC} , specifically for LAS-1 at the Timpas site. Especially, uncertainty with regard to the LAS effective height suggested H_{LAS} may have been biased larger than H_{EC} – however, lack of energy balance closure of the EC, for the Timpas site, suggested that H_{EC} may have been underestimated. Both factors being considered, the accuracy of the LAS is considered reasonable. Data from the AVRC site showed H_{LAS} greater than H_{EC} , although consideration of the LAS effective height, LAS-2 performance at the Timpas site, and

lack of energy balance closure of the EC at the AVRC site may explain the LAS overestimation bias. Further, observations suggested LAS performance with respect to H_{EC} improved when the instrument source areas were more similar. Therefore, the reasonable accuracy found for the Timpas site seems to be confirmed at the AVRC site, despite the uncertainty introduced by spatial variability. It is notable that the conclusion of reasonable accuracy of the LAS would be dependent on which LAS was used, based on the conclusion of inherent instrument variability.

3. Accuracy of u_{*LWP} : There was some observation of good agreement between u_{*LWP} and u_{*EC} , specifically with u_{*1-L} . However, this was considered spurious due to biases in the estimate of z_{om} . Correction of z_{om} for the Timpas site resulted in good agreement between u_{*1-L} and u_{*2-L} , and apparent overestimation of u_* with respect to u_{*EC} . The disagreement was attributed to sensor biases with either the Wind Sentry 03101 sensor or the CSAT3 3D sonic anemometer. It was also not clear why overestimation biases with u_{*LWP} were observed for the Timpas site versus underestimation biases for the AVRC site. Scatter between u_{*2-L} and u_{*EC} was significant for u_* lower than 0.2 to 0.3 m s⁻¹, perhaps especially for the AVRC site, which was attributed to potential impact of the low wind speed threshold of the lower arm sensor on estimation of u_{*2-L} . The poor correlation between u_{*2-L} and u_{*EC} for lower u_* highlights the advantage of the u_{*1-L} method. However, the u_{*2-L} method offers the advantage of not requiring an estimate of z_{om} .
4. Irrigated versus dry environment: Evaluation of H_{LAS} using H_{EC} was more difficult at the AVRC site due to issues of the heat flux source area variability (i.e. the surface condition was variable and the source area of each instrument was not the same). However, similar conclusions were reached regarding the reasonable accuracy of the LAS for estimation of

H at both sites, suggesting the LAS can operate well in an irrigated environment. However, it was observed that the irrigated condition made determination of the atmospheric stability more difficult, and that theoretical assumptions related to the humidity correction factor may have been violated for the irrigated condition.

5. Sub-objectives:

- a. Uncertainty: It is clear that the estimate of uncertainty in H_{LAS} is only as good as the estimate of the input uncertainties. Therefore the 9 to 14% uncertainty in H_{LAS} found in this study carries limited weight, despite fair agreement with results of previous studies. Experimental determination of the uncertainty of LAS H may be preferable. Further, uncertainty in H_{LAS} was found in this study not to be sensitive to the overall magnitude of β .
- b. Sensitivity: Approximately 60% sensitivity of H_{LAS} to z_{LAS} was found for the AVRC site, where sensitivity was apparently more for unstable conditions. Approximately 67% sensitivity of H_{LAS} to u^* was found for the Timpas site, where sensitivity was clearly more for stable conditions and less for unstable conditions. This finding was confirmed with data from the AVRC site. Further, experimental results showed a $\frac{1}{2}$ power relationship between H_{LAS} and C_n^2 . Finally, H_{LAS} appeared to be relatively insensitive to the scatter observed with the LAS stable data with respect to the Andreas (1988) MOST function. However, H_{LAS} may have exhibited some sensitivity to the overestimation observed with the LAS near-neutral unstable data relative to the Andreas (1988) MOST function.
- c. MOST agreement: LAS data were observed to trend above the prescribed Andreas (1988) MOST similarity function for near-neutral unstable conditions.

Agreement with the Thiermann and Grassl (1992) and the Hill et al. (1992) functions in this range was better. Significant scatter was observed for LAS stable data, showing little or no trend with respect to the stability variable (ζ). Scatter was also more significant overall with the AVRC data, attributed to tendency for violation of MOST requirements.

Based on the observations from the study, several practical recommendations for use of the LAS are provided. The Kipp and Zonen LAS should be calibrated against a reliable reference, such as an Eddy Covariance system or one of the more robust LAS models tested by Van Kesteren and Hartogensis (2011) or Kleissl et al. (2009), in order to evaluate whether the sensor is subject to inherent bias, based on the observation of inter-sensor variability. Filtering of LAS data based on criteria discussed in the methodology section resulted in removal of up to approximately 60% of the data, however the majority of data filtered were from the early morning and evening periods, suggesting the usability of the LAS was not greatly affected by data filtering. The LAS may be most practically used for a condition of either partial (limited) or no irrigation, based on the relatively small magnitude of H in a fully irrigated condition. The correlation of temperature and humidity (r_{Tq}) should be considered before application of the humidity correction factor in calculation of C_T^2 if the LAS is applied in a moist / irrigated location. A more accurate and precise air temperature sensor than the HMP45C from Vaisala, Inc. (distributed by Campbell Scientific, Inc. (CSI), Logan, UT) is suggested for measuring air temperature at two heights for determination of the atmospheric stability condition. This would be more relevant if the LAS is used in a moist or irrigated location. The u_{*2-L} method may be preferable to avoid estimation of z_{om} ; however, a more sensitive and accurate sensor than the Wind Sentry 03101 from R.M. Young Co. (distributed by CSI, Logan, UT) is recommended to improve accuracy, especially for

low wind speeds. Accurate determination of LAS effective height is recommended, based on the observed sensitivity of H_{LAS} to this parameter. If the LAS is used at a relatively low height (e.g., 2 m), use of the Thiermann and Grassl (1992) or Hill et al. (1992) MOST f_T functions are recommended for unstable conditions, rather than the Andreas (1988) function. Finally, if the signal strength (*Demod*) of the LAS is observed to drop significantly (and not return to its original value without re-alignment) it is recommended to re-align the LAS as soon as possible to avoid loss of data integrity. In this regard, telemetry would be helpful to monitor the *Demod* signal on a real time basis.

REFERENCES

- Allen, R.G., Pereira L.S., Howell, T.A., Jensen, M.E. 2011. Evapotranspiration information reporting: I. Factors governing measurement accuracy. *Agric. Water Manage.* 98, 899-920.
- Allen, R.G., Tasumi, M., Trezza, R. 2007. Satellite-based energy balance for mapping Evapotranspiration with internalized calibration (METRIC) – Model. *J. Irrig. Drain. Eng.* 133 (4), 380-394.
- Andreas, Edgar L. 1988. Estimating Cn₂ over snow and sea ice from meteorological data. *J. Opt. Soc. Am.* 5 (4), 481-495.
- Arya, S. Pal. 2001. *Introduction to Micrometeorology, 2nd Ed.* Academic Press, San Diego, CA, 420 pp.
- Bastiaanssen, W.G.M., Menenti, M., Feddes, R.A., Holtslag, A.A.M., 1998. A remote sensing energy balance algorithm for land (SEBAL): 1. Formulation. *Hydrology*, 212-213, 198-212.
- Brunsell, N.A., Ham, J.M., Arnold, K.A. 2011. Validating remotely sensed land surface fluxes in heterogeneous terrain with large aperture scintillometry. *Int. J. Remote Sens.* 32 (21), 6295-6314.
- Brutsaert, Wilfried. 1982. *Evaporation into the atmosphere: Theory, History, and Applications.* Kluwer Academic Publishers, Norwell, MA, 299 pp.
- Campbell Scientific, Inc., 2003. *HFT3 Soil heat flux plate instruction manual.* Campbell Scientific, Inc., Logan, UT.
- *Campbell Scientific, Inc., 2009. *253 and 257 (Watermark 200) Soil matric potential sensors instruction manual.* Campbell Scientific, Inc., Logan, UT.
- Clement, Robert. 1999. EdiRe Data Software. 1.5.0.10 Edition. University of Edinburgh, Edinburgh, England. (Available from: <http://www.geos.ed.ac.uk/abs/research/micromet/EdiRe/>)
- De Bruin, H.A.R., Kohsiek, W., Van Den Hurk, B.J.J.M. 1993. A verification of some methods to determine the fluxes of momentum, sensible heat, and water vapour using standard deviation and structure parameter of scalar meteorological quantities. *Boundary Layer Meteorol.* 63, 231-257.
- Dyer, A.J. 1974. A Review of Flux-Profile Relationships. *Boundary Layer Meteorol.* 7, 363-372.
- Foken, Thomas. 2008a. The Energy Balance Closure Problem: An Overview. *Ecol. Appl.* 18 (6), 1351-1367.
- Foken, Thomas. 2008b. *Micrometeorology* (Edited for English by Carmen J. Nappo). Springer-Verlag, Berlin Heidelberg, Germany, 306 pp.

Foken, Th. and Wichura, B. 1996. Tools for quality assessment of surface-based flux measurements. *Agric. For. Meteorol.* 78, 83-105.

Gowda, Prasanna. 2010. Scintillometry for regional ET mapping applications, University of Nebraska-Lincoln Spring 2010 Water Seminar Series, (PPT; Available from: <http://watercenter.unl.edu/SpringSeminars/SpringSeminarSeries2010.asp>)

Gowda, P. H., Chávez, J.L., Howell, T.A., Marek, T.H., New, L.L. 2008. Surface energy balance based Evapotranspiration mapping in the Texas High Plains. *Sensors*, 8, 5186-5201.

Gowda, P. H., Chávez, J.L., Colaizzi, P.D., Evett, S.R., Howell, T.A., Tolk, J.A. 2007. Remote sensing energy balance algorithms for mapping ET: Current status and future challenges. *Trans. ASABE*, 50 (5), 1639-1644.

Green, A. E. and Hayashi, Y. 1998. Use of the Scintillometer technique over a rice paddy. *J. Agric. Meteorol.* 54 (3), 225-234.

Hartogensis, Oscar K., 2006. *Exploring Scintillometry in the Stable Atmospheric Surface Layer – Appendix 5A. Inner Scale Sensitivity of the LAS*. Ph.D. Dissertation: 141-143, Wageningen University, Meteorology and Air Quality Group, Wageningen, Netherlands.

Hartogensis, O.K., Watts, C.J., Rodriguez, J.-C., De Bruin, H.A.R. 2003. Derivation of an effective height for scintillometers: La Poza experiment in Northwest Mexico. *J. Hydrometeorol.* 4, 915-928.

Hill, R.J., Ochs, G.R., Wilson, J.J. 1992. Measuring surface-layer fluxes of heat and momentum using optical scintillation. *Boundary Layer Meteorol.* 58, 391-408.

Hoedjes, J.C.B., Zuurbier, R.M., Watts, C.J. 2002. Large Aperture Scintillometer used over a homogeneous irrigated area, partly affected by regional advection. *Boundary Layer Meteorol.* 105, 99-117.

Hsieh, C., Katul, G., Chi, T. 2000. An approximate analytical model for footprint estimation of scalar fluxes in thermally stratified flows. *Adv. Water Resour.* 23, 765-772.

**Jarvis, P.G., Massheder, J.M., Hale, S.E., Moncrieff, J.B., Rayment, M., Scott, S.L., 1997. Seasonal variation of carbon dioxide, water vapor, and energy exchanges of a boreal black spruce forest. *J. Geophys. Res.* 102 (D24), 28953–28966.

Kaimal, J. and Finnigan, J. 1994. *Atmospheric Boundary Layer Flows: Their structure and measurement*. Oxford University Press, New York, New York, 289 pp.

Kipp and Zonen B.V. 2007. *LAS and X-LAS (Extra) Large Aperture Scintillometer instruction manual*. Kipp and Zonen B.V., Delft, Netherlands.

- Kleissl, J., Watts, C.J., Rodriguez, J.C., Naif, S., Vivoni, E.R., 2009. Scintillometer intercomparison study – Continued. *Boundary Layer Meteorol.* 130, 437-443.
- Kleissl, J., Gomez, J., Hong, S.-H., Hendrickx, J.M.H, Rahn, T., Defoor, W.L. 2008. Large Aperture Scintillometer intercomparison study. *Boundary Layer Meteorol.* 128, 133-150.
- Kochendorfer, J., Meyers, T.P., Frank, J., Massman, W.J., Heuer, M.W. 2012. How well can we measure the vertical wind speed? Implications for fluxes of energy and mass. *Boundary Layer Meteorol.* DOI 10.1007/s10546-012-9738-1, published online June 8th, 2012.
- Kormann, R. and Meixner, F. X., 2001. An analytical footprint for non-neutral stratification. *Boundary Layer Meteorol.* 99, 207-224.
- Lagouarde, J.P., Jacob, F., Gu, X.F., Olioso, A., Bonnefond, J.M., Kerr, Y., McAneney, K.J., Irvine, M. 2002. Spatialisation of sensible heat flux over a heterogeneous landscape. *Agronomie*, 22 (6), 627-633.
- Marx, A., Kunstmann, H., Schuettemeyer, D., Moene, A.F. 2008. Uncertainty analysis for satellite derived sensible heat fluxes and Scintillometer measurements over Savannah environment and comparison to mesoscale meteorological simulation results. *Agric. For. Meteorol.* 148, 656-667.
- Meijninger, Wouter M.L. 2003. *Surface fluxes over natural landscapes using scintillometry*. Ph.D. Dissertation, 164 pp., Wageningen University, Meteorology and Air Quality Group, Wageningen, Netherlands.
- *Meijninger, W.M.L., Hartogensis, O.K., Kohsiek, W., Hoedjes, J.C.B., Zuurbier, R.M., De Bruin, H.A.R. 2002. Determination of area-averaged sensible heat fluxes with a Large Aperture Scintillometer over a heterogeneous surface – Flevoland field experiment. *Boundary Layer Meteorol.* 105, 37-62.
- Moene, Arnold F. 2003. Effects of water vapour on the structure parameter of the refractive index for near-infrared radiation. *Boundary Layer Meteorol.* 107, 635-653.
- Moene, A.F., Meijninger, W.M.L., Hartogensis, O.K., Kohsiek, W., De Bruin, H.A.R. 2005. *A review of the relationships describing the signal of a Large Aperture Scintillometer*. Internal Report 2004/2 v.1.1, Wageningen University, Meteorology and Air Quality Group, Wageningen, Netherlands.
- Moore, C.J. 1986. Frequency response corrections for Eddy Correlation systems. *Boundary Layer Meteorol.* 37, 17-35.
- Neftel, A., Spirig, C., Ammann, C. 2008. Application and test of a simple tool for operational footprint evaluations. *Environ. Pollut.* 152, 644-652.

Nemitz, E., Hargreaves, K.J., Neftel, A., Loubet, B., Cellier, P., Dorsey, J.R., Flynn, M., Hensen, A., Weidinger, T., Meszaros, R., Horvath, L., Daemmgen, U., Fruehauf, C., Loepmeier, F.J., Gallagher, M.W., Sutton, M.A. 2009. Intercomparison and assessment of turbulent and physiological exchange parameters of grassland. *Biogeosciences*, 6, 1445-1466.

Ochs, G. R. and Hill, R. J., 1982. A study of factors influencing the calibration of optical Cn2 meters. NOAA Technical Memorandum ERL WPL-106. (Available from: National Technical Information Service, 5285 Port Royal Road, Springfield, VA 22161, U.S.A.)

Odhiambo, G.O., Savage, M.J. 2009. Sensible heat flux by surface layer scintillometry and eddy covariance over a mixed grassland community as affected by Bowen Ratio and MOST formulations for unstable conditions. *J. Hydrometeorol.* 10, 479-492.

Schmid, Hans P. 1994. Source areas for scalars and scalar fluxes. *Boundary Layer Meteorol.* 67, 293-318.

Schotanus, P., Nieuwstadt, F.T.M, De Bruin, H.A.R. 1983. Temperature measurement with a Sonic Anemometer and its application to heat and moisture fluxes. *Boundary Layer Meteorol.* 26 (1), 81-93.

Schuettmeyer, Dirk. 2005. *The surface energy balance over drying semi-arid terrain in West Africa*. Ph.D. Dissertation, 154 pp., Wageningen University, Meteorology and Air Quality Group, Wageningen, Netherlands.

Solignac, P.A., Brut, A., Selves, J.-L., Béteille, J.-P., Gastellu-Etchegorry, J.-P., Keravec, P., Béziat, P., Ceschia, E. 2009. Uncertainty analysis of computational methods for deriving sensible heat flux values from Scintillometer measurements. *Atmos. Meas. Tech. Discuss.* 2, 1383-1417.

Taylor, John R. 1997. *An Introduction to Error Analysis: The study of uncertainties in physical measurements*, 2nd Ed. University Science Books, Sausalito, CA, 327 pp.

Thiermann, V. and Grassl, H. 1992. The measurement of turbulent surface-layer fluxes by use of bichromatic scintillation. *Boundary Layer Meteorol.* 58, 367-389.

Timmermans, W.J., Su, Z., Oliosio, A. 2009. Footprint issues in scintillometry over heterogeneous landscapes. *Hydrol. Earth Syst. Sci.* 13, 2179-2190.

Twine, T.E., Kustas, W.P., Norman, J.M., Cook, D.R., Houser, P.R., Meyers, T.P., Prueger, J.H., Starks, P.J., Wesely, M.L. 2000. Correcting Eddy-Covariance flux underestimates over a grassland. *Agric. For. Meteorol.* 103, 279-300.

**Unland, H.E., Houser, P.R., Shuttleworth, W.J., Yang, Z.-L., 1996. Surface flux measurement and modeling at a semi-arid Sonoran Desert site. *Agric. For. Meteorol.* 82 (1-4), 119–153.

Van Kesteren, B. and Hartogensis, O.K. 2011. Analysis of the systematic errors found in the Kipp & Zonen Large Aperture Scintillometer. *Boundary Layer Meteorol.* 138 (3), 493-509.

*Varble, J.L., Chávez, J. L. 2011. Performance evaluation and calibration of soil water content and potential sensors for agricultural soils in eastern Colorado. *Agric. Water Manage.* 101 (1), 93-106.

*Von Randow, C., Kruijt, B., Holtslag, A.A.M., De Oliveira, M.B.L. 2008. Exploring Eddy-Covariance and Large-Aperture Scintillometer measurements in an Amazonian rainforest. *Agric. For. Meteorol.* 148, 680-690.

Wang, T., Ochs, G.R., Clifford, S.F., 1978. A saturation-resistant optical scintillometer to measure Cn2. *J. Opt. Soc. Am.* 68 (3), 334-338.

Webb, E.K., Pearman, G.I., Leuning, R. 1980. Correction of flux measurements for density effects due to heat and water vapour transfer. *Quart. J. R. Met. Soc.* 106, 85-100.

Wesely, Marvin L. 1976. The combined effects of temperature and humidity fluctuations on refractive index. *J. Appl. Meteorol.* 15, 43-49.

Willmott, Cort J. 1982. Some comments on the evaluation of model performance. *Bulletin Amer. Meteorol. Soc.* 63 (11), 1309-1313.

Wilson, K., Goldstein, A., Falge, E., Aubinet, M., Baldocchi, D., Berbigier, P., Bernhofer, C., Ceulemans, R., Dolman, H., Field, C., Grelle, A., Ibrom, A., Law, B.E., Kowalski, A., Meyers, T., Moncrieff, J., Monson, R., Oechel, W., Tenhunen, J., Valentini, R., Verma, S. 2002. Energy balance closure at FLUXNET sites. *Agric. For. Meteorol.* 113, 223-243.

**Wright, I.R., Gash, J.H.C., Da Rocha, H.R., Shuttleworth, W.J., Nobre, C.A., Maitelli, G.T., Zamparoni, C.A.G.P., Carvalho, P.R.A., 1992. Dry season micrometeorology of central Amazonian ranchland. *Quart. J. R. Met. Soc.* 118 (508), 1083–1099.

Wyngaard, J.C., Izumi, Y., Collins, S.A. Jr. 1971. Behavior of the refractive-index structure parameter near the ground. *J. Opt. Soc. Am.* 61 (12), 1646-1650.

**Reference appears in Appendices section only; other references in Appendices section appear in document body as well.*

***Reference cited in Twine et al. 2000*

APPENDIX 1. LAS SETUP/ALIGNMENT PROCEDURE

The manufacturer (Kipp and Zonen B.V., Delft, Netherlands) provides detailed instructions on the setup procedure for the LAS, which are summarized here. A setup height of at least 1.5 m is recommended, for a few reasons, among them to avoid saturation of the C_n^2 signal. Another motivation is to reduce risk of measuring C_n^2 in the near-surface roughness sub-layer, which would violate the requirements of MOST. A north-south path alignment is recommended in order to avoid direct sunlight on the transmitter or receiver apertures at sunrise/-set, which can apparently damage the optical parts. The LAS transmitter and receiver are supplied with horizontal and vertical alignment (pan and tilt) mechanisms and a base (flange) which facilitates mounting of the LAS units on a support structure. The manufacturer recommends a solid support structure (e.g. tripod) which will prevent vibration of the LAS, since this can affect the C_n^2 readings. The transmitter and receiver are first aligned with one another using manufacturer-provided scopes. Subsequently, the units are powered on with connection to a stable power supply, the transmitter power dial is set at a preliminary value, and the receiver is checked for a signal. Two people are needed to carry out the alignment procedure. Provided that some signal is observed, one person begins the fine alignment by adjusting the horizontal alignment of (e.g.) the transmitter, moving the LAS slowly back and forth while communicating with the person at the receiver in order to find the peak signal (horizontal beam center). Next, the vertical alignment is adjusted in a similar manner. Once the peak signal is reached for the optimum horizontal and vertical alignment, the unit is secured in that position. The procedure is then repeated for the receiver. The manufacturer recommends operation at a signal strength of 50%, which can be achieved by adjusting the power dial on the transmitter after the alignment procedure. However, it is considered that the absolute value of the signal strength is not as important as the good alignment of the transmitter and receiver. Finally, the user must (carefully) estimate the LAS path length and height; depending on the site topography, the elevation along the path may be necessary. In the case that multiple LAS units are set up together, horizontal separation should be greater than the beam width which expands to approximately $0.01 \times L_{LAS}$ from transmitter to receiver (Kleissl et al. 2008). For the Timpas site, the horizontal separation of approximately 20 m was much larger than the approximate 6 m requirement. In addition, the center LAS (-2) was directed in opposite direction to the other LAS units (Fig. 2), which also works to avoid inter-contamination of the LAS signals.

APPENDIX 2. LAS EFFECTIVE HEIGHT DETERMINATION

The general method presented here for estimating the LAS height using the path-weighting function of the LAS has been suggested as an approximate method by Hartogensis et al. (2003), while rigorously, the effective z_{LAS} would be computed for each time step due to effects of stability (L_{mo}) (Hartogensis et al. 2003). The same authors further indicate that the approximate method is sufficient for cases where topography is not very variable over the LAS path, which was assumed to apply to both sites in this study. The handheld GPS (Garmin eTrex) elevation data for the Timpas and AVRC sites had questionable accuracy, especially in regards to estimating the change in elevation for a relatively flat area. More information on the site topography was sought from the USDA NRCS geospatial data gateway (<http://datagateway.nrcs.usda.gov>). An Otero County digital raster graphic (DRG) 10 ft contour map was downloaded courtesy of the USDA NRCS National Geospatial Management Center (NGMC, Fort Worth, TX). The geo-rectified map was imported into ArcGIS 9.3 ArcMap, allowing the overlay of the LAS unit GPS locations for both sites. Approximate linear interpolation methods were used to estimate the elevation of the LAS transmitter (T), receiver (R), and some internal point along the path (e.g. path center). Figures A2.1 and A2.2 show map subsets for the Timpas and AVRC sites, respectively, also showing the LAS T and R locations.

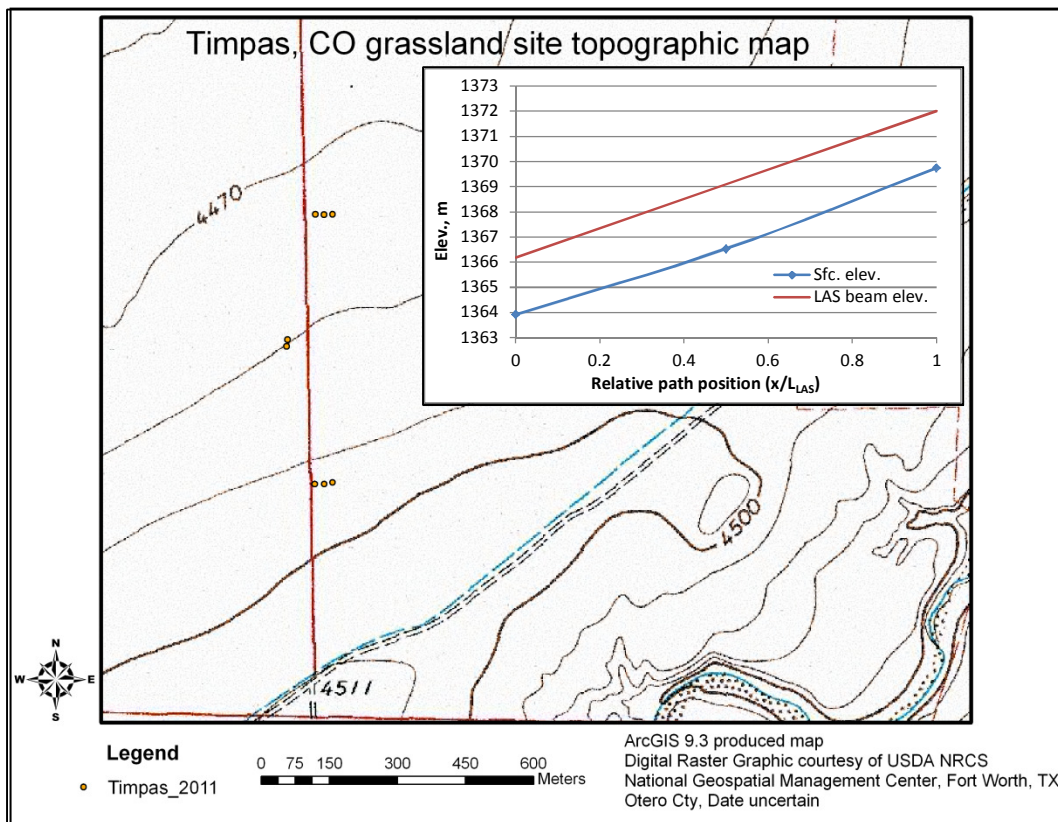


Figure A2.1. Topographic map showing 10 foot contours for Timpas grassland site. LAS locations are shown with orange points. Linear interpolation between the transmitter, path center, and receiver was used to estimate the path elevation profile. Profile plot is shown in upper right of image, with elevation in meters, for estimated elevations along LAS path. Solid red curve represents estimated beam elevation, based on setup height (2.267 m) off ground.

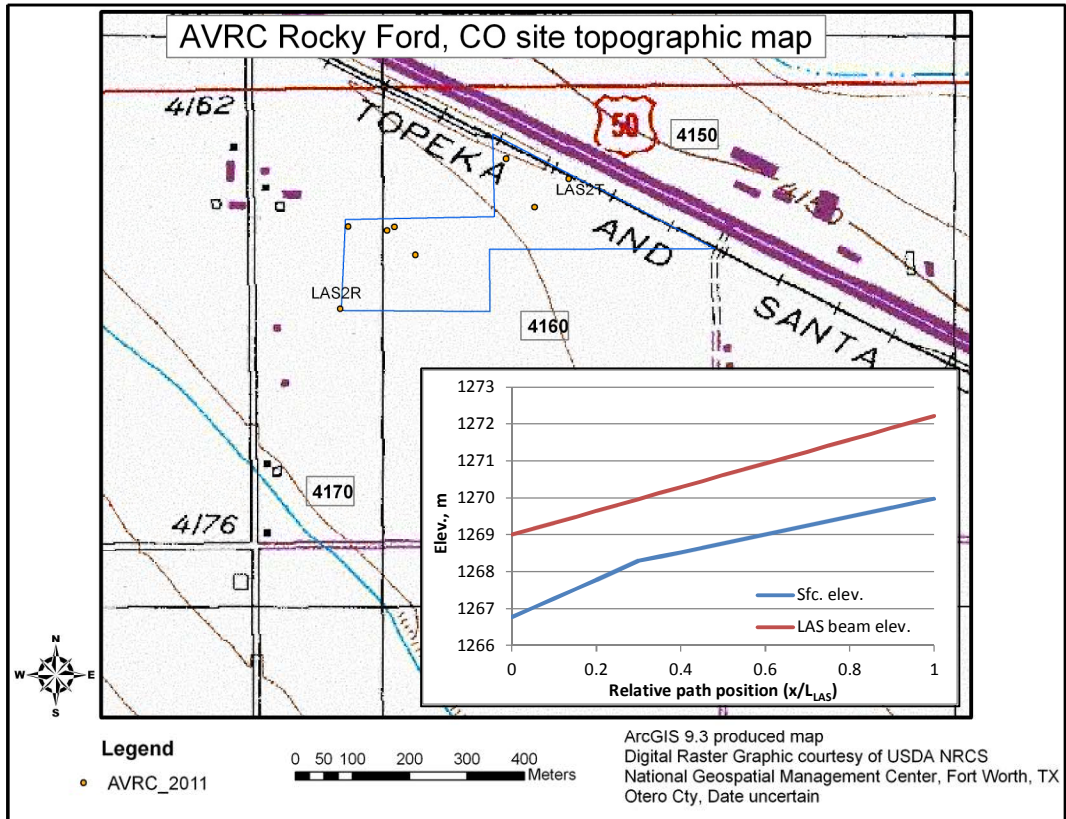


Figure A2.2. Topographic map showing 10 foot contours for AVRC site. LAS locations are labeled and shown with orange points. Blue perimeter represents SW and NE alfalfa field boundaries. Linear interpolations between the transmitter, the 4160 ft contour, and the receiver were used to estimate the path elevation profile. Profile plot is shown in lower right of image, with elevation in meters, for estimated elevations along LAS path. Solid red curve represents estimated beam elevation, based on setup height (2.24 m) off ground.

The topographic map elevations were observed to disagree significantly from the estimated GPS elevations (not shown). The elevation along the LAS path was estimated by linear interpolation between the three points along the LAS path extracted from the topographic map. The LAS beam elevation was estimated by adding the measured T and R heights to the estimated T and R elevations, respectively, and by subsequent linear interpolation between the T and R. The beam height along the path was then found by subtracting the elevation (surface) from the beam elevation along the path. Finally, discrete LAS path weights for 21 locations along the path (including the T and R locations; Table A2.1), provided by the LAS manufacturer, were used to derive an effective path-weighted beam height. It is notable that the topographic maps used for this analysis may be outdated and thus not applicable to the current situation, perhaps especially at the AVRC site. Further, using linear interpolation increases the uncertainty associated with this method. It was additionally noted that the 4160 (ft) contour at the AVRC site doubled back in close proximity to the LAS-2 T location (swale-like formation; Fig. A2.2), which was not accounted for in the analysis leading to the 1.86 m z_{LAS} estimation. This observation suggests a z_{LAS} (slightly) higher than 1.86 m.

Table A2.1 Kipp and Zonen-provided LAS path weights discretized for each 5% of the LAS path. Note zero contribution at the LAS T and R locations.

Relative position (x/L)	C_n^2 relative weight
0	0.000
0.05	0.002
0.1	0.009
0.15	0.018
0.2	0.031
0.25	0.046
0.3	0.062
0.35	0.079
0.4	0.093
0.45	0.104
0.5	0.108
0.55	0.104
0.6	0.093
0.65	0.079
0.7	0.062
0.75	0.046
0.8	0.031
0.85	0.018
0.9	0.009
0.95	0.002
1.0	0.000
Sum	0.996

APPENDIX 3. HARTOGENSIS 2006 CORRECTION FOR C_n^2

The justification for and formulation of the LAS C_n^2 correction for dissipation range contributions which is summarized here was given by Oscar Hartogensis (Hartogensis, 2006). The basis for the correction is that for lower wind speeds, the inner scale of turbulence (l_0 , m), which represents the boundary between the inertial range and the dissipation range of turbulence, can become more significant in magnitude and result in dissipation range contributions to the LAS signal. This issue becomes less important for increased aperture diameter (D , m). Hartogensis (2006) defined l_0 in terms of the dissipation rate of turbulent kinetic energy (ϵ) and incorporated a MOST function (f_ϵ) in order to solve for l_0 using strictly LAS output of friction velocity (u_* , m s⁻¹) and stability length (L_{mo} , m) (Eq. A3.1, 2);

$$l_0 = 7.4 \left(\frac{\nu}{u_*} \right)^{\frac{3}{4}} \left(\frac{0.41(z_{LAS} - d)}{f_\epsilon} \right)^{\frac{1}{4}}, \quad (\text{A3.1})$$

$$\text{where } \nu = \left(\frac{1.718 + 0.0049 \times T}{\rho_{air}} \right) \cdot 10^{-5},$$

$$\text{and } f_\epsilon = \begin{cases} \left(1 - 15.1 \frac{(z_{LAS} - d)}{L_{mo}} \right)^{-\frac{1}{3}} - \frac{(z_{LAS} - d)}{L_{mo}} - 0.16, & L_{mo} < 0 \\ 0.8 + 2.5 \frac{(z_{LAS} - d)}{L_{mo}}, & L_{mo} > 0 \end{cases} \quad (\text{A3.2})$$

Equation A3.1 requires input of air kinematic viscosity (ν), which is a function of air temperature (T , K) and density (ρ_{air} , kg m⁻³), shown above. The units for effective LAS height (z_{LAS}) and zero displacement height (d) are in m. The correction factor (m) for C_n^2 is given as a function of the ratio of D/l_0 (Eq. A3.3). Hartogensis (2006) suggested restricting the correction to cases where l_0 is less than 30 mm, since the behavior of Eq. A3.1 is unbounded for small u_* . By limiting l_0 to 30 mm, the maximum m is 1.0 and the minimum is approximately 0.7, where m is applied as shown in Eq. A3.4.

$$m = \frac{e^{0.72 \left(\frac{D}{l_0} \right)^{-2}}}{1 + 0.433e^{-\left(0.89 \left(\ln \left(\frac{D}{l_0} \right) - \ln(3.3) \right) \right)^2}} \quad (\text{A3.3})$$

$$C_{n_{corr}}^2 = m \times C_{n_{LAS}}^2 \quad (\text{A3.4})$$

APPENDIX 4. COMPUTATION OF G

Measurement of soil/ground heat flux at the surface is typically performed by measuring flux through thermopile plates at a depth of approximately 8 cm and accounting for flux at the surface using measurements of soil temperature (T_g) and soil volumetric water content (θ_v). The change in soil temperature (ΔT_g) over an averaging interval of (e.g.) 30 minutes, multiplied by the moist soil heat capacity (C_s , $\text{J kg}^{-1} \text{K}^{-1}$) over the depth (d_{pl}) from the surface to the plate, accounts for the heat energy stored (G_s , W m^{-2} ; Eq. A4.2). This is added to the plate measurement of heat energy flux (G_{pl} , W m^{-2}) to represent surface soil heat flux (G_{sfc} , W m^{-2} ; Eq. A4.3). In order to estimate C_s , the bulk density (ρ_b) of the dry soil and the dry soil heat capacity (C_d) must be given, along with the volumetric water content (θ_v) (Eq. A4.1). Soil bulk density (ρ_b , kg m^{-3}) is not the same for all soils, and must be measured or estimated from knowledge of the soil particle distribution and structure. Soil dry heat capacity (C_d) was taken as $840 \text{ J kg}^{-1} \text{K}^{-1}$ as a typical mineral soil value (Hanks and Ashcroft 1980 in HFT3 Campbell Scientific Instruction Manual 2003). Water content (θ_v , $\text{m}^3 \text{m}^{-3}$) was generally measured³² although in some cases measurement was not available and some estimation methods were performed (App. 5). In the equations below, ρ_w is the density of water (1000 kg m^{-3}), C_w is the heat capacity of water ($4190 \text{ J kg}^{-1} \text{K}^{-1}$), d_{pl} is the depth of the heat flux plate (m), and t is the time length of the averaging interval (e.g. 1800 s).

$$C_s = \rho_b C_d + \theta_v \rho_w C_w \quad (\text{A4.1})$$

$$G_s = \frac{\Delta T_g C_s d_{pl}}{t} \quad (\text{A4.2})$$

$$G_{sfc} = G_s + G_{pl} \quad (\text{A4.3})$$

³² Measurement was made with CS616 soil moisture sensors. For the AVRC site, since the readings were often clearly above range, some approximate calibration methods were used to scale down the CS616 θ_v .

APPENDIX 5. ALTERNATE METHODS FOR TIME SERIES θ_v ESTIMATION

For cases where continuous measurement of near surface soil moisture (θ_v) was not made at the soil heat flux (G) stations, alternate methods were considered. This was the case for the two weighing lysimeter stations at the AVRC study site. Theoretically, the presence of a weighing lysimeter provides an accurate tool for estimation of soil moisture through a soil water (mass) balance (SWB). The weighing lysimeter monolith is sealed from the exterior soil, preventing uncontrolled drainage and capillary/horizontal flow; therefore changes in monolith weight can be attributed to inputs of precipitation or irrigation and outputs of evapotranspiration (ET). Other known weight changes must also be recorded (e.g. plant harvest). In addition to the weighing lysimeter and ancillary instrumentation, neutron moisture meter (NMM) access tubes have been installed within and directly outside of the weighing lysimeter monoliths at both stations. The SWB method was used only for one of the lysimeter locations, in the southwest alfalfa field, and subsequent details for the SWB methods refer to this lysimeter. Periodic monolith NMM readings were used to anchor or initiate the soil water balance with a known soil moisture value. Daily weight changes were tabulated for the lysimeter in order to estimate the daily ET. Day-end depletions in crop root zone water were accounted for by adding the depletion from the previous day to the current day ET total less any added (irrigation or precipitation) water. Depletion amounts were related to soil VWC with additional information on the root zone depth, field capacity moisture content (FC_v), and wilting point moisture content (WP_v) (Eq. A5.1).

$$\theta_v = FC_v - \left(\frac{D_i}{Z_r} \right), \quad (\text{A5.1})$$

where D_i is the current-day depletion (mm) and Z_r is the root zone depth (mm). The alfalfa root zone was estimated to be 1.5 m, and FC_v and WP_v values were provided along with the NMM and lysimeter datasets (Lane Simmons, AVRC). The SWB was performed for the effective crop root zone, and therefore the balance was initiated with the mean of the NMM readings over the root zone (10 – 150 cm). To subsequently derive the near surface (~ 10 cm) θ_v , a relationship between 10 cm and mean 10-150 cm NMM readings was developed for the 2011 season. This relationship ($r^2 = 0.61$) was used to predict daily 10 cm θ_v from the daily SWB-derived root zone mean θ_v . The SWB was initiated on April 7th and anchored again on June 3rd. Other NMM readings were fairly well correlated with SWB-predicted θ_v , which suggested fair performance of the SWB method.

For the second lysimeter, some continuous moisture readings were available but for depths beyond the near surface soil. Therefore, consideration was given to the development of a relationship between the Watermark-derived soil moisture at 0.5 m and the NMM 10 cm readings. Watermark soil moisture potential sensors (Irrometer Company, Inc., Riverside, CA) yield resistance output, which must be calibrated to a (soil temperature-corrected) soil matric potential value (kPa). The manufacturer-provided (CSI 253/257 WMK200 Instruction Manual 2009) linear relationship was used to calculate potential (kPa) from the resistance measurements. Subsequently, the Van Genuchten equation was used to relate the SMP to θ_v , using lab-calibrated parameters for the applicable soil type (Varble, 2011). The calculated θ_v values corresponding to the times of the NMM readings were tabulated and plotted against the 10 cm NMM θ_v values.

The resulting relationship ($r^2 = 0.78$) was used to predict the 10 cm time series θ_v for the second lysimeter station.

APPENDIX 6. SPATIAL AVERAGE R_n AND G ESTIMATION PROCEDURES

The energy balance equation used to solve for Bowen Ratio (β) for LAS input (Eq. 16) required the input of net radiation (R_n , W m^{-2}) and ground heat flux (G , W m^{-2}). The relative impact of R_n and G on the final H depends on the magnitude of β , but is generally not too significant. Nonetheless, it was desirable to accurately estimate the effective spatial averages of R_n and G for the study areas at the Timpas and AVRC sites.

Timpas

At the Timpas site, two stations were available for measurement of R_n and G . The R_n measurements were made using NR-Lite (Kipp and Zonen, CSI, Logan, UT) sensors located at the LAS-1 receiver (LAS1R) and the SAT1 profile tower (Fig. 2). The soil heat flux (SHF) sensors were installed at the same locations. Bias was observed for SAT1 R_n greater than LAS1R R_n during the daytime. This bias was attributed to field of view (FOV) differences in the surface characteristics, and the effective R_n was taken as the average from both sensors³³. In addition, the R_n from both sensors were plotted against one another in order to develop predictive relationships to estimate LAS1R R_n as a $f(\text{SAT1 } R_n)$ and vice versa. These relationships were used to fill gaps in the record period which occurred for both sensors (at different times). The overall deviation between R_n from both sensors was approximately 5%. The computation of SHF (G_{sfc} , W m^{-2}) was performed as detailed in Appendix 4. The soil bulk density for the site was estimated using information from the USDA NRCS Web Soil Survey (<http://websoilsurvey.nrcs.usda.gov>), from which the average value from the range was taken as the effective surface soil bulk density (1.225 g cm^{-3}). Preliminary calculations of G_{sfc} from both locations suggested that LAS1R G_{sfc} was greater than SAT1 G_{sfc} . However, the plate depths used for the LAS1R calculations were approximately 2.5 cm (1") larger than those for SAT1, and after checking the plate SHF (G_{pl}) from both stations, it was considered appropriate to use the same plate depths for both stations. This modification resulted in much better comparison between LAS1R and SAT1³⁴. Based on the observed close relationship between LAS1R and SAT1 G_{sfc} ($\text{SAT1} = 0.98 \times \text{LAS1R}$, $r^2 = 0.99$), the LAS1R G_{sfc} was used alone to represent the effective site G_{sfc} . Although it may have been better to use the station average, the associated deviations in G_{sfc} are considered negligible.

AVRC

At the AVRC site, four stations were available for measurement of R_n and G . However, two of the stations were not operational until a later date in the period of record. Further, the field management was considered for determining the consensus R_n and G for use with LAS-2 processing. Although the details are not discussed here, satellite remote sensing data (Landsat TM, 30 m pixel resolution) were processed to obtain normalized difference vegetation index (NDVI) maps for the AVRC site. Several NDVI images were produced for the period of record in order to assess surface vegetation variability in the LAS-2 path area. The area of interest

³³ Current examination of sensors suggests that the LAS1R sensor may be biased low, such that the effective R_n may have been better estimated with SAT1 R_n .

³⁴ Plate depths for both stations were measured by different people, giving possible explanation for the different values reported. Plates were likely installed at roughly the same depth for both locations according to manufacturer recommendations.

(AOI) considered applicable to the LAS-2 measurements was defined by the two alfalfa fields, thus neglecting contribution from neighboring fields. It was found that the AOI mean NDVI was comparable to the mean NDVI for the pixels representing the R_n/G stations – this finding was used to support the use of average station R_n and G to represent effective LAS-2 R_n and G . This was a rough assumption, relying on the correlation between NDVI and R_n/G for alfalfa. The methods discussed here for R_n and G apply to the August 4th – Oct. 21st LAS-2 period of record. The lysimeter locations were operational for the complete period of record. The ancillary station in the southwest alfalfa field (SW-ancill.) was installed on August 27th, following the harvest on the 26th. The ancillary station in the northeast alfalfa field (NE-ancill.) was installed on Sept. 7th. Based on knowledge of field conditions, predictive equations were developed from linear regression plots of ancillary versus lysimeter station R_n values in order to fill the missing data for the SW- and NE-ancill. stations from August 4th – 26th. After the field harvest, the NE-ancill. station was still not available, and the lysimeter stations were not representative of the bulk field due to delayed cutting and subsequent irrigations occurring only at the lysimeters. Therefore the SW-ancill. station was used to represent effective LAS-2 R_n until the lysimeter stations were assumed to represent field conditions better. Subsequently, the SW-field R_n was predicted as the average of the lysimeter and SW-ancill. station R_n until the Oct. 21st de-installation. The NE-lysimeter was used to develop a different predictive relationship to estimate the NE-ancill. R_n for the Sept. 2nd – 7th period, using data after the NE-ancill. installation on Sept. 7th. This was performed because the NE-lysimeter had been irrigated but not the field, and thus the NE-ancill. station was assumed to better represent the field R_n until the field irrigation began on Sept. 16th. After this date, the average lysimeter and ancillary R_n was used to predict the NE-field R_n until the Oct. 21st de-installation. Finally, the effective LAS-2 R_n was taken as the average of the SW and NE-field R_n solutions according to the above discussion. The computation of G_{sfc} for the AVRC sites was problematic for the NE-field due to apparent data quality control issues for both the lysimeter and ancillary stations. Based on knowledge of the field conditions, it was hypothesized that the NE-lysimeter station G_{sfc} was greater than and ahead of (amplitude and phase) the expected (actual) G_{sfc} , and that the NE-ancill. station was lower than and behind the expected G_{sfc} . For this reason, it was finally decided to approximate the NE-field G_{sfc} using the average of the lysimeter and ancillary stations. Further, since no NE-ancill. G_{sfc} was available from August 4th – Sept. 7th, a similar procedure to that discussed for R_n was used to predict the August 4th – 26/27th NE-field G_{sfc} . In this case, however, the mean lysimeter and ancillary station G_{sfc} was directly predicted (to represent NE-field G_{sfc}) from the NE-lysimeter G_{sfc} . Subsequently the LAS-2 effective G_{sfc} was determined as follows: SW-field conditions were considered to be uniform between lysimeter and ancillary stations for the August 4th – 26th period, so that the SW-field G_{sfc} was taken solely from the lysimeter station. Subsequently, the SW-ancill. station was considered to represent the post-harvest condition for both alfalfa fields, and was taken as the effective LAS-2 G_{sfc} , from August 27th – Sept. 7th. On Sept. 8th, the SW-field G_{sfc} was taken solely from the SW-lysimeter station, due to the apparent impacts of irrigation water (temperature) on the SW-ancill. G_{sfc} . The average lysimeter and ancillary G_{sfc} was then used to represent the SW-field from Sept. 9th – Oct. 21st. As implied above, the NE-field G_{sfc} was predicted as the average of the lysimeter and ancillary station solutions from Sept. 8th – Oct. 21st (this was not in consideration of the representative field conditions, but based on the assumption that the overestimated lysimeter G_{sfc} and underestimated ancillary G_{sfc} could together represent the approximate field average G_{sfc}). Finally, the LAS-2 effective G_{sfc} was taken as the average of the SW- and NE-field solutions (except for the August 27th – Sept. 7th period). It is clear that the

AVRC site determinations of R_n and G were prone to much more uncertainty than the Timpas site solutions. However, it is notable that the impact of this uncertainty is generally relatively small on H_{LAS} , since R_n and G are required only to calculate β for input to the LAS model.

APPENDIX 7. LAS-1 TIMPAS INPUT MODIFICATIONS FOR TESTING

After preliminary processing was performed with the Timpas site data for each LAS according to the different processing methods (u_{*1-L} , u_{*2-L} , u_{*EC} , etc.), some consideration was given to potential biases in a few of the LAS input parameters. New estimates for the inputs were determined and the LAS-1 data were reprocessed to determine the effect of the input modifications on H . For example, the LAS effective height was initially determined for processing as the average height of the transmitter and receiver (aperture center) without accounting for variable topography within the path. In addition, the determination of the Timpas effective crop height was approximate, suggesting potential error in the z_{om} estimate. Finally, the LAS-1 on-site calibration test revealed the U_{Cn2} signal to be outside of the manufacturer-provided acceptable range for multiple path length settings, suggesting a drift in the LAS-1 calibration. The topography for the Timpas site was considered for the new estimation of LAS effective height, which suggested that the ground slope was not uniform along the path, resulting in the estimation of a new effective LAS height larger than the original estimate ($z_{LAS-1\ new} = 2.48$ m). The details of this procedure were shown in Appendix 2. Estimation of the Timpas effective z_{om} value could have been performed using either the EC or the SAT two-level solutions of u_{*} , since these were derived without assumptions regarding z_{om} . Examining the z_{om} derived from both u_{*2-L} and u_{*EC} for near-neutral atmospheric stability suggested that z_{om} was approximately 0.03 m. In order to estimate a correction (factor) for the LAS-1 U_{Cn2} data based on the calibration test results, it was assumed that the U_{Cn2} signal obtained in the ‘calibration’ mode would be comparable to the U_{Cn2} signal obtained in ‘signal’ (operation) mode. The average deviation (mV) in the LAS-1 signal from reference was taken from three path length settings closer to the actual Timpas path length and considered applicable as a constant mV offset for the LAS-1 U_{Cn2} data. This procedure for correcting the U_{Cn2} signal was not recommended and was thus an approximate correction for testing purposes. Table A7.1 below gives a summary of the LAS-1 input modifications. Each modification resulted in an increase in H_{LAS} .

Table A7.1 LAS-1 Timpas input modifications for u_{*1-L} method

Variable/Parameter	Modified value	Original value
z_{LAS} (m)	2.48	2.267
z_{om} (m)	0.03	0.014
U_{Cn2} (V)	$U_{Cn2} + 0.048$	U_{Cn2}

APPENDIX 8. KORMANN AND MEIXNER (2001) SOURCE AREA MODEL

The advantage of an analytical flux source area model such as that proposed by Kormann and Meixner (2001) is to permit efficient implementation for time series data analysis. The premise of a source area model is that the flux measured by an instrument at a given (x, y) datum and height (z_m) is the integration of the vertical fluxes occurring at all points within a variable upwind area (see Schmid, 1994). A flux source area function is generally given of the form $F(x, z_m)$, where x is the upwind distance and F is the crosswind-integrated relative contribution to the flux at x . The crosswind-integrated denotation simply means that the y -dimension has already been integrated for the evaluation of F at x_i . The Kormann and Meixner (2001) model is given as:

$$F = \frac{1}{\Gamma(\mu)} \frac{\xi^\mu}{x^{1+\mu}} e^{-\frac{\xi}{x}} \quad (\text{A8.1})$$

$$\xi(z) = \frac{Uz^r}{r^2 \kappa} \quad (\text{A8.2})$$

$$\mu = (1 + m) / r \quad (\text{A8.3})$$

$$r = 2 + m - n \quad (\text{A8.4})$$

$\Gamma(\mu)$ is the gamma function for the μ variable defined in Eq. A8.3, x is the upwind distance (m), and z is the height at which the equation(s) are evaluated, which is taken by the authors to be the effective instrument height ($z_m = z_{EC} - d$). In order to solve for the velocity and eddy diffusivity coefficients, U and κ , respectively, the authors combine power law profiles and Monin-Obukhov similarity (MOS) profiles as follows:

$$u(z) = Uz^m \quad (\text{A8.5})$$

$$K(z) = \kappa z^n \quad (\text{A8.6})$$

$$u(z) = \frac{u_*}{k} \left(\ln \left(\frac{z}{z_0} \right) + \Psi_m \left(\frac{z}{L_{mo}} \right) \right) \quad (\text{A8.7})$$

$$K(z) = \frac{ku_* z}{\phi_c \left(\frac{z}{L_{mo}} \right)} \quad (\text{A8.8})$$

Here, Eqs. A8.5 – A8.6 are the power law profiles for horizontal wind speed and eddy diffusivity, and Eqs. A8.7 – A8.8 are the MOS profiles for the same. Parameter z can be taken as the instrument height (z_m) and u_* is the friction velocity (m s^{-1}). Further, the exponents, m and n , can be solved by:

$$m = \frac{u_* \phi_m}{ku} \quad (\text{A8.9})$$

$$n = \begin{cases} \frac{1}{1 + 5z/L}, & L > 0 \\ \frac{1 - 24z/L}{1 - 16z/L}, & L < 0 \end{cases} \quad (\text{A8.10})$$

The Ψ_m in Eq. A8.7, φ_c in Eq. A8.8, and φ_m in Eq. A8.9 are stability functions of z_m/L_{mo} . The authors use the relationships given by Dyer (1974) to solve these functions. It is apparent also that n (Eq. A8.10) is a function of z_m/L_{mo} . Solving for m and n , along with $u(z)$ and $K(z)$ from Eqs. A8.7 – A8.8, Eqs. A8.5 and A8.6 can be solved for U and κ , respectively, allowing for evaluation of the footprint weights from Eq. A8.1 strictly as a function of downwind distance (x).

In order to incorporate the y -dimension into the source area model, it is common to use a Gaussian crosswind distribution function of form:

$$D_y(x,y) = \frac{1}{\sqrt{2\pi}\sigma} e^{-\frac{y^2}{2\sigma^2}} \quad (\text{A8.11})$$

Where σ is the crosswind dispersion and is commonly taken as $\sigma = \sigma_v x / \bar{u}$ (e.g. Kormann and Meixner, 2001), where σ_v is the standard deviation of the lateral wind (crosswind) fluctuations as defined by Schmid (1994). Here \bar{u} is the mean ($0 < z < z_m$) horizontal wind speed, though in some applications, this may be taken as the wind speed measurement at height z_m . The 2-D source area function is then equal to $F \times D_y$, from equations A8.1 and A8.11. It is notable that the value for z_m is somewhat ambiguous, defined as both the flux instrument height and the wind speed measurement height (both over the zero displacement height). For the eddy covariance case, this works rather well, since the sonic anemometer is the source of wind speed and sensible heat flux measurements. However, for the LAS case, wind speed measurement height would not necessarily be the same as the LAS height. For this study, the (LAS performance evaluation) analysis was performed only during periods where EC data were available; the LAS source area was modeled using EC data, but with z_m equal to z_{LAS} less the zero displacement height. Although this method is approximate, it is assumed to be conservative, since z_{LAS} was (slightly) greater than z_{EC} ³⁵; further the source area results were used more qualitatively than quantitatively, so that the absolute accuracy was not critical.

The above-described model considers the source area for a point (x, y) measurement (e.g. EC), and therefore must be adapted for the case of the path-integrated LAS fluxes (i.e. there is not one point origin of the source area, but a ‘line-path’ origin, where each point on the line (path) carries a different weight). Meijninger et al. (2002) indicated it was necessary to combine the LAS path weighting function with the source area function, specified by Von Randow et al. (2008) as a convolution. The discussion in Timmermans et al. (2009) suggested that the LAS path can be discretized into individual points of appropriate weight for this purpose. Following this approach, the application of the given source area model to the AVRC LAS-2 setup involved dividing the LAS path into 10 points, each assigned a weight representative of the applicable 10% of the path according to the LAS path weighting function. These weights were determined as follows: The

³⁵ For z_{LAS} equal to 2.24 m, this statement applies; however, considering the later estimate of z_{LAS} equal to 1.86 m, the statement would not apply.

interval weights for each 5% interval of the LAS path were adopted from the manufacturer (Table A2.1) which are observed to add up to a sum of (effectively) 1.0. The weights were extracted from each 10% interval of the LAS path as shown in Table A8.1. The total weight for each 10% interval, given at the interval center, was defined as the average of the weights at the interval beginning and end multiplied by two, in order to achieve a summation of 1.0 as in the original 5% interval table. The resulting path weights and their corresponding relative positions on the LAS path are shown in Table A8.1. In Figure A8.1a, the plot of the manufacturer-provided 5% interval LAS path weights is shown, along with the same plot when only using the 10% interval values. Subsequently, Fig. A8.1b shows the total 10% interval weights to be used for application to the source area model.

Table A8.1 Kipp and Zonen-provided LAS path weights extracted for only 10% intervals of the LAS path. Total interval weight column represents the average interval beginning/end value, multiplied by two. For example, the total interval weight for the 25% path position was taken as the average of the 20% path value (0.031) and the 30% path value (0.062), multiplied by two to equal 0.093.

Relative position (x/L_{LAS})	C_n^2 relative weight	Total interval (relative) weight	Relative position (x/L_{LAS})
0	0		
0.1	0.009	0.009	0.05
0.2	0.031	0.04	0.15
0.3	0.062	0.093	0.25
0.4	0.093	0.155	0.35
0.5	0.108	0.201	0.45
0.6	0.093	0.201	0.55
0.7	0.062	0.155	0.65
0.8	0.031	0.093	0.75
0.9	0.009	0.04	0.85
1	0	0.009	0.95

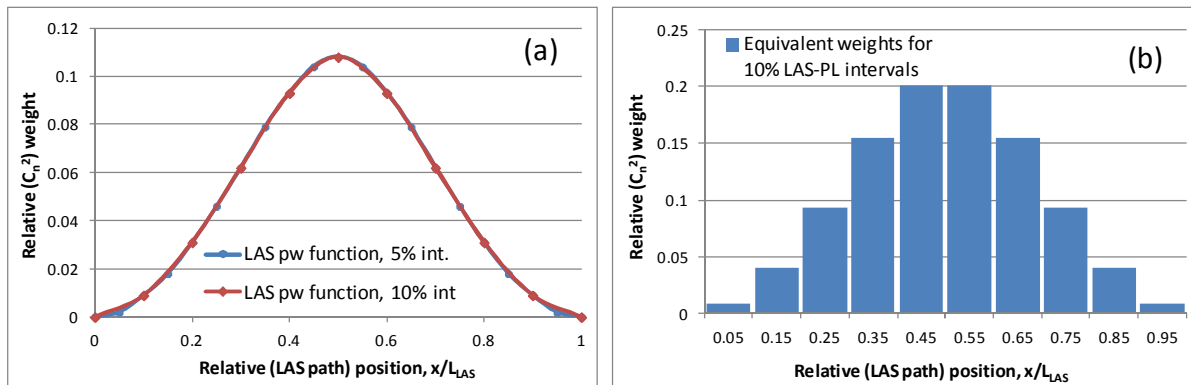


Figure A8.1. LAS 5% path interval weights provided by manufacturer, further plotted with only 10% interval values showing negligible difference in the resolution (a) and the total interval weights for the LAS path 10% intervals (b).

An implementation tool for the Kormann and Meixner (2001) model has been provided by Neftel et al. (2008), realized in Excel VBA. The tool requires input of the friction velocity (u_*), stability length (L_{mo}), crosswind standard deviation (σ_v), wind direction (θ), measurement height (z_m), and wind speed at measurement height (U). In addition, the tool performs geographic/geometric computations to yield source area percent contributions of the various upwind “fields”, for which the coordinates are also a user input. Finally, the user must input the coordinates of the measurement (in the same coordinate system as the fields). The model was run 10 times for the LAS, each time holding the input data constant and varying the measurement coordinates according to the 10 path points identified in Table A8.1. In order to limit the (2-D) boundary of the upwind source area, Neftel et al. (2008) limit the x and y extents to the point where the value of $F(x,y,z_m)$ is less than 1% of the observed maximum $F(x,y,z_m)$. Therefore, the amount of the total measurement source area captured in the reported boundary is less than 100%; for this study the amount varied approximately between 70-90%. Thus, the reported field contributions are fractions not of the total source area, but of that captured in the boundary. The field definitions for the application to the LAS and EC data in this study included the two alfalfa fields and several of the surrounding fields. Further the alfalfa fields were each divided into six sub-quadrangles. The coordinates were determined using ArcGIS 9.3 ArcMap software and a USDA FSA NAIP aerial image of the AVRC site. Finally, the effective LAS source area was determined using a weighted average of the field contribution outputs from the 10 model runs according to the LAS path weights in Table A8.1.

APPENDIX 9. LAS UNCERTAINTY ANALYSIS METHODS

The uncertainty analysis for the LAS data processing was performed in several stages. Propagation of uncertainty to H was simulated by processing the data with modified inputs. This method was used due to the iterative calculations involved in computing H , making a direct calculation of uncertainty in H more difficult. Further, since the determination of H_{LAS} involved determination of the first (stability) iteration of H , followed by subsequent iteration of H for the corrected Bowen ratio and C_n^2 , the determination of δH was also performed in such an iterative fashion. The value of δC_T^2 was computed directly (pre-iteration) using estimated input uncertainties (Table 2) of air temperature (T), barometric pressure (BP), relative humidity (RH), structure parameter of the air refractive index (C_n^2), and Bowen ratio (β). The partial derivative (general rule) method given in Taylor (1997) was used to determine δC_T^2 . In this method, the partial derivatives of C_T^2 with respect to each of the variables defining C_T^2 were computed (dC_T^2/dx , where $x = T, BP$, etc.) and multiplied by the corresponding values of δ . The sum of these products is equal to the total δC_T^2 (Eq. A9.1).

$$\delta Y = \left| \frac{dY}{dx_i} \right| \times \delta x_i + \dots + \left| \frac{dY}{dx_n} \right| \times \delta x_n, \quad (\text{A9.1})$$

$$\text{where } Y = f(x_1, \dots, x_n),$$

and δx_i represents the uncertainty for variable x_i . If the uncertainties for the different variables are random and independent, the quadrature sum can be used in place of the direct sum, reducing the apparent uncertainty (Eq. A9.2).

$$\delta Y = \left(\left(\frac{dY}{dx_i} \times \delta x_i \right)^2 + \dots + \left(\frac{dY}{dx_n} \times \delta x_n \right)^2 \right)^{\frac{1}{2}} \quad (\text{A9.2})$$

The assumption of independent and random uncertainties was made to determine δC_T^2 , using Eq. A9.2. The value of air density uncertainty ($\delta \rho_{air}$) was computed in the same fashion, using corresponding input uncertainties of T , BP , and RH . However, the saturation vapor pressure ($e_{s(T)}$) uncertainty was found independently using δT , and included with variables T , BP , and RH for the determination of $\delta \rho_{air}$. Since in this case the values of δT and δe_s were not independent, the direct sum method (Eq. A9.1) was used. Subsequently, the uncertainty in H was dependent on time series variables C_T^2 , T , wind speed (U), and ρ_{air} , and on constants LAS height (z_{LAS}), wind speed cup height (z_U), momentum roughness length (z_{om}), and zero displacement height (d). To consider the maximum positive and negative uncertainty in H , it was considered for each of the above inputs whether a directly or inversely proportional relationship with H existed. For variables which naturally varied together (e.g. C_T^2 and T), the same sign of δ_{input} was used. In addition, for variables which were dependent on the same inputs (e.g. C_T^2 and ρ_{air}), the sign of δ_{input} was assigned to each as would naturally occur (i.e. and e.g. for the case of C_T^2 and ρ_{air} , variables T , BP , and RH have opposite effects on C_T^2 and ρ_{air} ; therefore, the opposite sign of δ was used for C_T^2 and ρ_{air}). In such a case, it was estimated which variable and corresponding uncertainty would have a larger effect on H , and the sign of δ used for this (dominant) variable was made consistent with the sign of δH . After performing the first iteration for stability, the

solution of H_{LAS} was used along with measurements of R_n and G to compute β , assuming latent heat flux (λE) was the residual of $(R_n - G - H)$. The uncertainty of β was computed using the partial derivative rule and assuming H , R_n , and G uncertainties were independent and random (Eq. A9.2). The partial derivative method was used since H occurred in the equation for β more than once. The value of δH at each time step was given in $W m^{-2}$ as the average of the differences between the original H solution and the positive and negative δH solutions of H . Values of positive and negative δH were generally nearly of the same magnitude. The computations of corrected C_n^2 and corrected β were computed using the actual input magnitudes and subsequently used to compute the second iteration of H . For the second iteration, updated values of δC_n^2 and $\delta\beta$ were used based on (1) 0.5% (δC_n^2) applied to corrected C_n^2 (instead of original C_n^2) and (2) $\delta\beta$ derived from δR_n , δG , and δH as described above. Thus, only the value of δC_n^2 was different for the uncertainty propagation in the second iteration. The time series solution of δH resulting from the second iteration of H was considered to represent the final expected uncertainty in H , although in standard processing generally three or four iterations were performed. This procedure was performed for the three alternative friction velocity (u_*) methods wherein attention was given to the difference in uncertainty propagation for each. For example, the method using the sonic anemometer u_{*EC} was adjusted to include δu_* (Table 2) rather than the uncertainties associated with the alternate logarithmic wind profile (LWP) computation of u_* . The uncertainty propagation calculations were computed for both study sites for a subset of the data.

The period of July 22nd to August 2nd was tested for uncertainty propagation to LAS (-1) H for the Timpas site. This period incorporated generally dry conditions from the 22nd until the 28th, and subsequently more wet conditions following a (significant) rainfall on the 28th. Propagated uncertainty was determined for the u_{*1-L} , u_{*2-L} , and u_{*EC} methods. In general, the pattern of δH ($W m^{-2}$) was diurnal, increasing with H during the morning and decreasing with H during the afternoon. The relative (%) δH was more consistent, showing less diurnal deviation. The exception was for the u_{*EC} H_{LAS} method, which showed sharp increases in relative δH for periods of low u_* . This is because the Nemitz et al. (2009) model showed very large relative δu_* for increasingly small values of u_* . The values of δH ($W m^{-2}$) were plotted against the absolute value of the H solution ($|H|$, $W m^{-2}$) for the different processing methods, revealing linear relationships between uncertainty and H . These plots for the Timpas data subset for LAS-1 are shown in Fig. A9.1a-c.

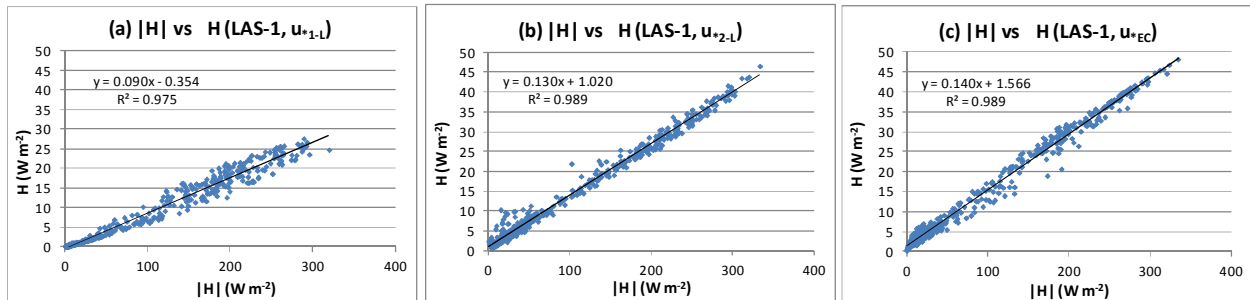


Figure A9.1. Regression plots showing relationship between propagated uncertainty in H and H absolute value; for Timpas site LAS-1 data subset July 22nd - August 2nd, u_{*1-L} method (a), u_{*2-L} method (b), and u_{*EC} method (c). Solid black line represents best-fit linear regression; regression slopes used to predict relative uncertainty in H for each LAS for the available period of record.

Since the correlation was quite good, it was decided to use the linear regression slope for each method as the (constant) relative uncertainty in H for the respective method. Further, these slope uncertainties were assumed applicable for the entire record period at Timpas and for each LAS unit. For the AVRC site, two data subsets were tested to account for post-harvest conditions (August 28th – Sept. 8th) and for established crop conditions (Oct. 8th – 21st). Again, the u_{*1-L} , u_{*2-L} , and u_{*EC} methods of processing (all HCF1) were tested. Results followed the same patterns as for the Timpas site; absolute δH (W m^{-2}) exhibited a diurnal pattern while the relative (%) δH was fairly consistent. Relative δH was generally a few percent higher for the October subset versus the early Sept. subset. Figures A9.2a-c show the δH versus $|H|$ plots for the AVRC data subsets, combining data from both subsets.

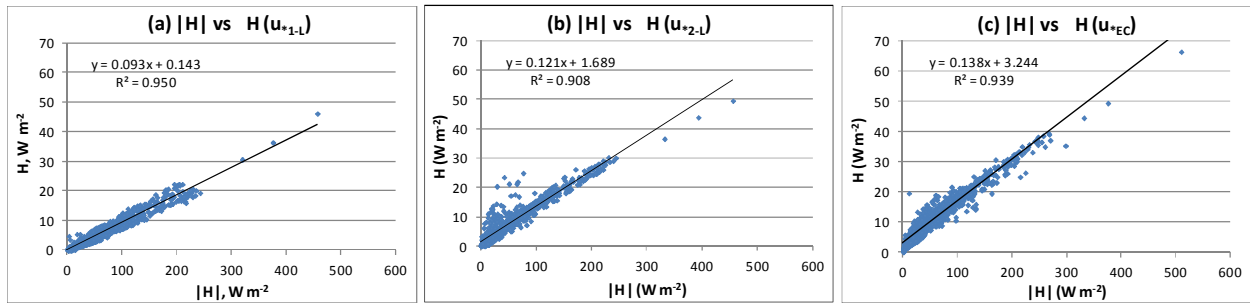


Figure A9.2. Same as Fig. A9.1, for AVRC site data subsets August 28th – Sept. 8th and Oct. 8th – 21st. Subsets data are combined in regression plots. The u_{*2-L} method was using 1m/3m arm pairs. Regression slopes were used (as for Timpas) to predict full period of record uncertainty in H_{LAS} .

Despite scatter being somewhat larger for the AVRC data, the same decision was made to apply the linear regression slope as the constant relative uncertainty for H_{LAS} for the entire analysis period (August 28th – October 21st). Figure A9.3 shows (for the u_{*1-L} method) that the Oct. subset data followed the same δH versus $|H|$ relationship as the early Sept. subset data, suggesting that the use of a constant slope uncertainty for the period of record was acceptable.

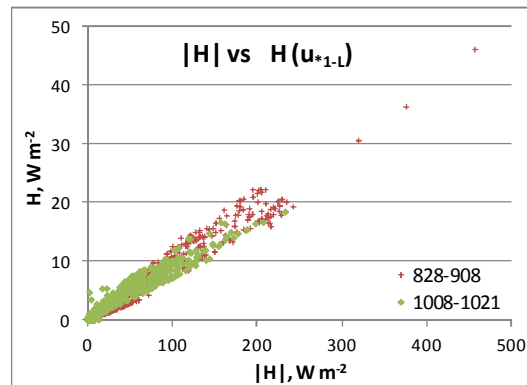


Figure A9.3. Same as Fig. A9.2a for the AVRC site, subdivided according to the two uncertainty analysis subsets, August 28th – Sept. 8th and Oct. 8th – 21st. The plot is included to show the overall similar trend of relative δH for both periods.

APPENDIX 10. LAS (ON-SITE) CALIBRATION TEST

The Kipp and Zonen Large Aperture Scintillometer user manual (Kipp and Zonen B.V. 2007) provides guidelines for conducting an on-site calibration test of the LAS receiver electronics. This test was performed on July 21st (2011) at the Timpas site for LAS-1 and -2, and later on August 10th (2011) for LAS-3. After the unit is powered, the toggle switch on the back of the receiver labeled ‘mode’ is set to ‘calibration’, which causes a reference signal to be sent to the receiver electronics. Using a (digital) multimeter, voltage readings can be taken at the $\log C_n^2$ BNC socket. Note that positive and negative multimeter leads can be used directly to read the voltage at the BNC socket by touching the positive lead to the central pin port and the negative lead to the outer shield. The manufacturer provides values of appropriate ($\log C_n^2$) UC_n^2 voltage readings for different path length settings when conducting the calibration test. These are shown below in Table A10.1. The manufacturer recommends the unit is significantly out of calibration if the readings are not within ± 15 mV of the desired value.

Table A10.1 Kipp and Zonen Large Aperture Scintillometer Instruction Manual values of UC_n^2 measured at the $\log C_n^2$ BNC socket for different potentiometer settings (in calibration mode, at room temperature)

Potentiometer (--)	UC_n^2 at BNC (mV)
200	1415
300	1004
400	650
500	316
594	0.0
700	-398
800	-859
884	-1415

APPENDIX 11. EXPERIMENT PHOTOS



Figure A11.1 Allen ranch near Timpas, CO where LAS experiments were conducted in 2011 (June 29th, 2011)



Figure A11.2 North end of LAS transect at Timpas site, LAS-1 and -3 Transmitter and LAS-2 Receiver (June 30th, 2011)

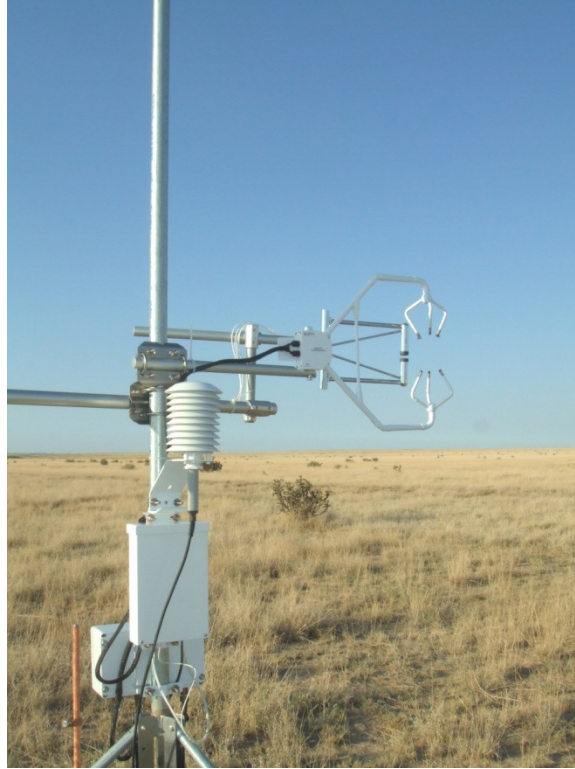


Figure A11.3 Close-up of Eddy Covariance tower at Timpas site (July 1st, 2011)



Figure A11. 4 SAT tower and Eddy Covariance (background) at Timpas site (July 21st, 2011)

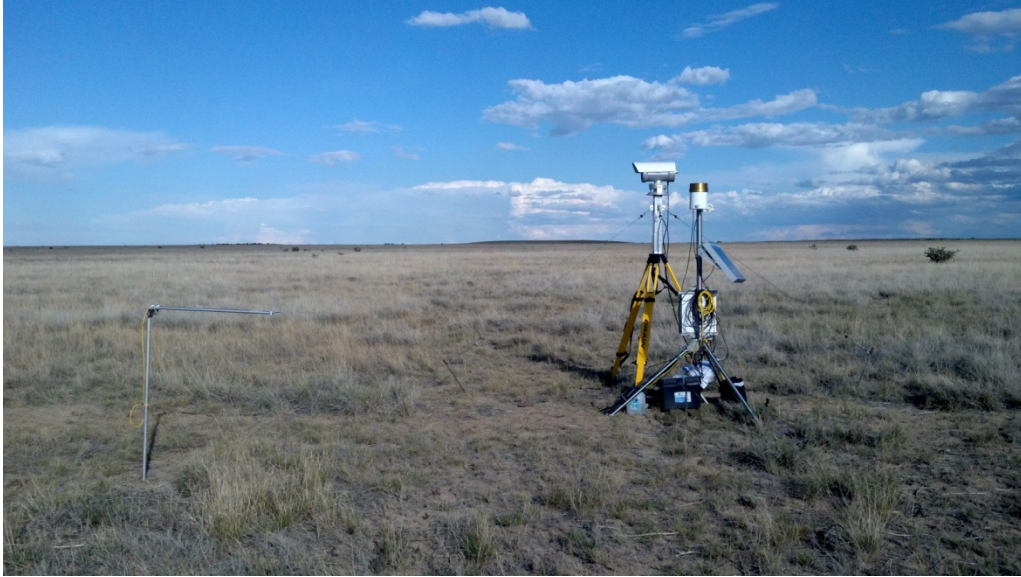


Figure A11.5 LAS-1 Receiver at south transect end at Timpas site; NR-Lite net radiometer (left) and TE-525 Rain gauge (next to LAS) evident in picture (September 16th, 2011)



Figure A11.5 LAS-1 Receiver at south transect end, looking north toward Transmitter at Timpas site (September 17th, 2011)



Figure A11.7 LAS-2 Receiver at southwest corner of southwest alfalfa field at AVRC site; alfalfa was being cut (August 26th, 2011)



Figure A11.8 Eddy Covariance tower and SAT tower (background) at north edge of southwest alfalfa field at AVRC site; alfalfa had been cut on August 26th (August 27th, 2011)



Figure A11.9 Ancillary (R_n and G) station in northwest corner of southwest alfalfa field; mast with SI-111 Infrared Radiometer (IRT) and mast with CNR1 four way net radiometer (background) (September 17th, 2011)



Figure A11.10 Ancillary (R_n and G) station in northwest corner of northeast alfalfa field; growth conditions were not as good in this section of the field; mast with SI-111 IRT and NR-Lite net radiometer in foreground (September 17th, 2011)



Figure A11.11 At LAS-2 Transmitter at north edge of northeast alfalfa field, looking southwest towards Receiver (September 17th, 2011)